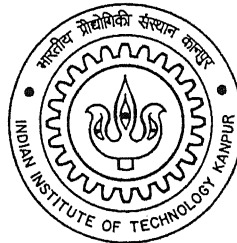


**COMPUTATION OF FLOWS PAST
MULTI-ELEMENT AIRFOIL USING
SPALART-ALLMARAS TURBULENCE MODEL**

*Thesis Submitted
in Partial Fulfillment of the Requirements
for the Degree of
Master of Technology*

by

Ashoke De



**Department of Aerospace Engineering
Indian Institute Of Technology, Kanpur
India**

July, 2004

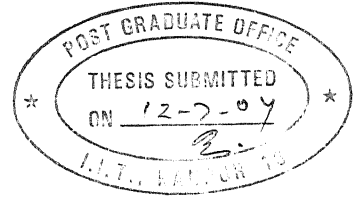
TH
AE/2004/M
D34c

7 OCT 2004

दुर्वाचम काशीनाथ कैलकर पुस्तकालय
भारतीय प्रौद्योगिकी संस्थान कानपुर
मबापि क० A...148871.....



A148871



Certificate

Certified that the work contained in the thesis entitled **Computation of flows past Multi-Element airfoil using Spalart-Allmaras turbulence model** by Ashoke De, has been carried out under my supervision and it has not been submitted elsewhere for a degree.

Dr. Sanjay Mittal

Professor

Department of Aerospace Engineering
Indian Institute of Technology Kanpur
Kanpur-208016, India.

July, 2004

Dedicated

to

My parents

Abstract

The present research is concerned with 2-D simulations of turbulent flows using Spalart-Allmaras turbulence model on various geometries like *flat plate*, *NACA0012 airfoil*, *McDonnell Douglas 30P-30N multi-element airfoil*. The incompressible Reynolds Averaged Navier Stokes(RANS) equations, in conjunction with the Spalart-Allmaras turbulence model for turbulence closure, in primitive variables, have been solved using stabilized finite element formulations. Typical finite element mesh consists of structured mesh close to the body and an unstructured mesh, generated via, Delaunay's triangulation, in the rest of the domain. This type of grid has the ability of handling fairly complex geometries while still providing the desired resolution close to the body, to effectively capture the boundary layer and shear layer, especially in the context of unsteady flows. In addition, the structured grid around the body allows for efficient implementation of the turbulence model.

The results have been presented for turbulent computations. Flat plate results have been found to be in good agreement with the theoretical results with successful control over the trip locations. The flow phenomenon over NACA0012 airfoil has also been captured successfully. In the context of multi-element airfoil, the computed results have been presented at $Re = 9 \times 10^6$, for angle of attack varying from 8° to 27° . It has been found that the velocity profiles match quite well with the experimental results below the slat wake but gets diffused towards the downstream of the flow even at lower angle of attack. C_p distribution also matches quite well on the lower surface but shows a slight deviation on the upper surface at the higher angle of attack. Since the turbulence model is not able to capture the stall behaviour at higher angle of attack, the lift coefficient has been found over predicted in computations. The computations of slat flow field represents a key roadblock for successful prediction of multi-element flows.

Acknowledgements

A journey is easier when you travel together. Interdependence is certainly more valuable than independence. This thesis is the result of two years of work whereby I have been accompanied and supported by many people. It is a pleasant aspect that I have now the immense opportunity to express my sincere gratitude for all of them.

The first person whom I would like to thank is my supervisor Prof. Sanjay Mittal. I have been in his project since 2002 when I started my M.Tech program. During these years I have known him as a sympathetic and principle-centered person. His overly enthusiasm and integral view on research and his mission for providing 'only high-quality work and not less', has made a deep impression on me. I owe him lots of gratitude for having me shown this way of research. He could not even realize how much I have learned from him. Besides of being an excellent supervisor, he was as close as a relative and a good friend to me. I am really glad that I have come to get know him in my life.

I would like to thank all the faculty members of Aerospace Engineering Department who took effort in providing me with valuable knowledge, advices, and generous help on my academics. I also extend my thanks to the technical staff of the department for maintaining an excellent working environment.

My colleagues of the CFD Laboratory all gave me the feeling of being at home at work. Satya Prakash Singh, Bhaskar, Manish, Prasanth, Srinath, Anik, Rajarao, Balaji, many thanks for being my colleague. My special thanks to Satya Prakash Singh for our many discussions and providing me brotherly advices and tips that helped me a lot in staying at the right track.

In my opinion, doing a research is a sacred task and this was definitely one of the best decisions of my life. Additional energy and vitality for this research was provided externally through my involvement in several friendly activities. Thereby, it has played a substantial role and provided me the opportunity to meet many good friends. Natida, Sonada, Bhaipo, Sakila, Hulo, Avik, Tuhin, Gmon, Sumit, Gantuda, Pritam, Somnath, Santanu, Manas, Sutapadi, Indrani, Sidhu, Utsa, Kesta, Rakesh, I am really thankful to all of you for having shared many experiences and thoughts with me to make my stay at IIT Kanpur enjoyable and pleasant throughout the last two years.

The chain of my gratitude would be definitely incomplete if I would forget to mention the first cause of this chain, the silent support, good wishes and blessings of my parents and other family members still provide a persistent inspiration for my journey in this life.

Ashoke De

Contents

Certificate	i
Dedication	ii
Abstract	iii
Acknowledgements	iv
Contents	v
List of Figures	viii
List of Tables	xi
Nomenclature	xii
1 Introduction	1
1.1 Problem description	2
1.2 Literature survey	3
1.3 Thesis organization	6
2 An Overview of Turbulence Modeling	8
2.1 Statistical Turbulence Models	9

2.2	Integral Methods	10
2.3	Brief description of turbulence equations(RANS)	10
2.4	Classification of Turbulence models	13
2.5	Desirable features of Turbulence model	13
2.6	Spalart-Allmaras Turbulence Model	14
2.6.0.1	Advantages and Disadvantages of Spalart-Allmaras Model	19
3	Numerical Technique and Procedure	20
3.1	Mesh Design	22
3.2	Governing Equations	23
3.3	Finite Element Formulation	25
4	Results and Discussions	28
4.1	Flat Plate	29
4.1.1	Computational Domain & Boundary conditions	29
4.1.2	Turbulent calculation for different values of Re	30
4.2	NACA 0012 airfoil	35
4.2.1	Computational Domain & Boundary conditions	35
4.2.2	Finite element mesh and Results	35
4.3	McDonnell Douglas Multi-Element Airfoil	46
4.3.1	Airfoil configuration	46
4.3.2	Computational Domain and Boundary Conditions	46
4.3.3	Results	47
4.3.3.1	Pressure distribution	47
4.3.3.2	Velocity profiles	50
4.3.3.3	Force and Pitching moment	53
4.4	Convergence of GMRES solver	89

5	Conclusions	91
6	Scope for Future Work	93
	References	94

List of Figures

4.1	Flat plate configuration.	31
4.2	Variation of C_f along the length of the plate for $Re = 10^5$	31
4.3	Variation of C_f along the length of the plate for $Re = 10^6$	32
4.4	Variation of C_f (where flow trips by its own) along the length of the plate for $Re = 10^6$	33
4.5	Variation of turbulence index(i_t) along the length of the plate for $Re = 10^6$	34
4.6	Turbulent boundary layer velocity profile over flat plate at $Re = 10^6$	34
4.7	Finite element mesh for NACA 0012 airfoil at $\alpha = 10^0$	37
4.8	C_p distribution over NACA 0012 airfoil surface at different angle of attacks for $Re = 10^6$	38
4.9	Turbulent flow past a NACA 0012 airfoil at $Re = 10^6$: magnitude of velocity(left) and eddy viscosity(right) for various angle of attacks.	39
4.10	C_l, C_d, C_m versus angle of attacks for NACA 0012 airfoil at $Re = 10^6$	40
4.11	NACA 0012 airfoil: Variation of turbulence index over airfoil surface at $Re = 10^6$	41
4.12	NACA 0012 airfoil: Location of stations from the leading edge where velocity profile, over airfoil surface is shown.	42
4.13	NACA 0012 airfoil: Velocity profiles at different stations over airfoil surface for $\alpha = 5^0$	43
4.14	NACA 0012 airfoil: Velocity profiles at different stations over airfoil surface for $\alpha = 10^0$	44

4.15	NACA 0012 airfoil: Velocity profiles at different stations over airfoil surface for $\alpha = 15^0$	45
4.16	McDonnell Douglas Multi-Element Airfoil: Model geometry & Nomenclature (as given in the paper [17]).	55
4.17	Typical Finite Element Mesh shown for $\alpha = 15^0$, consists of 48760 nodes and 96615 elements.	56
4.18	Finite Element Mesh for $\alpha = 15^0$ showing close-up of main-element, slat and flap.	57
4.19	Pressure distribution over multi-element surfaces for $\alpha = 8^0$	58
4.20	Pressure distribution over multi-element surfaces for $\alpha = 15^0$	59
4.21	Pressure distribution over multi-element surfaces for $\alpha = 16^0$	60
4.22	Pressure distribution over multi-element surfaces for $\alpha = 19^0$, $Re = 7 \times 10^6$	61
4.23	Pressure distribution over multi-element surfaces for $\alpha = 19^0$, $Re = 9 \times 10^6$	62
4.24	Pressure distribution over multi-element surfaces for $\alpha = 21^0$	63
4.25	Pressure distribution over multi-element surfaces for $\alpha = 27^0$	64
4.26	Multi-Element Airfoil: Location of stations from leading edge, for showing velocity profiles.	65
4.27	Multi-element airfoil: Contours of velocity magnitude, pressure fields, eddy viscosity for mesh1 at $\alpha = 8^0$, $Re = 9 \times 10^6$	66
4.28	Multi-element airfoil: Contours of velocity magnitude, pressure fields, eddy viscosity for mesh2 at $\alpha = 8^0$, $Re = 9 \times 10^6$	67
4.29	Multi-element airfoil: velocity distribution at $\alpha = 8^0$, $Re = 9 \times 10^6$	68
4.30	Multi-element airfoil: Contours of velocity magnitude, pressure fields, eddy viscosity at $\alpha = 15^0$, $Re = 9 \times 10^6$	69
4.31	Multi-element airfoil: velocity distribution on main element at $\alpha = 15^0$, $Re = 9 \times 10^6$	70
4.32	Multi-element airfoil: velocity distribution on flap at $\alpha = 15^0$, $Re = 9 \times 10^6$	71
4.33	Multi-element airfoil: Contours of velocity magnitude, pressure fields, eddy viscosity at $\alpha = 16^0$, $Re = 9 \times 10^6$	72

4.34	Multi-element airfoil: velocity distribution at $\alpha = 16^0$, $Re = 9 \times 10^6$.	73
4.35	Multi-element airfoil: Contours of velocity magnitude, pressure fields, eddy viscosity at $\alpha = 19^0$, $Re = 7 \times 10^6$.	74
4.36	Multi-element airfoil: velocity distribution on main element at $\alpha = 19^0$, $Re = 7 \times 10^6$.	75
4.37	Multi-element airfoil: velocity distribution on flap at $\alpha = 19^0$, $Re = 7 \times 10^6$.	76
4.38	Multi-element airfoil: Contours of velocity magnitude, pressure fields, eddy viscosity at $\alpha = 19^0$, $Re = 9 \times 10^6$.	77
4.39	Multi-element airfoil: velocity distribution on main element at $\alpha = 19^0$, $Re = 9 \times 10^6$.	78
4.40	Multi-element airfoil: velocity distribution on flap at $\alpha = 19^0$, $Re = 9 \times 10^6$.	79
4.41	Multi-element airfoil: Contours of velocity magnitude, pressure fields, eddy viscosity for mesh1 at $\alpha = 21^0$, $Re = 9 \times 10^6$.	80
4.42	Multi-element airfoil: Contours of velocity magnitude, pressure fields, eddy viscosity for mesh2 at $\alpha = 21^0$, $Re = 9 \times 10^6$.	81
4.43	Multi-element airfoil: velocity distribution at $\alpha = 21^0$, $Re = 9 \times 10^6$.	82
4.44	Multi-element airfoil: Contours of velocity magnitude, pressure fields, eddy viscosity at $\alpha = 27^0$, $Re = 9 \times 10^6$.	83
4.45	Multi-element airfoil: velocity distribution on main element at $\alpha = 27^0$.	84
4.46	Multi-element airfoil: velocity distribution on flap at $\alpha = 27^0$.	85
4.47	Multi-element airfoil: C_l Vs angle of attack at $Re = 9 \times 10^6$.	86
4.48	Multi-element airfoil: C_d Vs angle of attack at $Re = 9 \times 10^6$.	87
4.49	Multi-element airfoil: C_m Vs angle of attack at $Re = 9 \times 10^6$.	88

List of Tables

4.1	Number of nodes and elements in different meshes used for turbulent calculation of flow past a flat plate.	30
4.2	Number of nodes and elements in NACA mesh at different angle of attack.	35
4.3	NACA 0012 airfoil: Location of stations from leading edge for showing velocity profiles.	36
4.4	Slat and Flap setting of Multi-Element airfoil	46
4.5	Number of nodes and elements in Multi-Element mesh at different angle of attack.	47
4.6	Multi-element airfoil: Location of stations from leading edge for showing velocity profiles.	50

Nomenclature

A	Reference area
c	Chord length of airfoil
C_p	Pressure coefficient
C_d	Drag coefficient
C_l	Lift coefficient
C_m	Moment coefficient
C_f	Skin-friction coefficient
$c_{b1}, c_{b2}, c_{t1}, c_{t2}$	Empirical constants in the turbulence model
c_{w1}, c_{w2}, c_{w3}	Empirical constants in the turbulence model
c_{r1}, c_{r2}, c_{r3}	Empirical constants in the turbulence model
d	Distance to the wall
D	Drag force
\mathbf{f}	Force vector
$f_w, f_{v1}, f_{v2}, g_{t1}$	Empirical functions in turbulence model
f_{t1}, f_{t2}	Trip functions in the turbulence model
f_{r1}	Rotation/curvature correction function in the turbulence model
g, r, \bar{S}	Intermediate variables in the turbulence model
h	Element length
$\mathbf{H}^{1h}(\Omega)$	Finite dimensional function space over Ω
i_t	Turbulence index
l	Mixing length
L	Lift force
M	Pitching moment
n_{sd}	Number of space dimensions
n_{el}	Number of elements

p	Pressure
\bar{p}	Mean component of pressure
p'	Fluctuating component of pressure
Re	Reynolds number
r^*, \bar{r}	Nondimensional parameters for rotation effects in turbulence model
St	Stanton number
S_{ij}	Strain-rate tensor
S	Measure of deformation tensor
T	Temperature
\bar{T}	Mean component of temperature
T'	Fluctuating component of temperature
\mathbf{u}	Velocity vector
u	Velocity in x direction
\bar{u}	Mean component of velocity in x direction
u'	Fluctuating component of velocity in x direction
\bar{u}_i, \bar{u}_j	Components of the mean velocity vector
u_τ	Friction velocity
v	Velocity in y direction
\bar{v}	Mean component of velocity in y direction
v'	Fluctuating component of velocity in y direction
w	Velocity in z direction
\bar{w}	Mean component of velocity in z direction
w'	Fluctuating component of velocity in z direction

Greek symbols

α	Angle of attack
χ	Intermediate variable in the turbulence model
δ^*	Displacement thickness
δ	Thickness of shear layer
δ_i	Kronecker delta
ϵ	Turbulent dissipation rate
$\epsilon_{imn}, \epsilon_{jmn}$	Tensor of Levi-Civita
κ	Kármán constant
ρ	Density of the fluid
$\bar{\rho}$	Mean component of density

ρ'	Fluctuating component of density
Γ	Boundary on Ω
Γ_g, Γ_h	Complementary subsets of the boundary Γ
μ	Molecular viscosity
μ_t	Turbulent viscosity
ν	Kinematic molecular viscosity
ν_t	Kinematic turbulent, or eddy, viscosity
$\bar{\nu}$	Working variable of the turbulence model
$ \omega $	Magnitude of vorticity
ω_{ij}	Components of the vorticity tensor
Ω_m	Components of the system rotation tensor
Ω	Physical domain of calculation
Ω^e	Interior domain of an element
σ	Stress tensor
σ'	Turbulent Prandtl number
$\mathcal{S}_u^h, \mathcal{S}_p^h, \mathcal{S}_{\bar{\nu}}^h$	Finite element trial function spaces
$\mathcal{V}_u^h, \mathcal{V}_p^h, \mathcal{V}_{\bar{\nu}}^h$	Finite element weighting function spaces
θ	Momentum thickness
τ_{ij}	Viscous stress tensor

Acronyms

<i>BB</i>	Baldwin-Barth
<i>BL</i>	Baldwin-Lomax
<i>CFD</i>	Computational Fluid Dynamics
<i>DNS</i>	Direct Numerical Simulation
<i>FEM</i>	Finite Element Method
<i>GMRES</i>	Generalized Minimal RESidual
<i>LTPT</i>	Low Turbulence Pressure Tunnel
<i>LES</i>	Large Eddy Simulation
<i>MD</i>	McDonnell Douglas
<i>PSPG</i>	Pressure-Stabilizing Petrov-Galerkin
<i>RST</i>	Reynolds stress transport
<i>RANS</i>	Reynolds Averaged Navier-Stokes Equations
<i>SA</i>	Spalart-Allmaras
<i>SUPG</i>	Streamline-Upwind Petrov-Galerkin

Chapter 1

Introduction

High-lift aerodynamics has received considerable attention in last few years. A number of conferences and workshops have been held on high-lift problems to search for better computational and experimental tools. Also significant research works are in progress to resolve the difficulties, while the prediction of high-lift flow-fields consisting of multiple airfoil elements still remains a challenge to the computational fluid dynamics (CFD) community. Multi-element airfoil has wide variety of flow physics which requires accurate modeling. Each airfoil element has a stagnation point and boundary layers that developed along a curved surface in pressure gradients and may pass through various transition of laminar to turbulent flow. Additionally, the wake of each element eventually merges with the boundary layer, developed from subsequent elements. Hence keeping the slat wake distinct from the main element boundary layer for the greatest distance on the main element is one of the key ingredients of high lift multiple element design.

The factors affecting the design of multi-element airfoil namely, pressure distribution over surfaces and the flow around the slat, is also quite complex. The upper surface of the slat is highly curved with large flow acceleration, whereas the flow at the slat trailing edge can be laminar, transitional, or turbulent. On the other hand, the slat lower surface is highly concave and a result of that the flow in the lower side is accelerated through the slat-main element gap around a very sharp bend. The flow often separates due to the slat geometry and reattached near the slat trailing edge. The free shear layer developed at the recirculation boundary is most likely turbulent. The wake, developed at the trailing edge of the slat, is created from the laminar, transitional, or turbulent

upper surface flow and the turbulent lower surface flow. Additionally, the flow around the lower surface may be unsteady.

Therefore, the predictive capability for high lift multi element airfoil configurations is dependent on the accurate modeling of (i) boundary layer transition on a curved surface in a strong pressure gradients (ii) turbulent boundary layer development on a curved surface in a strong pressure gradient (iii) transitional and turbulent wake development (iv) separating and reattaching flow and (v) wind tunnel effects.

To achieve the goal of a high-lift system, generating as much lift as possible, the flow should remain attached to the airfoil surface. This can be achieved effectively by using multiple elements instead of using any external devices such as wall suction. Multi-element geometry provides a greatest advantage of getting high-lift through inviscid pressure distribution over surfaces by reducing the pressure rise over each element. However, the presence of multiple elements complicates the analysis procedures because of important and often complex interactions between the individual elements. While inviscid analysis can be done using panel methods or unstructured grid Euler solvers. But the accurate prediction of the flows about these configurations requires viscous analysis which can have large influences on the pressure distributions. As a result, these have obvious effects such as separation on the surfaces, wake interactions between forward and aft elements as well as flow reversal off the surface, can contribute in determining the overall performance of the high-lift system significantly.

The simulation of real flows, viscous in nature, has become a complicated task and hence the solution of Navier Stokes equation is essential to capture the effects of viscosity such as skin friction drag and heat transfer coefficient. Furthermore, in the real world problems involving high *Reynolds number* as those in aerospace applications, the flow is turbulent in nature.

1.1 Problem description

Multi-element airfoil has important applications in high-lift systems, typically for present transport airplanes, often consisting of a leading edge slat and a trailing edge flap system. The analysis brings forth unexpected complexities in flow structures. The objective

of the present thesis is to develop a tool for analysis of such flows and their physical understanding.

The present study is concerned with the high *Reynolds number* flows obtained from two-dimensional numerical computations. The unsteady incompressible Reynolds Average Navier Stokes (RANS) equations, in conjunction with Spalart-Allmaras model for turbulence closure in primitive variable formulation have been solved on hybrid mesh with triangular elements using a well proved stabilized finite element method with the SUPG(streamline-upwind/Petrov-Galerkin) and PSPG(pressure-stabilizing/Petrov-Galerkin) stabilization terms. The resulting nonlinear equation system has been solved using Generalized Minimal RESidual (GMRES) technique in conjunction with diagonal pre-conditioners.

Results have been compared with other published results in the open literature. The effect of spatial resolution has also been investigated. The flow problem considered in the present thesis are turbulent computations over (a) flat plate, (b) NACA 0012 airfoil ($Re = 10^6$), and (c) 30P-30N multi-element airfoil ($Re = 9 \times 10^6$).

1.2 Literature survey

The literature pertaining to flow past multi-element airfoil is reviewed below. The review of earlier investigations related to the different aspects of the flows for high Reynolds number has also been presented. A brief review on the modeling aspects of turbulent flow has also been undertaken to examine the performance of various turbulence models for complex geometries.

Some important insight into the physical processes that govern the high-lift aerodynamics were summarized by Smith in his landmark paper [1]. In particular he described several effects that contribute to the improvement of high lift characteristic of multiple elements over single element.

Turbulence modeling is an important issue in solving flows past complex geometries. The various length scales must be resolved properly. Tulapurkara [2] gave an extensive review on the development and application of turbulence models to aerospace

applications. Spalart-Allmaras [3] proposed a one-equation turbulence model. This is one of the most widely used model for aerodynamic flows in recent times. They came out with some advantages over Baldwin-Barth's model. Thereafter, Spalart-Shur [4, 5] came out with a proposal for sensitization of the model to rotation and curvature effects.

Anderson et. al. [6] utilized a two-dimensional unstructured Navier-Stokes code for computing the flow around multi-element configurations using both Baldwin-Barth and Spalart-Allmaras turbulence models. Comparisons had been shown for a landing configuration with an advanced-technology flap. They also showed the comparisons between experimental & computed results and the grid convergence studies to assess inaccuracies caused by inadequate grid resolution. They concluded from the grid convergence study that sufficient grid refinement is required to obtain suitable levels of grid convergence for velocity profiles at high angle of attacks, while adequately small spacing of grid points to be maintained for obtaining accurate resolution of the wall boundary layers on upstream elements.

Godin et. al. [7] reported detailed comparison of the Spalart-Allmaras and Menter turbulence models in the context of two-dimensional high-lift aerodynamic flows. Their results showed that the Menter model to be more accurate in separated flow regions, whereas the Spalart-Allmaras model is more accurate in attached flows and wakes, including merging boundary layers and wakes. The Spalart-Allmaras model is somewhat more robust, though for several cases the computational costs were about equal.

Rango and Zingg [8] investigated the flow over multi-element airfoil configurations using higher-order methods on multi-block grids, in conjunction with Spalart-Allmaras turbulence model. They performed grid convergence study to evaluate the accuracy of the higher-order algorithm on multi-block grids and showed that the globally higher-order approach can provide accuracy equivalent to a second-order algorithm on a grid with several times fewer nodes, thus greatly reducing the cost of computing flows over multi-element airfoils.

Rumsey and Gatski [9] applied the Spalart-Allmaras model with curvature corrections to simulate the flow over multi-element airfoil. Their investigations showed that implementation of curvature term does not have much impact on flow field.

Rumsey et. al. [10] demonstrated the need to include the transition location in

addition to study of various turbulence models. They studied the McDonnell Douglas three element high lift configuration tested in NASA Langley LTPT (Low turbulence Pressure Tunnel) wind tunnel. They derived a conclusion from their study that transition location is crucial to the accurate computation of boundary layer velocity profiles. Otherwise poor boundary-layer profile predictions lead to poor predictions of trailing-edge near-wake profiles and, therefore, poor predictions in the far-wake region. They also demonstrated their efforts in understanding the flow over slat by specifying transition on the slat resulted either in slat separation or in only marginal improvement in slat-wake profiles compared to the experimental results.

Kim and Nakahashi [11] solved RANS on the unstructured grid for computing flows over multi-element airfoil configuration. They compared their results with the experimental data to assess the accuracy of the computations. They also discussed the effect of complex flow phenomenon around high-lift system, like the interaction between upstream element wakes and boundary layers on downstream elements, on the solution accuracy using the grid refinement method.

Valarezo and Mavriplis [12] presented the application of compressible RANS method to the calculation of flows about a transport-type multi-element airfoil. They used unstructured-mesh method utilizing multi grid techniques for computational efficiency in the context of different turbulence models. They discussed the usability of such method to capture performance increments due to rigging changes and Reynolds number effects and suggested to consider grid adaptation for extensions to three-dimensional flows.

Joseph H. Morrison [13] performed the calculations with Reynolds averaged Navier-Stokes code ISAAC to study the effect of numerical accuracy on the advection terms of the turbulence equations and the performance of several turbulence models. Also the effect of transition location was investigated. His results estimated too large wake defect in all the models and finally suggested to go for improved transition model.

Jones et. al. [14] discusses the multi zonal grid technique for analyzing the multi-element airfoil. Grid resolution is an important aspect to capture the shear layer of each element and for that they conducted grid refinement study and found dramatic effect on the downstream flow field velocity profiles.

Rogers et. al. [15] reported the comparison of various turbulence models in com-

puting multi-element airfoil flows with the experimental results. Their results showed very little difference in C_p distribution in the context of various models. They also reported that Spalart-Allmaras(SA) model appeared to have the most amount of mixing in the wakes, while Shear stress transport(SST) model consistently showed the greatest amount of velocity defect in the wakes. According to their results, SA model was the only one to show a stall behaviour below an angle of attack of 25 degrees, this may be due its treatment in transition. The most significant thing observed in their study is that the difference between the computational and the experimental data in the slat wake at lower angle of attack. The grid resolution study showed that this difference did not decrease with increased grid resolution. They finally concluded that all the models are similar for most part of the predictions but given the complexity of the multi-element airfoil geometry and the surrounding flow field, further development and tuning of turbulence models were suggested. Nakayama et. al. [16] did experimental investigation of flow field about multi-element airfoil to measure the mean flow and turbulence quantities using pressure and hot-wire probes.

Experiments have also been performed in NASA LTPT on McDonnell Douglas three element landing configuration, which was used as a test cases in a CFD challenge workshop discussed in [17] held at NASA. The conclusions drawn on the workshop were (i) RANS showed less variability than did potential/Euler solvers coupled with boundary-layer solution techniques, (ii) Coupled-methods drag prediction agreed more closely with experiment than the RANS methods. Lift was more accurately predicted than drag in both methods, (iii) Both the methods did reasonably well in predicting lift and drag due to changes in Reynolds number, (iv) Pressure and skin friction were also in good agreement with the experimental results, and finally it was suggested to have accurate transition locations since it appeared to have a major influence on overall airfoil performance.

1.3 Thesis organization

Reynolds Averaged Navier-Stokes equation have been presented in chapter2, followed by an introduction to turbulence modeling. The Spalart-Allmaras turbulence model has also been described in the same chapter. The details of numerical techniques, governing

equations and formulations with the different boundary conditions including the grid system used here have been presented in Chapter3. Chapter4 describes the results of the present research and related discussions. Chapter5 summarizes major conclusions of the present work. The scope for future work has been enlisted in Chapter6.

Chapter 2

An Overview of Turbulence Modeling

Newtonian fluid flow is now understood to be fully represented by the Navier-Stokes equations. Numerical solution of Navier-Stokes equations is thus a successful modeling tool for laminar and turbulent flows. If turbulent flow is computed using the same grid and time as in laminar flow, the solutions will not reveal the existence of the small scale eddies. Hence, the transport of turbulent kinetic energy from the larger to the smaller eddies will not be addressed. Nevertheless, the Navier-Stokes equations can be solved on a fine enough grid with an exceptionally accurate discretization method so that both fine scale and large scale aspects of turbulence can be calculated. This approach is termed as the *Direct Numerical Simulation*(DNS) of turbulence. DNS has been a very successful tool over the past ten years for the study of turbulent flow physics. It has however a severe limitation. In order to resolve all scales of motion, one requires a very large amount of computing resources.

In *Large-Eddy Simulation*(LES) the small scales of turbulence, which are assumed to be more universal in nature, are modeled; the large, energy-containing scales that are more flow specific are explicitly calculated. The models used for the small scales are called sub grid-scale(SGS) models. Unlike other types of turbulence models, the resultant equations for LES describe a fully time-dependent flow; the modeling only blurs the turbulent structures so that the small scales do not need to be calculated. Like the DNS, the LES also requires enormous computing resources for solving practical flow

problem. A potential exists for the practical use of LES & DNS in the near future, although the high cost will restrict its use to cases where lower order models are not expected to give satisfactory results.

2.1 Statistical Turbulence Models

Presently, statistical turbulence models are the most widely used turbulence-modeling schemes. Flow quantities are decomposed into mean and fluctuating parts and then substituted into the equations of motion. These equations are averaged to produce a set of equations for the mean motion. Osborne Reynolds [24] pioneered this approach by temporally averaging the equations for incompressible flow; the resultant equations are known as the Reynolds-averaged Navier-Stokes(RANS) equations. These equations involve the mean flow quantities as well as correlations of the fluctuating quantities. The correlations appear in the equations of mean motion in the same way as the viscous stress terms appear; hence, these correlations are known as the Reynolds stresses. The various classes of models differ in how these correlations are approximated.

Reynolds stress transport(RST) models involve transport equations for each of the six independent Reynolds stress components. This class of models is the most complex of the statistical turbulence models, and the use of these models for engineering applications is not yet commonplace. However, because the Reynolds stresses can independently respond to various flow conditions, this class of models can potentially be applied to a large variety of flows. This potential generality motivates much of the current research on these models.

Eddy-viscosity models include a number of classes of models, all of which approximate the effect of the turbulence on the mean motion by modifying the coefficient of viscosity. The effective viscosity coefficient that issued in the computation of the flow field is the sum of the molecular viscosity(μ) and turbulent viscosity(μ_t). The different classes of eddy-viscosity models are distinguished by the number of additional differential equations that are solved to determine μ_t . Dimensional analysis suggests that μ_t is the product of the density, a velocity scale, and a length scale. The local mean density is almost always used, leaving the velocity and length scale still to be determined. Two-equation models solve differential equations to determine these two scales. One-equation

models solve a differential equation for the velocity scale and use algebraic relations to determine the length scale. Zero-equation models use algebraic relations to determine both the velocity and length scales. More detail on all of these model classes are given in books.

2.2 Integral Methods

In integral methods, an ordinary differential equation is solved for the momentum thickness(θ) in terms of the skin-friction coefficient(C_f), the displacement thickness(δ^*), the boundary-layer edge velocity, and body curvature. For flows with heat transfer, another equation is required that involves the Stanton number(S_t), the enthalpy thickness, the free-stream and wall temperatures, and the body geometry. Approximate relationships between the variables are substituted into the equations. The equations are integrated in the downstream direction. These methods are computationally quite efficient, but are accurate only for those flows in which the assumed relationships are appropriate. Of the 20 integral methods that competed in the 1968 Stanford Conference([25], [26]), only four received an evaluation of "good" after they were tested for 16 different turbulent flows. In spite of their limited generality, integral methods provide good skin-friction and heat-transfer predictions for well-studied flows of engineering interest. This method is discussed in more details in book [38].

2.3 Brief description of turbulence equations(RANS)

The unsteady Navier-Stokes equations are generally considered to govern the turbulent flows in the continuum regime. Turbulent flow, shows irregular fluctuation in the flow variables, are superimposed on the mean flow. Therefore, the mathematical description of turbulent flow, consists of decomposing the flow variables like velocity, pressure, density, temperature etc. into mean and fluctuating components(called as *Reynolds decomposition*) are defined as follows.

Now by time averaging the N-S Equations, and taking into account the basic rules for fluctuating components, we obtain RANS Equations:

$$\frac{\partial}{\partial x_i}(\bar{u}_i) = 0 \quad (2.3.5)$$

$$\frac{\partial}{\partial t}(\bar{u}_i) + \frac{\partial}{\partial x_j}(\bar{u}_i \bar{u}_j) = -\frac{\partial \bar{p}}{\partial x_i} + \frac{\partial}{\partial x_j}(\bar{\tau}_{ij} - \overline{\rho u'_i u'_j}) \quad (2.3.6)$$

For the present cases, in the limit $M \rightarrow 0$ the governing equations are incompressible in nature i.e. density ρ is constant and the energy equation is decoupled. Hence, the continuity and momentum equations become

$$\frac{\partial \bar{u}_i}{\partial x_i} = 0 \quad (2.3.7)$$

$$\frac{\partial}{\partial t}(\bar{u}_i) + \frac{\partial}{\partial x_j}(\bar{u}_i \bar{u}_j) = -\frac{\partial \bar{p}}{\partial x_i} + \frac{\partial}{\partial x_j}(\bar{\tau}_{ij} - \overline{\rho u'_i u'_j}) \quad (2.3.8)$$

where

$$\bar{\tau}_{ij} = \mu \left[\left(\frac{\partial \bar{u}_i}{\partial x_j} + \frac{\partial \bar{u}_j}{\partial x_i} \right) - \frac{2}{3} \delta_{ij} \frac{\partial \bar{u}_k}{\partial x_k} \right] \quad (2.3.9)$$

The Reynolds stress tensor is given by:

$$\begin{pmatrix} \sigma'_x & \tau'_{xy} & \tau'_{xz} \\ \tau'_{xy} & \sigma'_y & \tau'_{yz} \\ \tau'_{xz} & \tau'_{yz} & \sigma'_z \end{pmatrix} = -\rho \begin{pmatrix} \overline{u'^2} & \overline{u'v'} & \overline{u'w'} \\ \overline{u'v'} & \overline{v'^2} & \overline{v'w'} \\ \overline{u'w'} & \overline{v'w'} & \overline{w'^2} \end{pmatrix}$$

Thus the mean momentum equation is complicated by new term involving the turbulent inertia tensor $\overline{u'_i u'_j}$. This new term may not be negligible in a turbulent flow, in general, and is the source of analytic difficulties. The components of $\overline{u'_i u'_j}$ are related not only to fluid physical properties but also to local flow conditions(velocity, geometry, surface roughness, and upstream history). If we observe equation 2.3.8 then, a turbulent inertia term behaves as if the total stress on the system were composed of the Newtonian viscous stresses plus an additional or apparent turbulent stress tensor which arises from the fluctuating terms. These turbulence-correlation terms must be modeled with semi empirical assumption, which leads to idea of turbulence modeling. With the above background information, the turbulence models are categorized.

2.4 Classification of Turbulence models

The turbulence models can be classified depending on the number of differential equations solved in addition to the mean flow equations:

1. Zero equation models - Algebraic models.
2. One equation models.
3. Two equation models.
4. Stress equation models.

Models in class 1-3 are based on Boussinesq eddy viscosity model, while those in 4 obtain the Reynolds stress solving differential equation for $\overline{u'v'}$ directly. Zero equation models, which uses only the partial differential equation for the mean flow field and no transport equations for turbulence quantities, is also called "mean field" closure. The class 2-4 are called "transport equation" closures, as they takes into account the transport phenomena involved.

2.5 Desirable features of Turbulence model

The turbulence models provide the equations necessary to make the Reynolds Averaged Navier Stokes equations a closed set. The turbulence model should have the following features :

- predict accurately a wide range of flows;
- be mathematically simple and involve small number of assumptions and model constants;
- be computationally stable and economical in computational time.
- be dimensionally correct.

2.6 Spalart-Allmaras Turbulence Model

This model was proposed by Spalart and Allmaras [3]. The proposition of this model was prompted by Baldwin and Barth's [27] work, and by the belief that generating a One-equation model as a simplified version of the $\kappa - \epsilon$ model is not optimal. A one-equation model is simple enough that it can be generated "from scratch", which may lead to better performance and certainly gives fuller control over its mechanics. A case in point is the Baldwin-Barth diffusion term, which constrained by the $\kappa - \epsilon$ ancestry and the further assumptions made. This model allows a "semi-local" near-wall term, also has the same properties as that of Baldwin-Barth in terms of compatibility with unstructured grids and benign near-wall behavior, and is more accurate, especially away from wall, as well as slightly more robust.

The model has four nested versions from the simplest, applicable only to free shear flows, to the most complete, applicable to viscous flows past solid bodies and with laminar regions. As each additional physical effect is considered, new terms or factors are introduced. They are identified by a common letter subscript in the constants and functions involved. The new terms are passive in all lower versions of the model, so that the description proceeds in order.

Free shear flows

The central quantity is the eddy viscosity ν_t ; the Reynolds stresses are given by the constitutive relation $-\overline{u_i u_j} = 2\nu_t S_{ij}$. For generating transport equation for ν_t at high Re , the molecular viscosity is not incorporated here. The left hand side of the equation is the Lagrangian or material derivative of ν_t : $D\nu_t/Dt \equiv \partial\nu_t/\partial t + U_i \partial\nu_t/\partial x_i$ and on the right hand side the production and diffusion terms are provided.

For the production term, the deformation tensor $\partial U_i/\partial x_j$ presents itself. Since ν_t is a scalar, the scalar measure of the tensor is needed, denoted by S , defined as magnitude of the vorticity ($|\omega|$), and then $S\nu_t$ has the desired dimension. The production term, and in fact the restriction of the model to homogeneous turbulence, is

$$\frac{D\nu_t}{Dt} = c_{b1} S \nu_t \quad (2.6.10)$$

The subscript b stands for "basic". The eddy viscosity is stationary in isotropic turbu-

lence (*i.e.* $D\nu_t/Dt = 0$, since $S = 0$). The calibration of the model on inhomogeneous flows yields values of c_{b1} between 0.13 and 0.14.

The diffusion terms naturally focuses on spatial derivatives of ν_t . Incorporating the non-conservative diffusion term, involving first derivatives of ν_t , the "basic" model defined as

$$\frac{D\nu_t}{Dt} = c_{b1}S\nu_t + \frac{1}{\sigma'} \left[\nabla \cdot (\nu_t \nabla \nu_t) + c_{b2} (\nabla \nu_t)^2 \right] \quad (2.6.11)$$

where the constants are defines as $\sigma' = 2/3$, $c_{b1} = 0.1355$, $c_{b2} = 0.622$.

Near-wall region, high Reynolds number

In a boundary layer the blocking effect of a wall is felt at a distance through the pressure term, which acts as the main destruction term for the Reynolds shear stress. This suggests a destruction term in the transport equation for the eddy viscosity. Dimensional analysis leads to a combination $-c_{w1}(\nu_t/d)^2$ as a starting point, where d is the distance to the wall. The subscript w stands for a "wall". This term is passive in free shear flows ($d \gg \delta$, so that the new term is much smaller than the diffusion term) and therefore does not interfere with the calibration upto this point. the idea of near-wall, but not viscous, "blocking" term is also defined in other literatures. It is related to algebraic models, which takes the smaller of two eddy viscosities. In these models the outer eddy viscosity scales with the boundary-layer thickness, and the inner eddy viscosity is given by the mixing length, $l \propto d$. In a classical log layer it is found that $S = u_\tau/(\kappa d)$ and $\nu_t = u_\tau \kappa d$ follow these relationships. Equilibrium between the production and diffusion terms(all positive) and the destruction term is possible provided $c_{w1} = c_{b1}/\kappa^2 + (1 + c_{b2})/\sigma'$.

Tests show that the model, when equipped the destruction term, can produce an accurate log layer in a $U^+(y^+)$ plot (this requires an adequate treatment of the viscous region, which is described later on). On the other hand it produces too low a skin-friction coefficient in a flat-plate boundary layer. This shows that the destruction term as formulated above decays too slowly in the outer region of the boundary layer. To address this deficiency and allow a new calibration, the term is multiplied by a non-dimensional function f_w , which equals 1 in log layer. With these modifications the model becomes

$$\frac{D\nu_t}{Dt} = c_{b1}S\nu_t + \frac{1}{\sigma'} \left[\nabla \cdot (\nu_t \nabla \nu_t) + c_{b2} (\nabla \nu_t)^2 \right] - c_{w1}f_w \left[\frac{\nu_t}{d} \right]^2 \quad (2.6.12)$$

The choice of an argument for f_w was inspired by algebraic models, in which the mixing length plays a major role near the wall. This length can be defined by $l \equiv \sqrt{(\nu_t/S)}$ and the square of $l/\kappa d$ is considered for convenience:

$$r \equiv \frac{\nu_t}{S\kappa^2 d^2} \quad (2.6.13)$$

$$f_w(r) = g \left[\frac{1 + c_{w3}^6}{g^6 + c_{w3}^6} \right]^{1/6}, \quad g = r + c_{w2} (r^6 - r) \quad (2.6.14)$$

with the constants as $\kappa = 0.41$, $c_{w2} = 0.3$, $c_{w3} = 2.0$

Near-wall region, finite Reynolds number

In buffer layer and viscous sublayer, additional notation is needed. Besides the wall unit, y^+ and so on, $\bar{\nu}$ is introduced which is equal to ν_t except in the viscous region. Also χ follows the relationships: $\chi = \kappa y^+$ from wall to the log layer. The transported quantity $\bar{\nu}$ behaves linearly near the wall. This is beneficial for numerical solutions: $\bar{\nu}$ is actually easier to resolve than U itself, in contrast with ϵ , for instance. Therefore, the model will not require a finer grid than an algebraic model would. To arrive at this behavior, the classical law of the wall is considered and devised near-wall "damping functions" which are distinct from the f_w near-wall non-viscous destruction term.

The eddy viscosity ν_t equals $\kappa y u_\tau$ in the log layer, but not in the buffer layer and viscous sublayer. $\bar{\nu}$ is defined in such a way that it equals $\kappa y u_\tau$ all the way to the wall. This leads to

$$\nu_t = \bar{\nu} f_{v1}, \quad f_{v1} = \frac{\chi^3}{\chi^3 + c_{v1}^3} \quad (2.6.15)$$

The subscript v stands for "viscous" and c_{v1} contains a value of 7.1.

To modify the production term, S is replaced with \bar{S} , given by

$$\bar{S} \equiv S + \frac{\bar{\nu}}{\kappa^2 d^2} f_{v2}, \quad f_{v2} = 1 - \frac{\chi}{1 + \chi f_{v1}} \quad (2.6.16)$$

The function f_{v2} is constructed, just like f_{v1} , so that \bar{S} maintains its log-layer behavior ($\bar{S} = u_\tau / (\kappa y)$) all the way to the wall. So, the other quantities involved in the "inviscid" model are redefined in the terms of $\bar{\nu}$ instead of ν_t , for instance $r \equiv \bar{\nu} / (\bar{S} \kappa^2 d^2)$. Finally viscous diffusion term is added, consistent with a Dirichlet boundary condition at the wall,

$\bar{\nu} = 0$. And the transport equation has become

$$\frac{D\bar{\nu}}{Dt} = c_{b1}\bar{S}\bar{\nu} + \frac{1}{\sigma'} \left[\nabla \cdot ((\nu + \bar{\nu}) \nabla \bar{\nu}) + c_{b2} (\nabla \bar{\nu})^2 \right] - c_{w1} f_w \left[\frac{\bar{\nu}}{d} \right]^2 \quad (2.6.17)$$

This equation now yields equilibrium ($D\bar{\nu}/Dt = 0$) all the way $d = 0$ in a classical law-of-the-wall situation.

Laminar region and trip term

The final set of terms provide control over the laminar regions of the shear layers, which has two aspects: keeping the flow laminar where desired, and obtaining transition where desired.

The turbulence index, $i_t \equiv \frac{1}{\kappa u_\tau} \frac{\partial \bar{\nu}}{\partial n}$ (where $u_\tau \equiv \sqrt{(\nu | \omega |)}$), determines the transition near a wall. This index attains an approximate value of 0 & 1 in a laminar and turbulent region, respectively. In laminar region $\bar{\nu}$ is less than about ν and the production term is multiplied by a factor $(1 - f_{t2})$, where

$$f_{t2} = c_{t3} \exp(-c_{t4} \chi^2) \quad (2.6.18)$$

The subscript t stands for "trip" and the constants are having the value of $c_{t3} = 1.2$, $c_{t4} = 0.5$. In all case c_{t3} must be larger than 1. Particularly for boundary layer calculation the f_{t2} term can be left out by assigning $c_{t3} = 0$.

To initiate transition near the specified trip points in a smooth manner, a source term needs to be added that will be non zero in a small domain of influence and this domain should not extend outside the boundary layer. Not wanting to find this edge, nor violating the invariance principles, two quantities ($\Delta U, \omega_t$) are invoked, where ΔU is the norm of the difference between the velocity at the trip (i.e. usually zero since the wall is not moving) and that at the considered field point. ω_t is the vorticity at the wall at the trip point. Also d_t , the distance from the field point to the closest trip point or line, is introduced. Dimensional analysis points to ΔU^2 as a starting point for the source term, and the final equation becomes

$$\frac{D\bar{\nu}}{Dt} = c_{b1} [1 - f_{t2}] \bar{S}\bar{\nu} + \frac{1}{\sigma'} \left[\nabla \cdot ((\nu + \bar{\nu}) \nabla \bar{\nu}) + c_{b2} (\nabla \bar{\nu})^2 \right] - \left[c_{w1} f_w - \frac{c_{b1}}{\kappa^2} f_{t2} \right] \left[\frac{\bar{\nu}}{d} \right]^2 + f_{t1} \Delta U^2 \quad (2.6.19)$$

with

$$f_{t1} = c_{t1} g_{t1} \exp \left(-c_{t2} \frac{\omega_t^2}{\Delta U^2} [d^2 + g_t^2 d_t^2] \right) \quad (2.6.20)$$

and $g_t \equiv \min(0.1, U/\omega_t \Delta x_t)$, where x_t is the grid spacing along the wall at the trip, whereas the constants c_{t1}, c_{t2} hold the value 1.0 & 2.0, respectively. The Gaussian in f_{t1} confines the domain of influence of the trip terms as needed; it is roughly a semi-ellipse.

In the present code, the trip terms have not been employed except flat plate calculations. So, the resultant equation effectively solved, is equation 2.6.17.

Curvature effects

The implementation of curvature terms to the one-equation Spalart-Allmaras model lead to a fairly simple modification of the original model. The only difference between the modified model, accounting for the rotation-curvature effects and the SA model is that in the former the production term in the eddy viscosity transport equation, $c_{b1} \bar{S} \bar{\nu}$, is multiplied by a rotation function f_{r1} , defined as follows:

$$f_{r1}(r^*, \bar{r}) = (1 + c_{r1}) \frac{2r^*}{1 + r^*} [1 - c_{r3} \tan^{-1}(c_{r2} \bar{r})] - c_{r1} \quad (2.6.21)$$

Assuming that all of the variables and their derivatives are defined with respect to the reference frame of the calculation, which is rotating at a rate Ω , the non dimensional quantities r^* and \bar{r} are given by the following formulas:

$$r^* = S/\omega, \quad \bar{r} = 2\omega_{ik} S_{jk} \left[\frac{DS_{ij}}{Dt} + (\epsilon_{imn} S_{jn} + \epsilon_{jmn} S_{in}) \Omega_m \right] / D^4 \quad (2.6.22)$$

Here, $S_{ij} = 0.5 \left(\frac{\partial u_i}{\partial x_j} + \frac{\partial u_j}{\partial x_i} \right)$, $\omega_{ij} = 0.5 \left[\left(\frac{\partial u_i}{\partial x_j} - \frac{\partial u_j}{\partial x_i} \right) + 2\epsilon_{mji} \Omega_m \right]$

$$S^2 = 2S_{ij}S_{ij}, \quad \omega^2 = 2\omega_{ij}\omega_{ij}, \quad D^2 = 0.5(S^2 + \omega^2)$$

and $\frac{DS_{ij}}{Dt}$ are the components of the Lagrangian derivative of the strain tensor. These are all second derivatives. The Einstein summation convention is used with the model constants $c_{r1} = 1.0, c_{r2} = 12.0, c_{r3} = 1.0$, respectively.

In the present study, there is no rotation effect, i.e. $\Omega = 0.0$, so the curvature factor also gets simplified. It has also been observed that the implementation

of the curvature term leads to a slow convergence rate without having any appreciable change in the solution, so the curvature terms have been no more considered in the rest of the computations.

2.6.0.1 Advantages and Disadvantages of Spalart-Allmaras Model

Some of the advantages of Spalart-Allmars model are:

1. It is applicable to free shear flows and also to viscous flows past solid bodies with laminar regions.
2. It is more accurate in attached flows and wakes, including merging boundary layers and wakes.
3. It is also very much useful for computations in unstructured grid.
4. In calculation of eddy viscosity, the upstream value are taken into account which improves the solution.

Some disadvantages are:

1. It is not a simple model for implementation, because it involves an extra differential equations and takes large computational time.
2. It can only predict the velocity profiles \bar{u} and \bar{v} and the turbulent shear $(-\overline{u'v'})$ but cannot give the turbulent energy or any of the components $(u', v', w')_{rms}$.

Chapter 3

Numerical Technique and Procedure

The 2-D flow simulations over multi-element airfoil are carried out using incompressible Navier-Stokes equations solver, by stabilized finite element method. The finite element method starts with a piecewise approximation to the dependent variables. Various methods of this class exist, all requiring an integral representation of the partial differential equation to be constructed. The classical finite element method for structural mechanics are based on variational principles. But for many engineering problems, particularly in fluid flow, more general approaches, such as the method of weighted residuals are used. The primary advantage of FEM is its ability to handle a complex geometry. The major activities involved in finite element analysis broadly classified into three classes:

1. Pre-processing
2. Processing
3. Post-processing

Pre-processing refers to all the tasks to be performed before starting the flow solution using N-S solver. The major pre-processing activities are smoothing the airfoil, generating the mesh and applying the required boundary conditions. The other important activity is to automate the grid generation procedure so that different grids can be generated for different configurations like airfoil and parafoil at different angles of attack.

Smoothing the Airfoil: The airfoil geometry which we obtained with contains very few points. These many points are not sufficient to generate a fine mesh which can resolve the flow field properly. So, to increase the number of points on the airfoil surface, we used a NAG routine E02BAF and E02BBF which fits cubic splines.

Mesh generation: This is one of the very important task in CFD because with a poor mesh one can never expect good results even with higher order accurate method. The mesh generation described in the present study, follows Vinod's work [28]. Mesh is basically set of points, with certain connectivity which one obtains by discretizing the domain of flow. Because of this spatial discretization the continuum of space is replaced by a finite number of points where numerical value of variables has to be determined. For the simulations the space domain has been discretized using hybrid grid i.e. the region close to the body consists of structured mesh while the rest is filled with unstructured mesh. Unstructured meshes are very useful for the complex geometries at the same time they take into account the complexity of the flow. Structured meshes have logical indexing scheme for the nodes while, the unstructured meshes have a irregular connectivity. In the structured mesh generation the points are distributed in any ratio uniform or geometric progression or exponentially varying. In our cases, structured meshes are constructed using lines normal to the surface of the body. Triangular elements have been considered which are supposed to be ideal for the complex geometries. Filling up the whole domain with structured mesh would be very costly and controlling the density of points would be difficult. So to capture the shear layer coming out of slat we generated a structured mesh just ahead the slat. Further refinement is done by two level refinement of the main element mesh. Here the 2nd level of refinement is adjusted according to slat shear layer. Over the flap we inserted a inclined fictitious boundary following the flap deflection.

For the unstructured mesh generation, among various algorithms available for triangulation, Delaunay approach has proved to be very efficient. The most important property of a Delaunay mesh is that for each element in the mesh, its circumcircle which encompasses all nodes defining that element contains no other nodes of the mesh. This produces elements with very optimal aspect ratio. The algorithm that we have used in our mesh generation is an incremental insertion algorithm given by Watson. A brief outline of it is stated below :

- insert new site Q into existing Delaunay triangulation.
- find any triangle with circumcircle containing site Q .
- perform a search to find remaining set of triangles with circumcircle containing site Q .
- construct list of edges associated with deletable triangles. Delete all edges from the list that appear more than once.
- Connect remaining edges to site Q and update Delaunay data structure.

After obtaining an initial mesh the elements lying in the holes and convex regions are being removed. Finally, based on height functions (based on spacing of the points of the perimeter) we insert more elements, where desired, to refine the mesh.

An automatic unstructured mesh generator uses some sort of boundary data alone as an input, and then create the interior nodes and elements automatically based on the boundary data. As the mesh generator makes little or no assumption on the structure of the domain any structure can be modeled.

The basic data structure of the mesh consists of X-array and IEN-array. The X-array i.e. $x(nsd, numnp)$ which stores the x and y coordinates of the nodal points. Here, nsd stands for number of space dimension. It is equal to 2 for our case. $numnp$ is the global node number.

IEN-array, i.e. $ien(nen, numel)$ which defines the connectivity between the global nodal points and it contains the information of element numbering with respect to local and global node numbering. Here, nen stands for local node numbers, 3 for triangular elements and 4 for quadrilateral elements. $numel$ is the global element number.

3.1 Mesh Design

Mesh design for flow computation is the most important issue, it must take into account the nature of flow. For example, the flow near the body involves boundary layer development, boundary layer separation, formation of shear layer, interaction of shear layers,

sharp velocity gradients etc., whereas far away from the body upstream and downstream flow changes are small. Around the body we generate structured mesh which is obtained by drawing lines perpendicular to the slope of the airfoil surface. This feature is also essential from the point of view of turbulence modeling. As boundary layer velocity profile does not vary linearly, a provision has been made to vary the spacing between different layers of the structured mesh in geometric progression. To capture the wake a fictitious boundary has been inserted so that the concentration of elements increase in the zone near the airfoil.

Automatic mesh generator description: The grid generator routine needs various parameters like the points on the surface of the airfoil, the points on the outer domain, the points on a fictitious boundary if present, the first element thickness for the structured mesh, the number of elements on the structured mesh and the total thickness of structured mesh. For the mesh around multi-element airfoil we need to supply these inputs for each element.

To obtain meshes at certain angle of attack with the free stream velocity, the nodes are rotated about certain point, i.e. input parameter. The new coordinates are being obtained using the following simple equations.

$$x' = x \cos \phi - y \sin \phi, \quad y' = x \sin \phi + y \cos \phi \quad (3.1.1)$$

The mesh generator uses a mesh moving technique such that mesh can be obtained on an airfoil at different angles of attack restoring the number of elements and the number of nodes.

3.2 Governing Equations

Let $\Omega \subset R^{n_{sd}}$ and $(0, T)$ be the spatial and temporal domains respectively, where n_{sd} is the number of space dimensions, and Γ denote the boundary Ω . The spatial and temporal coordinates are denoted by \mathbf{x} and t . The Navier-Stokes equations governing incompressible fluid flow are

$$\rho \left(\frac{\partial \mathbf{u}}{\partial t} + \mathbf{u} \cdot \nabla \mathbf{u} - \mathbf{f} \right) - \nabla \cdot \boldsymbol{\sigma} = 0 \quad \text{on } \Omega \text{ for } (0, T) \quad (3.2.2)$$

$$\nabla \cdot \mathbf{u} = 0 \quad \text{on } \Omega \text{ for } (0, T) \quad (3.2.3)$$

Here, ρ , \mathbf{u} , \mathbf{f} and $\boldsymbol{\sigma}$ are the density, velocity, body force and the stress tensor, respectively. The stress tensor is written as the sum of its isotropic and deviatoric parts :

$$\boldsymbol{\sigma} = -p\mathbf{I} + \mathbf{T} , \quad \mathbf{T} = 2\mu\boldsymbol{\epsilon}(\mathbf{u}) , \quad \boldsymbol{\epsilon}(\mathbf{u}) = \frac{1}{2}((\nabla\mathbf{u}) + (\nabla\mathbf{u})^T) \quad (3.2.4)$$

where p and μ are the pressure and coefficient of dynamic viscosity, respectively. Both the Dirichlet and Neumann type boundary conditions are accounted for, represented as

$$\mathbf{u} = \mathbf{g} \text{ on } \Gamma_g , \quad \mathbf{n} \cdot \boldsymbol{\sigma} = \mathbf{h} \text{ on } \Gamma_h \quad (3.2.5)$$

where, Γ_g and Γ_h are complementary subsets of the boundary Γ . The initial condition on the velocity is specified on Ω :

$$\mathbf{u}(\mathbf{x}, 0) = \mathbf{u}_0 \text{ on } \Omega \quad (3.2.6)$$

where, \mathbf{u}_0 is divergence free. The Spalart-Allmaras (one equation turbulence model) for eddy viscosity is

$$\begin{aligned} \frac{\partial \bar{\nu}}{\partial t} + \mathbf{u} \cdot \nabla \bar{\nu} - c_{b1} [1 - f_{t2}] \bar{S} \bar{\nu} - \frac{1}{\sigma'} [\nabla \cdot ((\nu + \bar{\nu}) \nabla \bar{\nu}) + c_{b2} (\nabla \bar{\nu})^2] \\ + \left[c_{w1} f_w - \frac{c_{b1}}{\kappa^2} f_{t2} \right] \left[\frac{\bar{\nu}}{d} \right]^2 - f_{t1} \Delta U^2 = 0 \quad \text{on } \Omega \text{ for } (0, T) \end{aligned} \quad (3.2.7)$$

Here, ν is the molecular viscosity and $\bar{\nu}$ obeys the above transport equation. So, the eddy viscosity (ν_t) is defined as $\nu_t = \bar{\nu} f_{v1}$ where $f_{v1} = \frac{\chi^3}{\chi^3 + c_{v1}^3}$, $\chi \equiv \frac{\bar{\nu}}{\nu}$, $\bar{S} = S + \frac{\bar{\nu}}{\kappa^2 d^2 f_{v2}}$, $f_{v2} = 1 - \frac{\chi}{1 + \chi f_{v1}}$ where S is the magnitude of the vorticity, and d is the distance to the closest wall. The function $f_w = g \left[\frac{1 + c_{w3}^6}{g^6 + c_{w3}^6} \right]^{\frac{1}{6}}$, $g = r + c_{w2} (r^6 - r)$, $r \equiv \frac{\bar{\nu}}{S \kappa^2 d^2}$. The f_{t2} function is given by $f_{t2} = c_{t3} \exp(-c_{t4} \chi^2)$ and the trip function f_{t1} is as follows : $f_{t1} = c_{t1} g_t \exp(-c_{t2} \frac{\omega_t^2}{\Delta U^2} [d^2 + g_t^2 d_t^2])$ where d_t is the distance from the field point to the trip, which is on the wall, ω_t is the wall vorticity at the trip, and ΔU is the difference between the velocity at the field point and that at the trip. Then $g_t \equiv \min(0.1, \frac{\Delta U}{\omega_t} \Delta x_t)$ where Δx_t is the grid spacing along the wall at the trip, whereas the others parameters are defined as $c_{b1} = 0.1355$, $\sigma' = \frac{2}{3}$, $c_{b2} = 0.622$, $\kappa = 0.41$, $c_{w1} = \frac{c_{b1}}{\kappa^2} + \frac{(1 + c_{b2})}{\sigma'}$, $c_{w2} = 0.3$, $c_{w3} = 2$, $c_{v1} = 7.1$, $c_{t1} = 1$, $c_{t2} = 2$, $c_{t3} = 1.2$ and $c_{t4} = 0.5$. Both the Dirichlet and Neumann type boundary conditions are accounted for, represented

as

$$\bar{\nu} = g_1 \text{ on } \Gamma_g, \quad n \cdot \bar{\nu} = h_1 \text{ on } \Gamma_h \quad (3.2.8)$$

where, Γ_g and Γ_h are complementary subsets of the boundary Γ . The initial condition on the eddy viscosity is specified on Ω :

$$\bar{\nu}(\mathbf{x}, 0) = \bar{\nu}_0 \text{ on } \Omega \quad (3.2.9)$$

where, $\bar{\nu}_0$ is divergence free.

3.3 Finite Element Formulation

Consider a finite element discretization of Ω into sub domains $\Omega^e, e = 1, 2, \dots, n_{el}$, where n_{el} is the number of elements. Based on this discretization, for velocity, pressure and eddy viscosity we define the finite element trial function spaces \mathcal{S}_u^h , \mathcal{S}_p^h and $\mathcal{S}_{\bar{\nu}^h}$, and weighting function spaces \mathcal{V}_u^h , \mathcal{V}_p^h and $\mathcal{V}_{\bar{\nu}^h}$. These function spaces are selected, by taking the Dirichlet boundary conditions into account, as subsets of $[\mathbf{H}^{1h}(\Omega)]^{n_{sd}}$ and $\mathbf{H}^{1h}(\Omega)$, where $\mathbf{H}^{1h}(\Omega)$ is the finite dimensional function space over Ω . The stabilized finite element formulation of equation 3.2.2 and equation 3.2.3 is written as follows: find $\mathbf{u}^h \in \mathcal{S}_u^h$ and $p^h \in \mathcal{S}_p^h$ such that $\forall \mathbf{w}^h \in \mathcal{V}_u^h, q^h \in \mathcal{V}_p^h$

$$\begin{aligned} \int_{\Omega} \mathbf{w}^h \cdot \rho \left(\frac{\partial \mathbf{u}^h}{\partial t} + \mathbf{u}^h \cdot \nabla \mathbf{u}^h - \mathbf{f} \right) d\Omega + \int_{\Omega} \epsilon(\mathbf{w}^h) : \sigma(p^h, \mathbf{u}^h) d\Omega + \int_{\Omega} q^h \nabla \cdot \mathbf{u}^h d\Omega \\ + \sum_{e=1}^{n_{el}} \int_{\Omega^e} \frac{1}{\rho} \left(\tau_{SUPG} \rho \mathbf{u}^h \cdot \nabla \mathbf{w}^h + \tau_{PSPG} \nabla q^h \right) \cdot \\ \left[\rho \left(\frac{\partial \mathbf{u}^h}{\partial t} + \mathbf{u}^h \cdot \nabla \mathbf{u}^h - \mathbf{f} \right) - \nabla \cdot \sigma(p^h, \mathbf{u}^h) \right] d\Omega^e \\ + \sum_{e=1}^{n_{el}} \int_{\Omega^e} \delta \nabla \cdot \mathbf{w}^h \rho \nabla \cdot \mathbf{u}^h d\Omega^e = \int_{\Gamma_h} \mathbf{w}^h \cdot \mathbf{h}^h d\Gamma \quad (3.3.10) \end{aligned}$$

The equation 3.2.7 is written as follows: find $\bar{\nu}^h \in \mathcal{S}_{\bar{\nu}^h}$ such that $\forall \mathbf{w}^h \in \mathcal{V}_{\bar{\nu}^h}$ and

$$\begin{aligned}
F = & c_{b1} [1 - f_{t2}] \bar{S} \bar{v}^h - c_{b2} (\nabla \bar{v}^h)^2 + [c_{w1} f_w - \frac{c_{b1}}{\kappa^2} f_{t2}] [\frac{\bar{v}^h}{d}]^2 - f_{t1} \Delta U^2 \\
& \int_{\Omega} \mathbf{w}^h \cdot \left(\frac{\partial \bar{v}^h}{\partial t} + \mathbf{u}^h \cdot \nabla \bar{v}^h - F \right) d\Omega + \int_{\Omega} \frac{1}{\sigma'} [\nabla \mathbf{w}^h \cdot ((\nu + \bar{v}^h) \nabla \bar{v}^h)] d\Omega \\
& + \sum_{e=1}^{n_{el}} \int_{\Omega^e} (\tau_{SUPG} \mathbf{u}^h \cdot \nabla \mathbf{w}^h) \cdot \left[\frac{\partial \bar{v}^h}{\partial t} + \mathbf{u}^h \cdot \nabla \bar{v}^h - F \right] d\Omega^e = \int_{\Gamma_h} \mathbf{w}^h \cdot h_1^h d\Gamma \quad (3.3.11)
\end{aligned}$$

In the variational formulation, the first three terms of equation 3.3.10, the first two terms of equation 3.3.11 and the right hand side of both equations constitute the Galerkin formulation of the problem. The first series of element level integrals are the SUPG and PSPG stabilization terms added to the variational formulations. In the current formulation τ_{PSPG} is the same as τ_{SUPG} and is given as

$$\tau = ((\frac{2\|\mathbf{u}^h\|}{h})^2 + (\frac{12\nu}{h^2})^2)^{-\frac{1}{2}} \quad (3.3.12)$$

The second series of element level integrals are added to the formulation for numerical stability at high Reynolds numbers. This is a least squares terms based on the continuity equation. The coefficient δ is defined as

$$\delta = \frac{h}{2} \|\mathbf{u}^h\|_z \quad (3.3.13)$$

where,

$$z = \begin{cases} (\frac{Re_u}{3}) & Re_u \leq 3 \\ 1 & Re_u > 3 \end{cases} \quad (3.3.14)$$

and Re_u is the cell Reynolds number. Both stabilization terms are weighted residuals, and therefore maintain the consistency of the formulation. h is the *element length* and various definitions of h is available. The one which results in the least sensitivity of the computed flow to the element aspect ratio has been used for computations in the present work. According to this definition, the element length is equal to the minimum edge length of a triangular (3 noded) element.

The time discretization of variational formulations given by the equations 3.3.10 & 3.3.11 is done via the generalized trapezoidal rule (Crank-Nicholson). For unsteady computations, we employ a second order accurate in time procedure. Equal in order basis functions for velocity and pressure (the P1P1 element) are used and a 3 point quadrature is employed for numerical integration. The non-linear equation systems resulting from

the finite element discretization of the flow equations are solved using the Generalized Minimal RESidual (GMRES) technique. The pre-conditioning used in conjunction with the GMRES method is nodal block diagonal. Matrix free GMRES algorithm is used which reduces the memory requirements. The key advantage of the matrix free GMRES algorithm is direct computation of the result of matrix vector products in the GMRES algorithm which avoids the explicit formation of the element level matrices.

Chapter 4

Results and Discussions

This chapter presents the results of 2-D simulations of turbulent flows using Spalart-Allmaras turbulence model on three geometries of increasing complexity. Initially the calculations have been done for flat plate, then NACA 0012 airfoil and finally for McDonnell Douglas 30P-30N multi-element airfoil. The incompressible Reynolds Averaged Navier Stokes equations, in conjunction with the Spalart-Allmaras turbulence model for turbulence closure, have been solved using stabilized finite element formulations. To stabilize the computations against spurious numerical oscillations in advection dominated flows and to enable the use of equal order interpolation velocity-pressure elements, streamline-upwind/Petrov-Galerkin(SUPG) and pressure-stabilizing/Petrov-Galerkin(PSPG) stabilization techniques have also been employed. In this technique, stabilizing terms are added to the basic Galerkin formulation(Chapter 3). Equal-in-order linear basis functions for velocity and pressure have been used and a 3 point quadrature has been employed for numerical integration. The time integration of the equations has been carried out via the time accurate version of the generalized trapezoidal rule(Crank-Nicholson). The nonlinear implicit equation system resulting from the finite element discretization of the flow equations has been solved using the Generalized Minimal RESidual (GMRES) technique in conjunction with diagonal preconditioners.

The finite element meshes used in various computations consist of a structured mesh close to the body and an unstructured mesh generated via Delaunay's triangulation, in the rest of the domain. This type of grid has the ability of handling fairly complex geometries while still providing the desired resolution close to the body to effectively

capture the boundary layer and shear layer, especially in the context of unsteady flows. In addition, the unstructured grid around the body allows for efficient implementation of the turbulence model.

The non-dimensional quantities encountered in discussing the results are :

- Pressure coefficient.

$$C_p = \frac{(p - p_\infty)}{\frac{1}{2}\rho_\infty \|u_\infty\|^2}$$

- Drag coefficient.

$$C_d = \frac{D}{\frac{1}{2}\rho_\infty \|u_\infty\|^2 A}$$

- Lift coefficient.

$$C_l = \frac{L}{\frac{1}{2}\rho_\infty \|u_\infty\|^2 A}$$

- Moment coefficient.

$$C_m = \frac{M}{\frac{1}{2}\rho_\infty \|u_\infty\|^2 Al}$$

where, A is the reference area, l is the reference length, D is the drag force, L is the lift force and M is the pitching moment.

4.1 Flat Plate

4.1.1 Computational Domain & Boundary conditions

The flat plate resides in a rectangular computational domain of dimension 15×5 units. The inflow boundary is located at a distance of 5 unit from the leading edge of the plate as shown in Figure 4.1. On the plate surface, the no-slip condition for the velocity and zero value for eddy viscosity have been specified while free stream values have been assigned for the velocity at the inflow boundary, whereas a very low value of eddy viscosity ($\bar{\nu} = 10^{-10}$) has been specified at the same boundary. At the downstream boundary, a Neumann type boundary condition for both velocity and eddy viscosity

has been specified. The Reynolds number is calculated based on unit length of plate, free-stream speed and viscosity of the fluid.

4.1.2 Turbulent calculation for different values of Re

Results have been presented in this section for different values of Re using two different Meshes(one coarse & one fine), as shown in Table 4.1.

Re	Mesh1		Mesh2	
	nodes	elements	nodes	elements
10^5	5151	5000	15251	15000
10^6	5151	5000	15251	15000

Table 4.1: Number of nodes and elements in different meshes used for turbulent calculation of flow past a flat plate.

The turbulent computations have been carried out in two-dimensions by specifying the transition location on the plate surface for $Re = 10^5$ & 10^6 . The variation of *skin-friction coefficient*(C_f), *turbulence index*(i_t) along the length of the plate have been shown. The computed results have also been compared with the theoretical values of (C_f), calculated from correlation function given by F. M. White [38], defined as:

$$C_f = \begin{cases} \text{laminar} & = \frac{0.664}{\sqrt{Re_x}} \\ \text{turbulent} & = \frac{0.455}{\ln^2(0.06Re_x)} \end{cases} \quad (4.1.1)$$

where x is the distance along the length of the plate.

Figure 4.2 & Figure 4.3 shows the variation of C_f along the length of the plate for $Re = 10^5$ & 10^6 , respectively. It is evident that the computed results are in good agreement with the theoretical values. Also, the desired trip location, where the flow becomes turbulent, can be controlled by specifying the trip point on the plate surface. One interesting phenomenon observed here is that, as we keep on increasing the Re , the trip location starts moving towards the leading edge. So in that case if the trip point is specified towards the trailing edge, no effect of the specified point is sensed by the flow field and it trips on its own at an upstream location. Same features have been noticed even after the spatial resolution increased to a sufficient level as used in Mesh2.

Figure 4.4 shows the case where the flow trips on its own at an upstream location due to increase of Re from 10^5 to 10^6 even after the desired trip point is specified.

Figure 4.5 shows the variation of turbulence index along the length of the plate. It is seen from the figure that at the specified trip location, the *turbulence index* achieves an approximate value of 1 and sustains this value, thereafter. In Figure 4.6, the turbulent boundary layer velocity profile is shown, which is also in good agreement with the theoretical value.

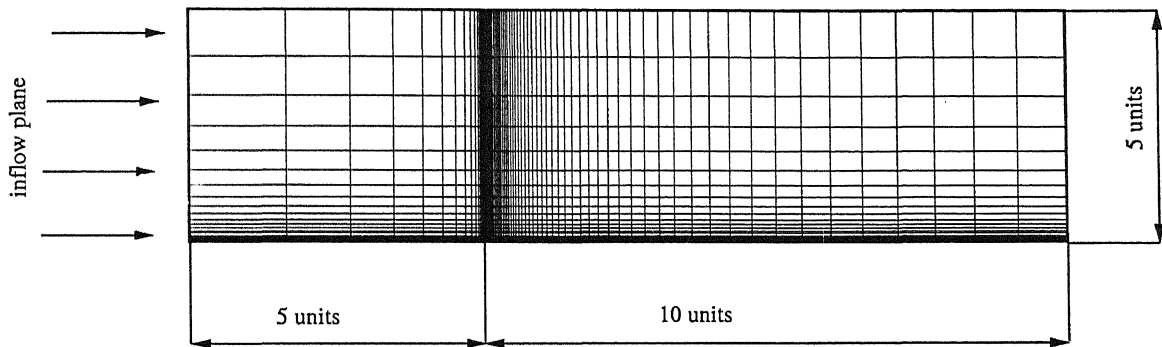


Figure 4.1: Flat plate configuration.

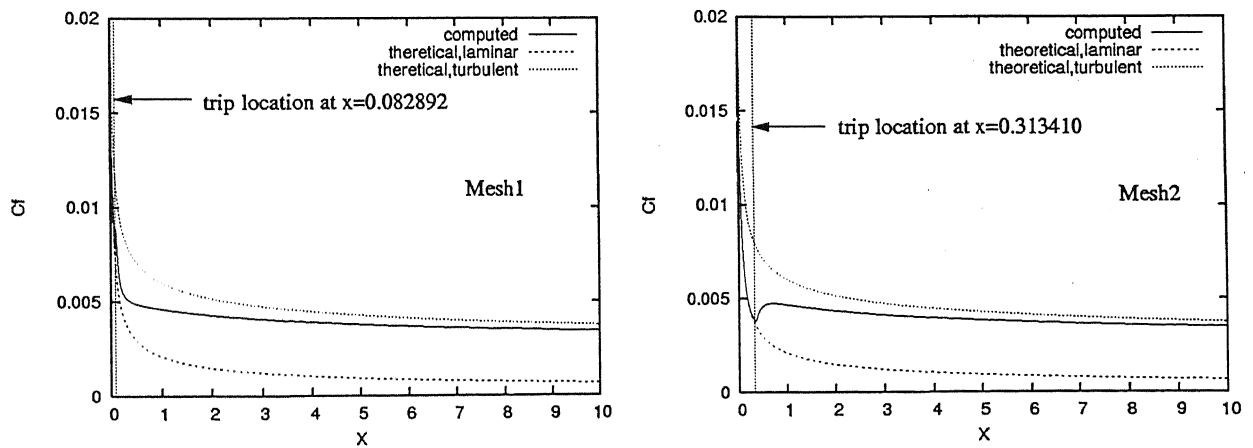


Figure 4.2: Variation of C_f along the length of the plate for $Re = 10^5$.

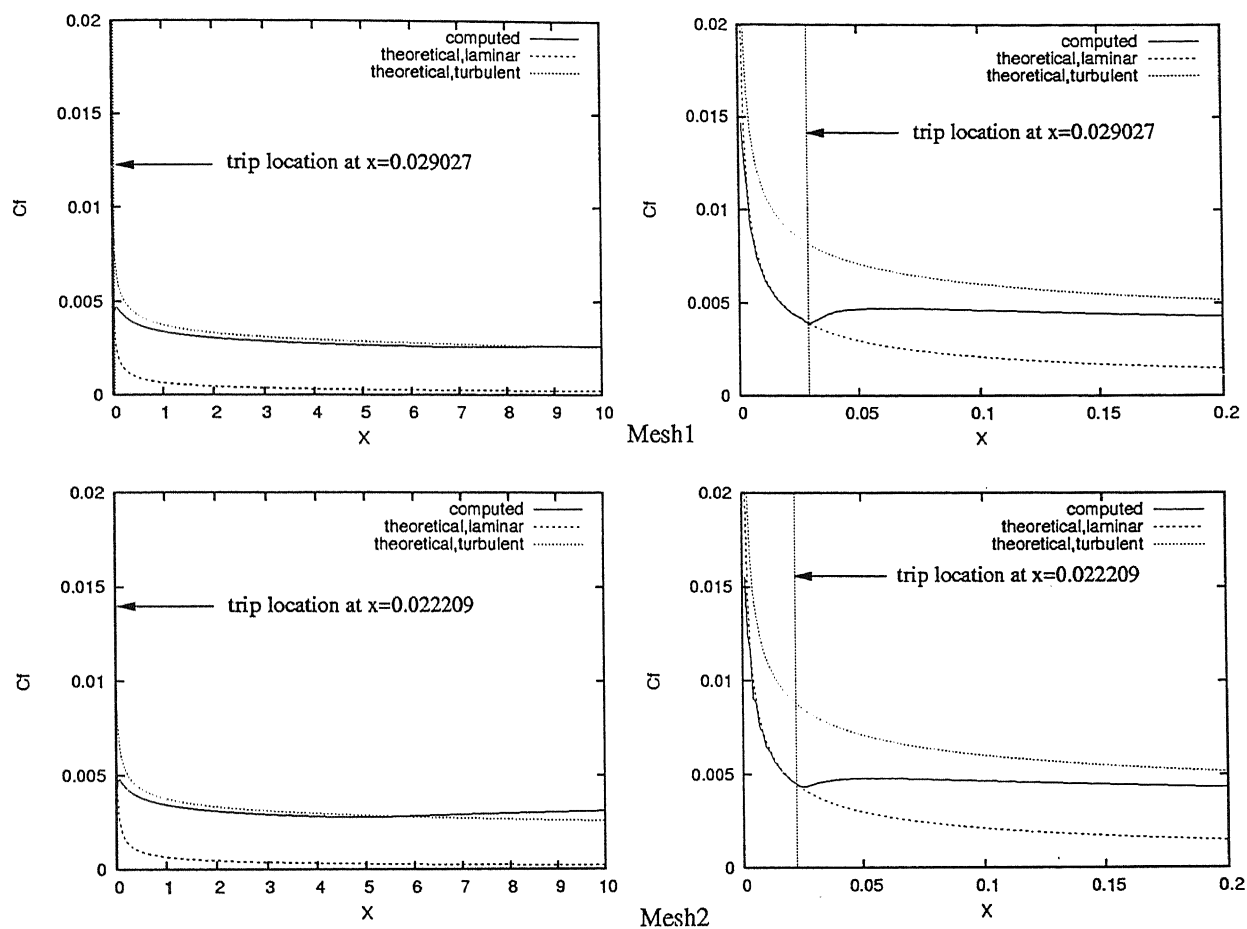


Figure 4.3: Variation of C_f along the length of the plate for $Re = 10^6$.

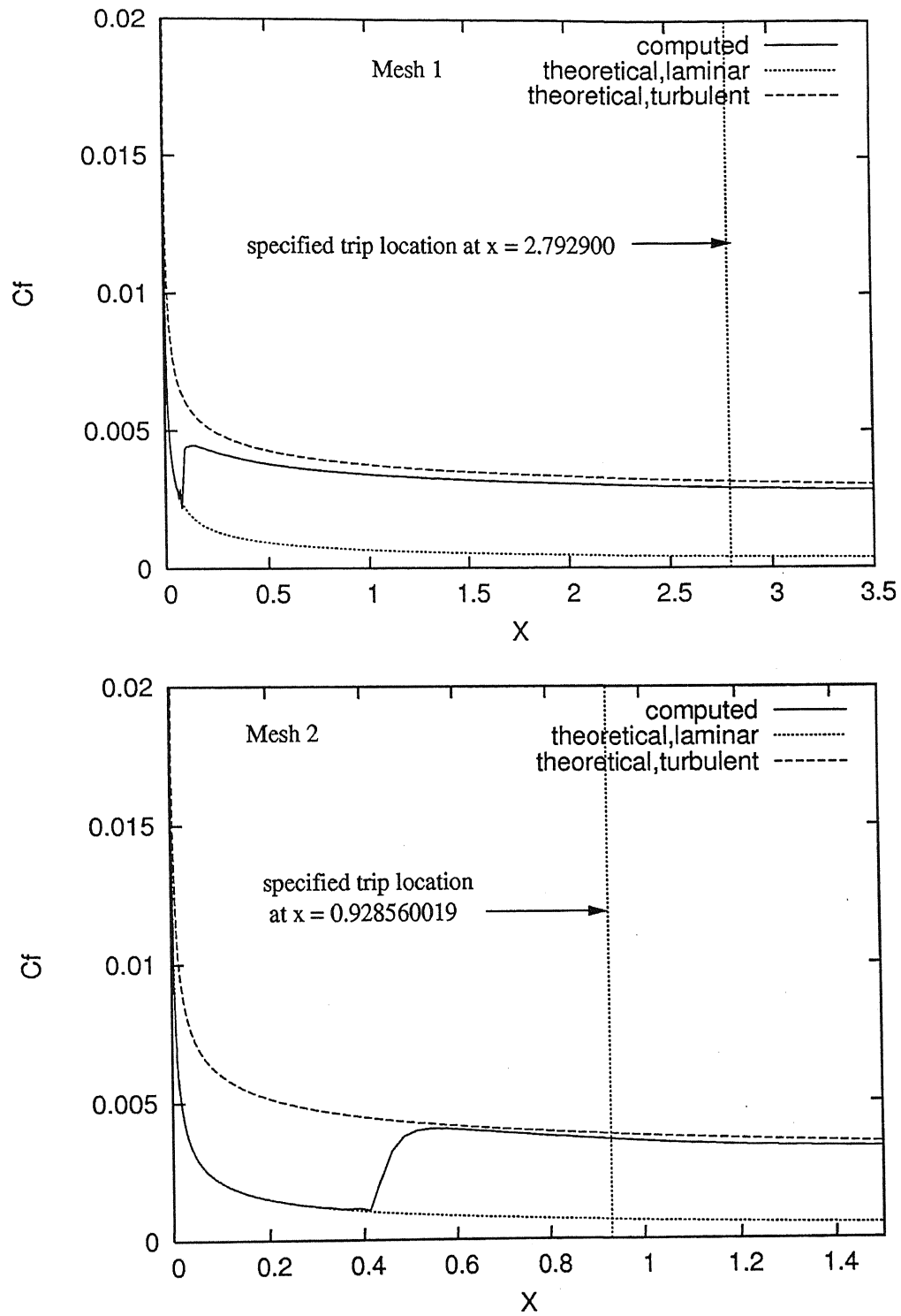


Figure 4.4: Variation of C_f (where flow trips by its own) along the length of the plate for $Re = 10^6$.

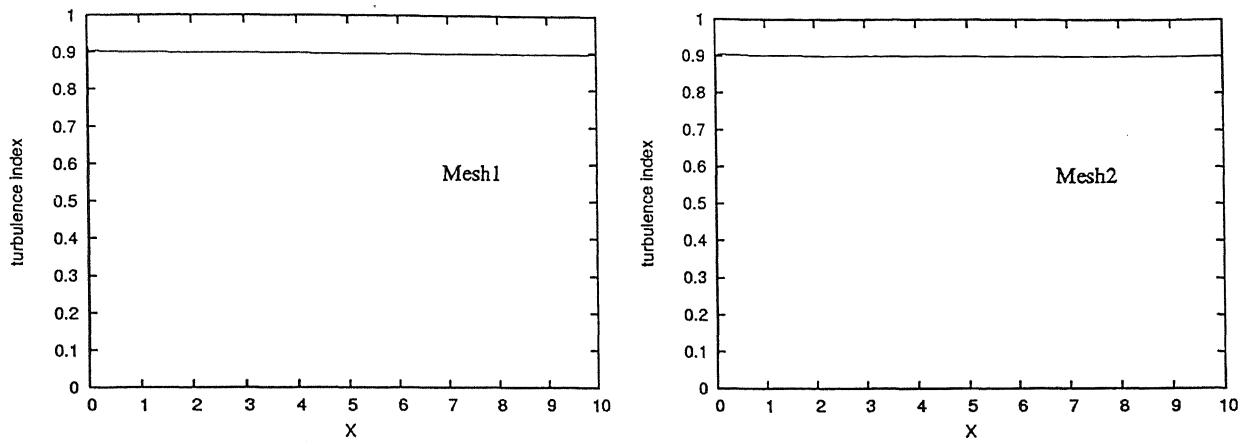


Figure 4.5: Variation of turbulence index(i_t) along the length of the plate for $Re = 10^6$.

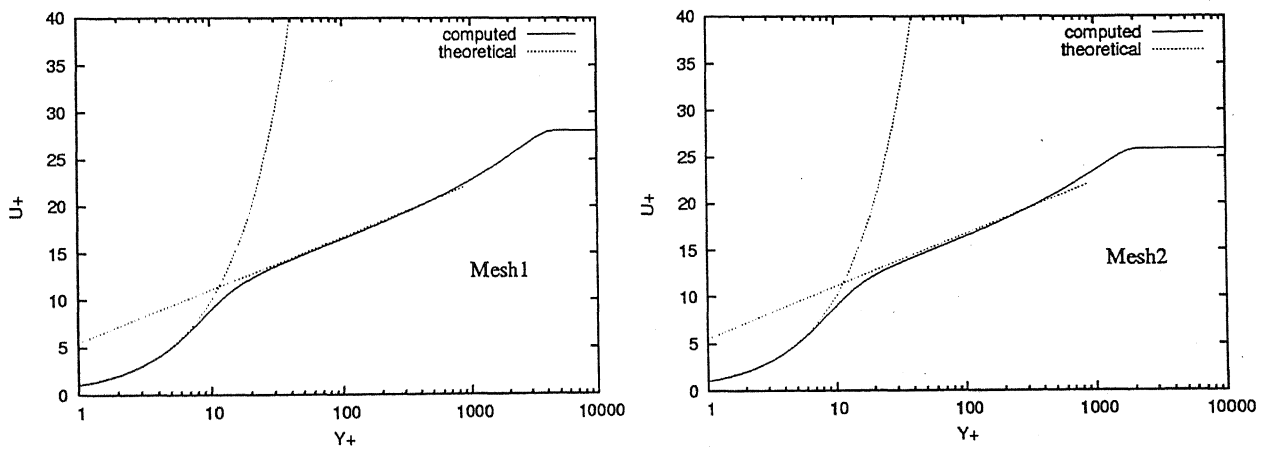


Figure 4.6: Turbulent boundary layer velocity profile over flat plate at $Re = 10^6$.

4.2 NACA 0012 airfoil

4.2.1 Computational Domain & Boundary conditions

The NACA 0012 airfoil lies in a rectangular computational domain whose upstream and downstream boundaries are located at 5 and 11 chord lengths from the leading edge, respectively. The upper and lower boundaries are placed at 5 chord lengths, each, from the leading edge. On airfoil surface, no-slip boundary condition for velocity and zero value for eddy viscosity have been specified while free-stream values have been assigned for both velocity and eddy viscosity at the upstream boundary. At the downstream boundary, a Neumann type boundary conditions for both velocity and eddy viscosity has been specified that correspond to zero viscous stress vector and zero eddy viscosity, respectively. At the upper and lower surface boundaries, the component of velocity normal to the component of stress vector along these boundaries have been prescribed zero value. The Reynolds number based on the chord length of the airfoil, free-stream velocity and viscosity of the fluid is 10^6 .

4.2.2 Finite element mesh and Results

The computed results have been reported in this section, carried out using typical finite element mesh as shown in Figure 4.7. The unstructured mesh provides flexibility to handle complex geometries. The structured mesh around the airfoil provides effective control on the grid to resolve the boundary layer. The meshes used for the turbulent calculation at different angle of attack have been listed in the Table 4.2.

α	Mesh	
	nodes	elements
5°	18925	37604
10°	18994	37742
11°	18994	37742
15°	19071	37896

Table 4.2: Number of nodes and elements in NACA mesh at different angle of attack.

The number of nodes and elements for $\alpha = 10^\circ$ & $\alpha = 11^\circ$ are same as the mesh

for $\alpha = 11^\circ$ is obtained by deforming mesh for $\alpha = 10^\circ$ using mesh-moving scheme.

The initial condition for the computation for $\alpha = 11^\circ$ is the fully developed solution for $\alpha = 10^\circ$. Figure 4.8 shows the pressure distribution over airfoil surface at different angle of attacks. Also, It shows the comparison with Baldwin-Lomax solution without any significant deviation in the result. At various angle of attacks, the velocity and eddy viscosity plots are shown in Figure 4.9. It is noticed that the flow is attached upto $\alpha = 11^\circ$ and starts separating at $\alpha = 15^\circ$ towards the trailing edge of the airfoil where the boundary layer thickness is thicker than the leading edge whereas the thickness on the lower surface is much much thinner than that on upper surface due to the difference in the pressure gradients. The variation of C_l, C_d, C_m are shown in Figure 4.10 which also represents the same phenomenon that the flows started separating at $\alpha = 15^\circ$ where the C_d value increases significantly. In Figure 4.11, the variation of turbulence index over airfoil surfaces is shown for different angle of attacks. The turbulence index variation also estimates the same flow behaviours that the flow starts separating at $\alpha = 15^\circ$. The chord wise locations for velocity profiles, shown in Figure 4.12, are listed in the Table 4.3.

Station No	x/c	surface
1	1.00	lower
2	0.240	lower
3	0.052	lower
4	0.008	upper
5	0.207	upper
6	1.00	upper

Table 4.3: NACA 0012 airfoil: Location of stations from leading edge for showing velocity profiles.

Figure 4.13, Figure 4.14 & Figure 4.15 shows the nature of the velocity profile at different stations over airfoil surfaces for various angle of attacks. The computed results have also been compared with the results, obtained using Baldwin-Lomax turbulence model. It shows that the computed results are in good agreement with Baldwin-Lomax solutions.

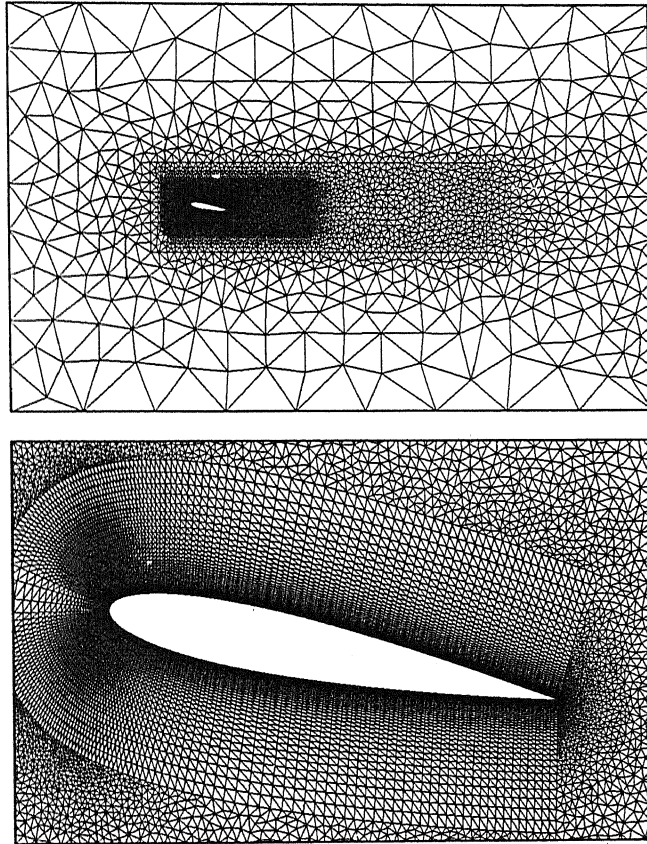


Figure 4.7: Finite element mesh for NACA 0012 airfoil at $\alpha = 10^\circ$.

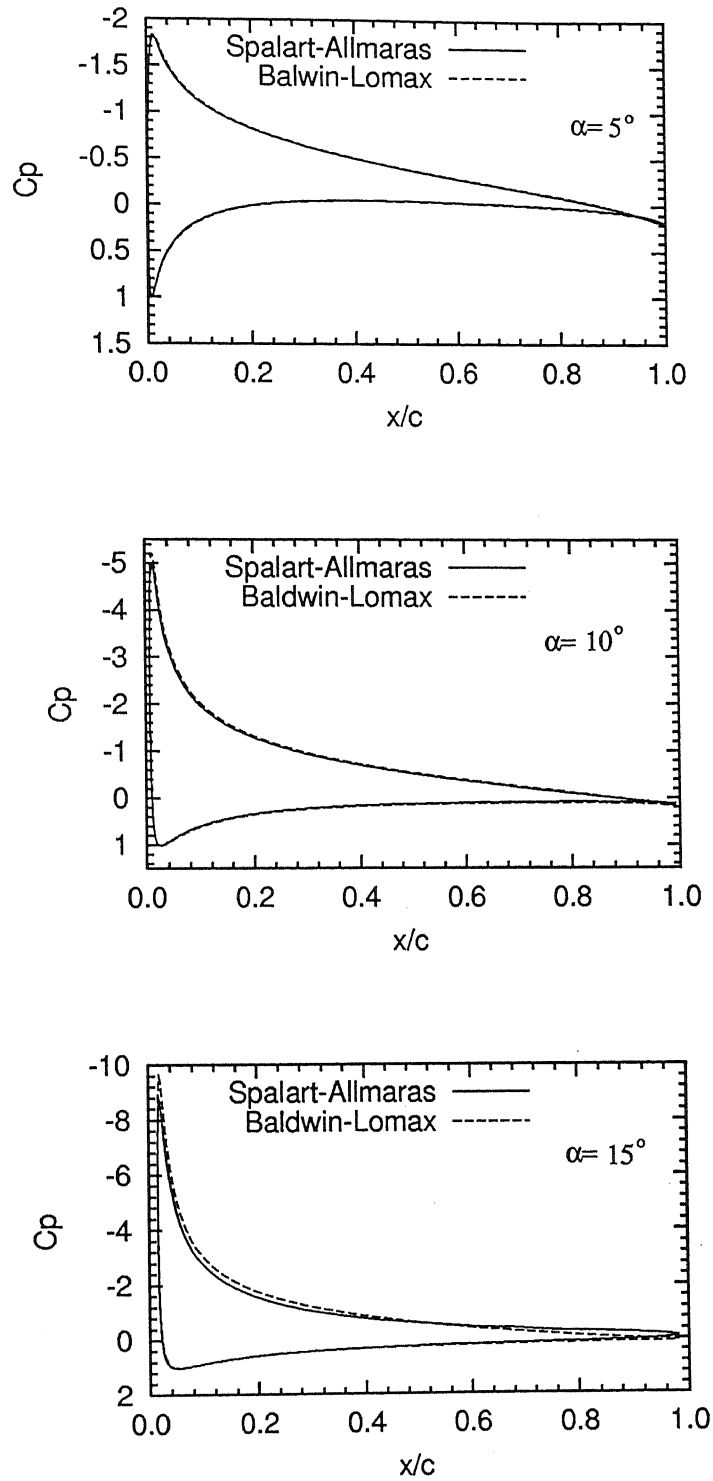


Figure 4.8: C_p distribution over NACA 0012 airfoil surface at different angle of attacks for $Re = 10^6$.

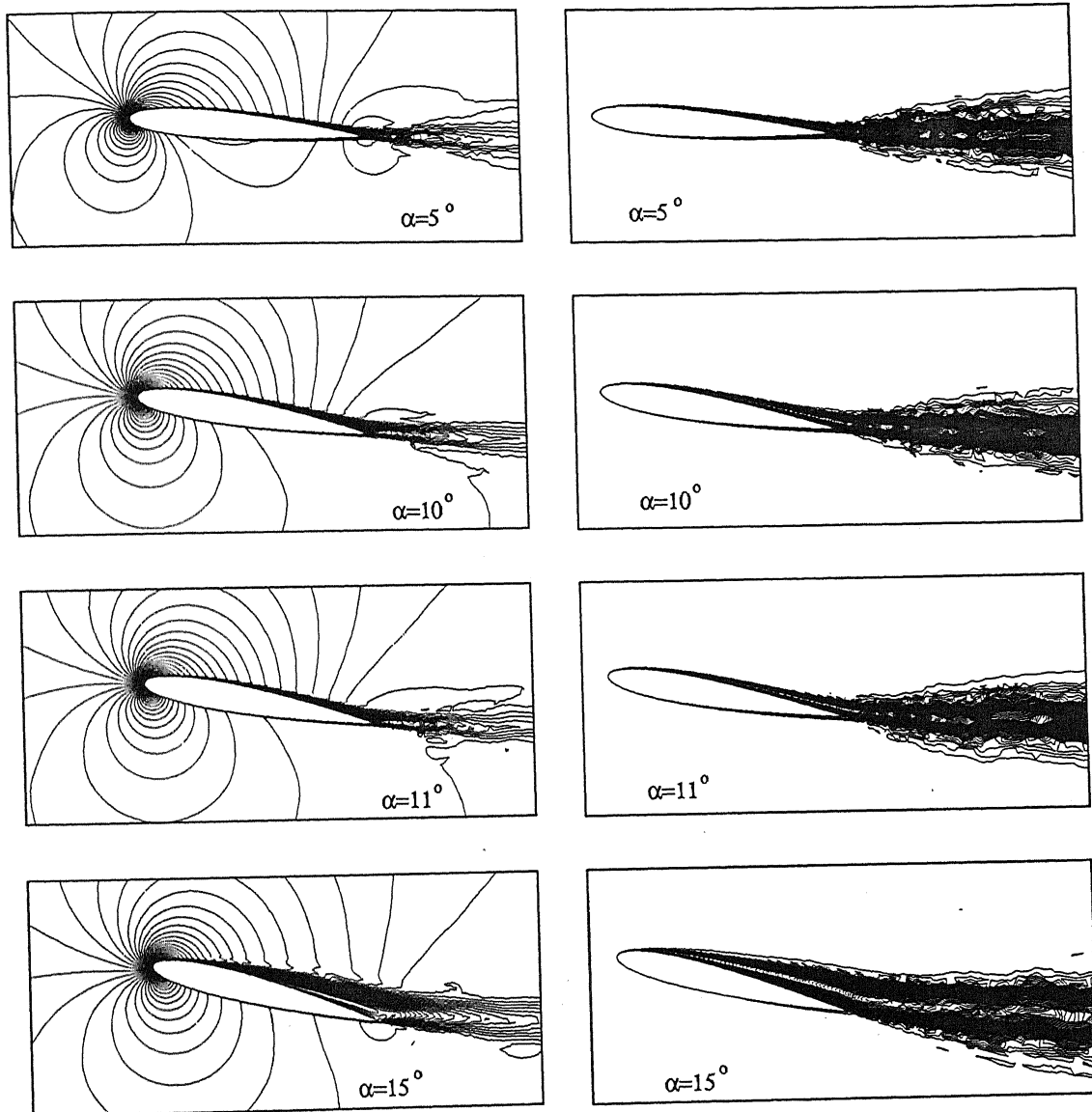


Figure 4.9: Turbulent flow past a NACA 0012 airfoil at $Re = 10^6$: magnitude of velocity(left) and eddy viscosity(right) for various angle of attacks.

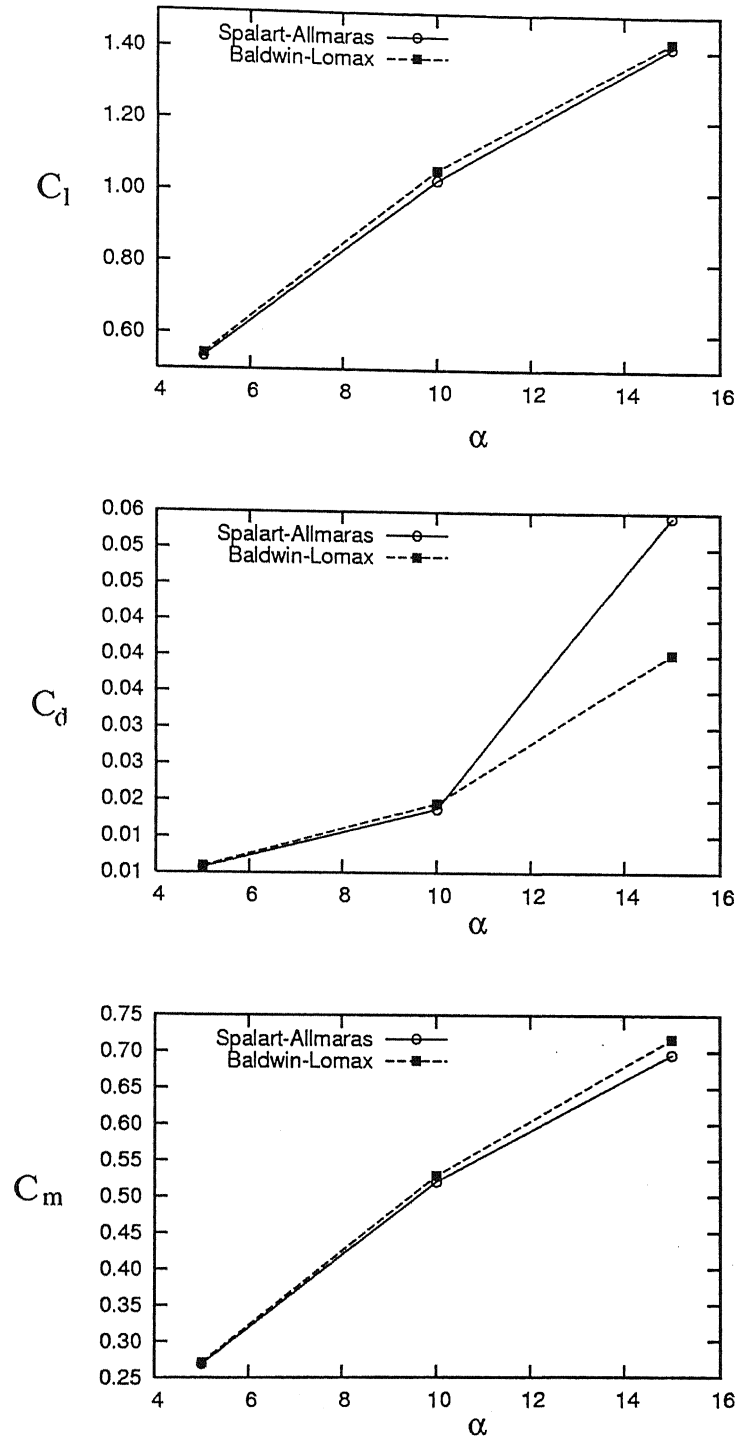


Figure 4.10: C_l, C_d, C_m versus angle of attacks for NACA 0012 airfoil at $Re = 10^6$.

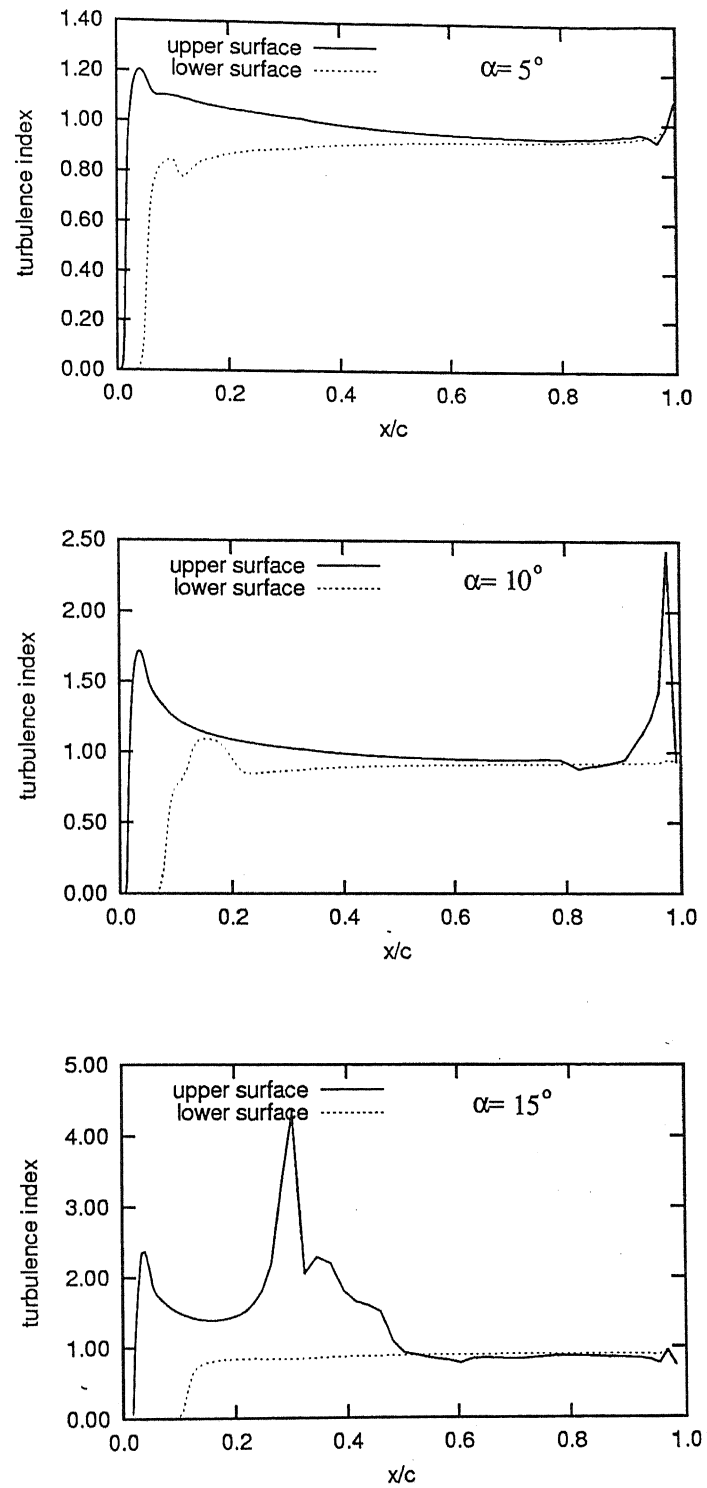


Figure 4.11: NACA 0012 airfoil: Variation of turbulence index over airfoil surface at $Re = 10^6$.

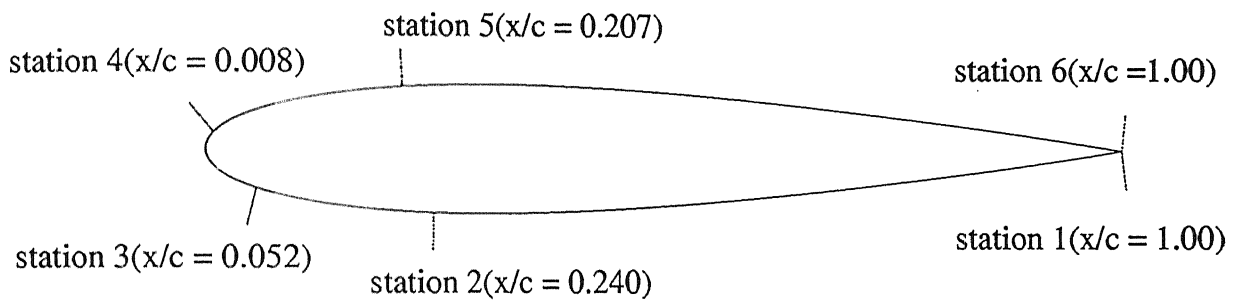


Figure 4.12: NACA 0012 airfoil: Location of stations from the leading edge where velocity profile, over airfoil surface is shown.

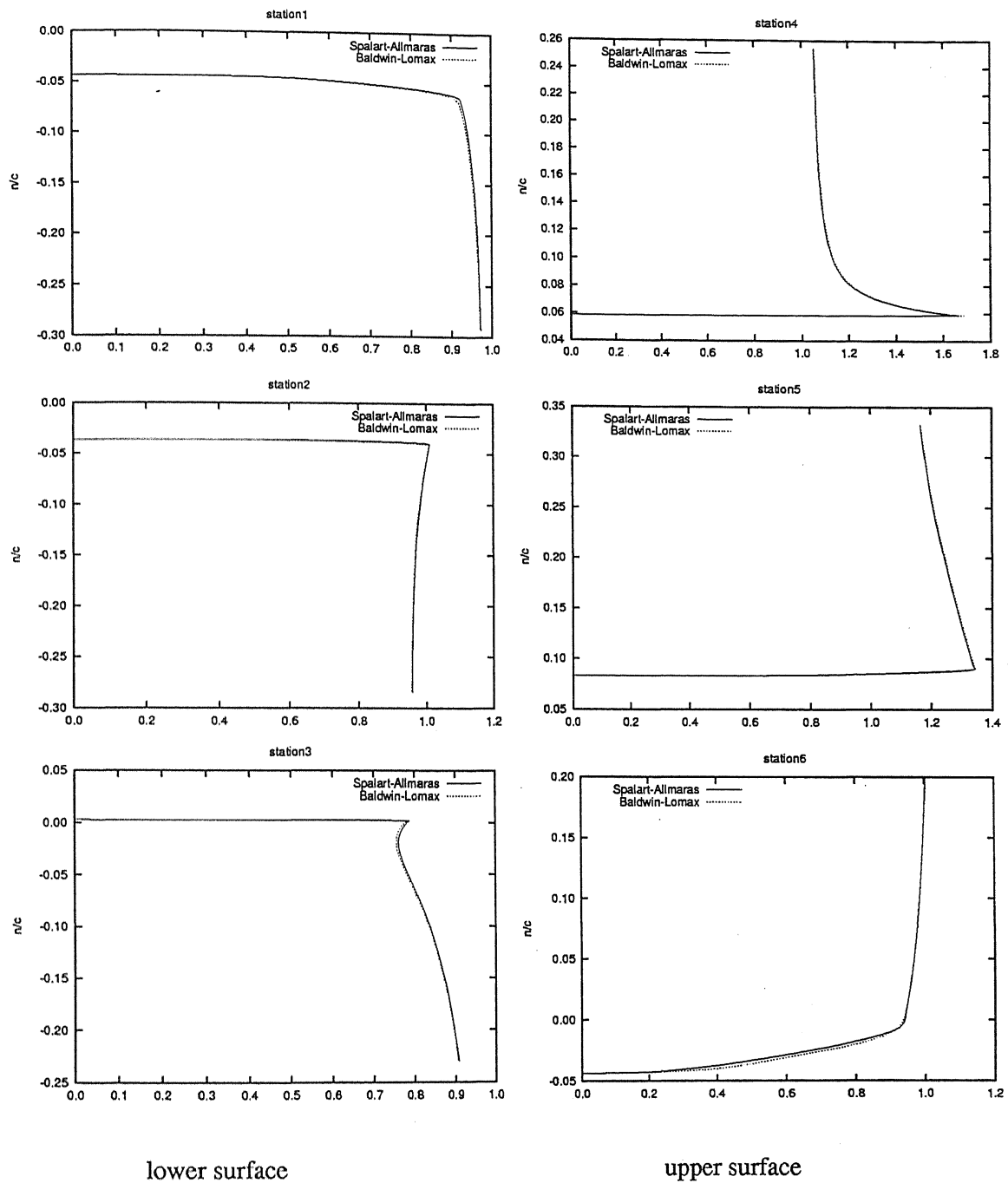


Figure 4.13: NACA 0012 airfoil: Velocity profiles at different stations over airfoil surface for $\alpha = 5^\circ$.

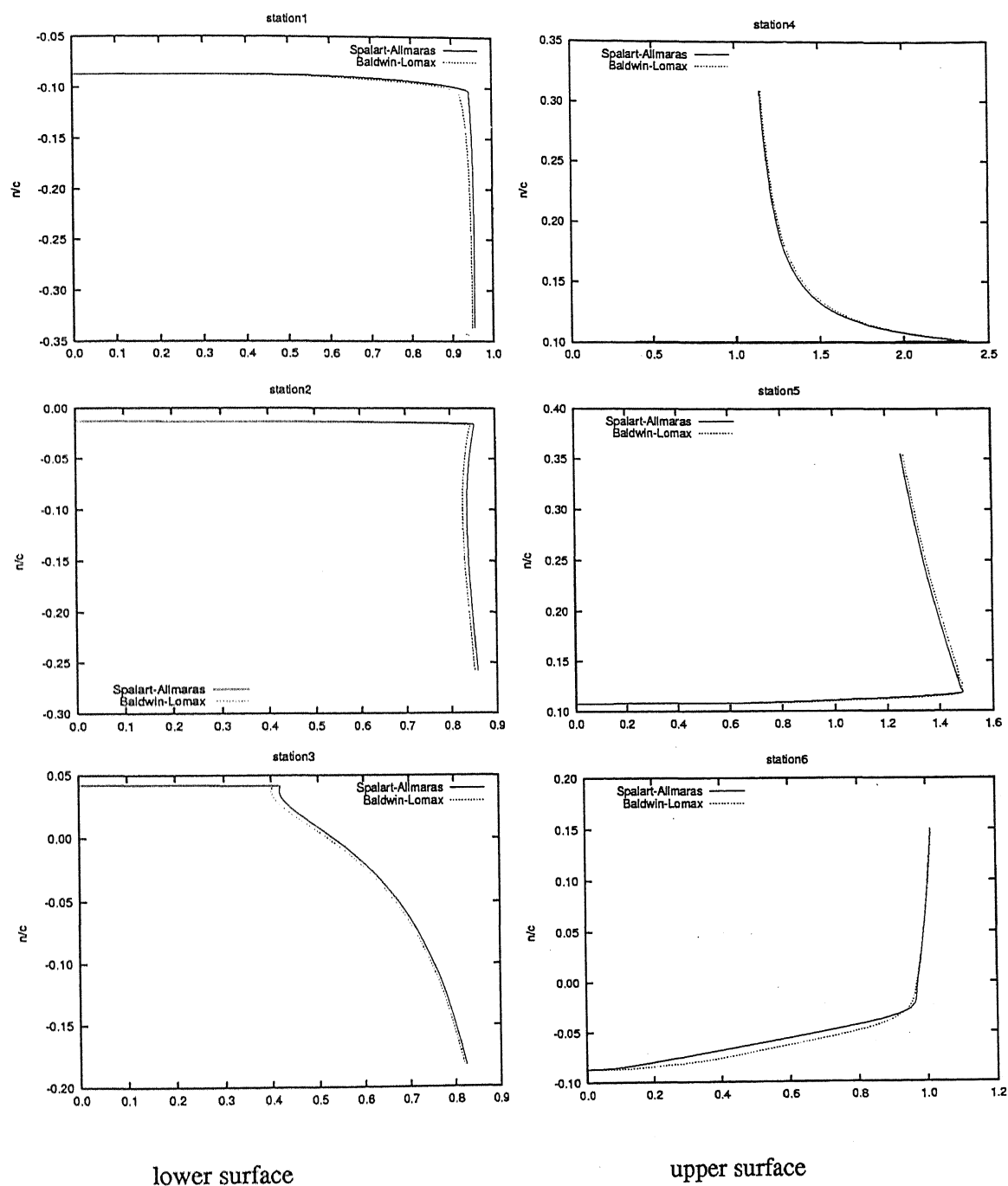


Figure 4.14: NACA 0012 airfoil: Velocity profiles at different stations over airfoil surface for $\alpha = 10^\circ$.

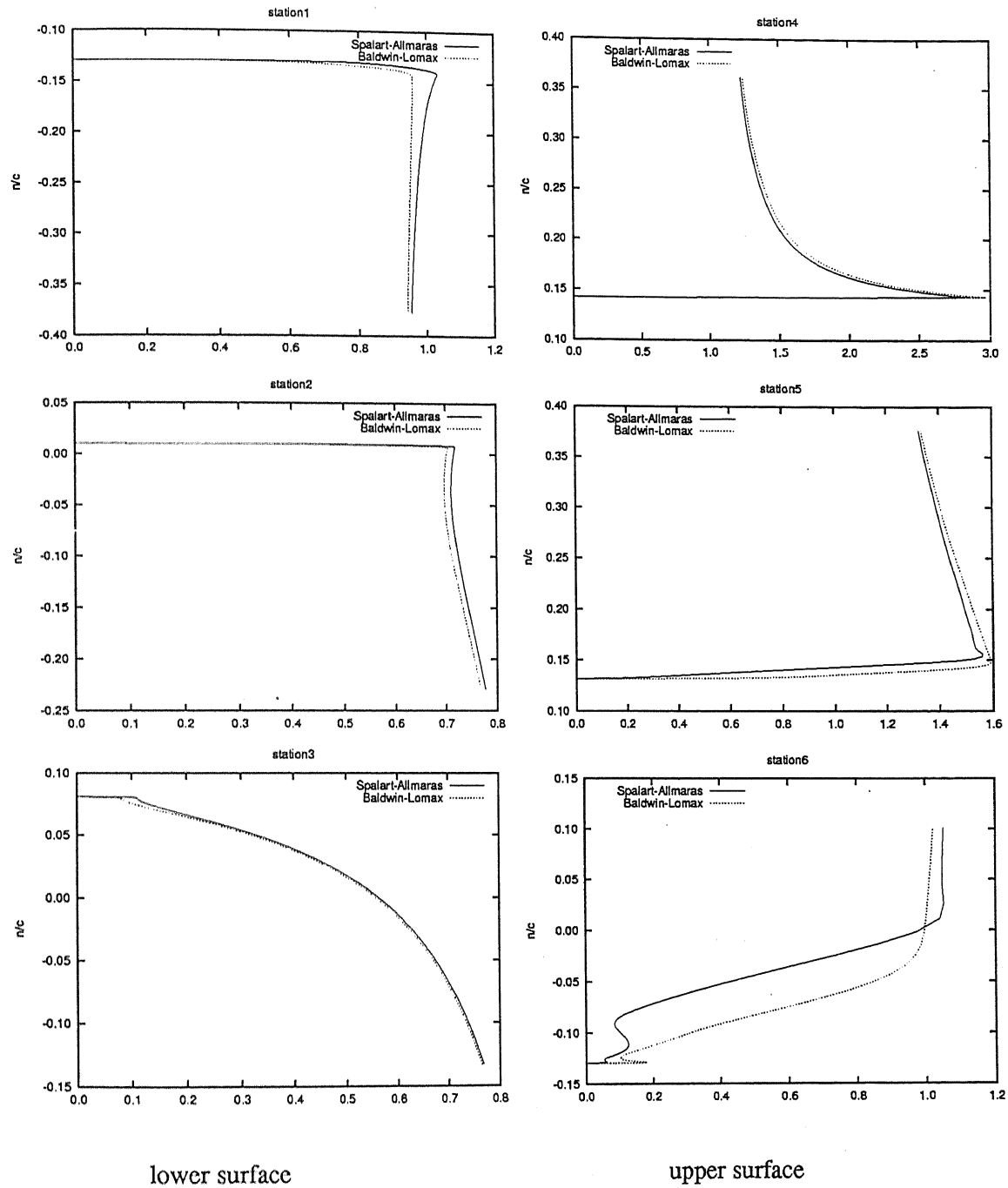


Figure 4.15: NACA 0012 airfoil: Velocity profiles at different stations over airfoil surface for $\alpha = 15^\circ$.

4.3 McDonnell Douglas Multi-Element Airfoil

4.3.1 Airfoil configuration

The high lift model investigated is a McDonnell Douglas aerospace(MDA) 2D 11.55% thick super critical, single flap, three element airfoil as shown in Figure 4.16(a). The slat chord is 14.48% and the flap chord is 30% of the stowed airfoil chord. The airfoil was configured in a typical approach/landing configuration with slat and flap deflections of 30° . This configuration is denoted as 30P-30N(slat deflection 30° , slat rigging positive, flap deflection 30° , flap rigging negative). Figure 4.16(b) defines the nomenclature for gap and overhang. The slat and flap setting for 30P-30N configuration has been shown in Table 4.4.

Nomenclature (Flap & Slat)	MD Geometry (30P-30N)
Slat Deflection(δ_s)	-30°
Slat Gap, %c	2.95
Slat Overhang, %c	-2.5
Flap Deflection (δ_f)	30°
Flap Gap, %c	1.27
Flap Overhang, %c	0.25

Table 4.4: Slat and Flap setting of Multi-Element airfoil

4.3.2 Computational Domain and Boundary Conditions

The airfoil rests in a rectangular domain. The grid extends $7c$ upstream and $11c$ downstream of the model to minimize inflow/outflow influence on the solution. The details of the meshes used for computations for various angle of attack have been summarized in Table 4.5. A close-up of the grid is shown in Figures 4.17 and 4.18. The structured mesh thickness over each body varies from $0.1c$ to $0.007c$. The meshes used in computation contains 457 points on main element, 198 points on slat and 200 points on flap. In order to control the unstructured mesh density in wake region, three fictitious boundaries are inserted to resolve the wake effectively. The spacing of the first point normal to the wall is 1×10^{-6} normalized to the chord length of the airfoil in the undeflected position.

This spacing yields a y^+ of less than 1.0 for the point next to the wall over main element.

On airfoil surface, no slip boundary condition for velocity and zero value for eddy viscosity have been specified while free stream values have been assigned for both velocity and eddy viscosity at the upstream boundary. At the downstream boundary, a Neumann type boundary condition for both velocity and eddy viscosity has been specified. At the upper and lower surface boundaries, the component of velocity normal to the component of stress vector along these boundaries have been prescribed zero value.

α	Mesh1		Mesh2	
	nodes	elements	nodes	elements
8^0	46916	92927	84320	167735
15^0	48760	96615	-	-
16^0	48760	96615	-	-
19^0	48368	95831	-	-
21^0	48236	95567	83052	165199
27^0	47669	94433	-	-

Table 4.5: Number of nodes and elements in Multi-Element mesh at different angle of attack.

The number of nodes and elements for $\alpha = 15^0$ & $\alpha = 16^0$ are the same since the mesh for $\alpha = 16^0$ is obtained by deforming the mesh for $\alpha = 15^0$ using a mesh-moving scheme.

4.3.3 Results

This section contains the comparison of computed and experimental results for various angle of attack at $Re = 9 \times 10^6$. For both the meshes the first point next to the wall is at a distance of 1.0×10^{-6} , which gives an average y^+ of 0.5 on the upper surface of main element. Mesh2 has also been used for computation at $\alpha = 8^0$ & $\alpha = 21^0$ to study mesh convergence.

4.3.3.1 Pressure distribution

$$\alpha = 8^\circ$$

Figure 4.19 shows the comparison of computed and experimental pressure distribution over slat, main element and flap for $\alpha = 8^\circ$. It has been observed that the computed results for mesh1 predict higher values whereas mesh2 predict lower values than the experimental values on the upper of the slat. However, on the lower surface of the slat, the computed results are in good agreement with the experimental results.

The main element pressure distribution shows a large suction peak near the leading edge followed by pressure recovery region. The pressure is not recovered to free stream level since the trailing edge is adjacent to the flap suction peak. The lower surface is characterized by high pressure (nearly stagnant flow $C_p = 1$). The free stream pressure in the present case has been assigned to zero for the computation of C_p distribution. On the upper surface, the computed results for mesh1 are in good agreement with experimental results, whereas the results for mesh2 predict slightly lower values than the experimental values.

The flap upper surface pressure distribution shows higher pressure recovery for mesh1 results than experiment, indicating higher separation near the trailing edge. However, the results obtained using SA model for mesh2 are in good agreement with the experimental results, while BL results for mesh2 show lesser pressure recovery than experiment, indicating lesser separation near trailing edge.

$$\alpha = 15^\circ$$

Pressure distribution on the slat, main element and flap has been shown in Figure 4.20 for $\alpha = 15^\circ$. No experimental data is available for this case, so the results have been compared for two different turbulence models. On the upper surface, BL shows higher suction peak near the leading edge of slat and flap, indicating higher pressure recovery. While both the models predict same results for main element.

$$\alpha = 16^\circ$$

Figure 4.21 shows pressure distribution on the slat, main element and flap for $\alpha = 16^\circ$. The computed results are in good agreement with the experimental results, except on the upper surface of the flap. On the flap upper surface, the SA model shows higher pressure recovery than experiment. Also it predicts larger suction peak than

experiment near the leading edge of the main element.

$$\alpha = 19^\circ, Re = 7 \times 10^6$$

Pressure distribution on the slat, main element and flap for $\alpha = 19^\circ$ at $Re = 7 \times 10^6$ has been shown in Figure 4.22. Experimental data is not available for this case, so the results have been reported for two different turbulence models. On the upper surface, BL predicts higher suction peak near the leading edge of slat and flap, indicating higher pressure recovery. While both the models show same results for main element.

$$\alpha = 19^\circ, Re = 9 \times 10^6$$

Figure 4.23 shows pressure distribution on the slat, main element and flap for $\alpha = 19^\circ$ at $Re = 9 \times 10^6$. The suction peaks are larger in this case than that at lower angle of attack. Again there is not much difference in pressure distribution for computed and experimental results, except on the upper surface of the flap. Near the leading edge of main element, SA model predicts larger suction peak than experiment. The computed pressure distribution of SA model is more close to the experiment than BL model in all the three elements.

$$\alpha = 21^\circ$$

Figure 4.24 shows pressure distribution on the slat, main element and flap for $\alpha = 21^\circ$. It has been observed that the computed results predict higher suction peak and also show significant differences from the experimental results on the upper and lower surfaces of the slat. However, on the main element the computed pressure distribution matches well with the experiment. While showing the C_p distribution over flap surface, SA model shows good agreement with the experiment, whereas BL results for both meshes predict higher values than experiment, followed by higher pressure recovery, indicating higher separation near trailing edge.

$$\alpha = 27^\circ$$

Pressure distribution on the slat, main element and flap has been shown in Figure 4.25 for $\alpha = 27^\circ$. Experimental data is not available for this case also, so the results have been compared for two different turbulence models. The suction peaks are having large values in this case than that at lower angle of attack. BL model shows larger suc-

tion peak near the leading edge of slat and flap than SA model, whereas in case of main element it shows same value of suction peak with lesser pressure recovery on the upper surface. The flap upper surface pressure distribution shows higher pressure recovery for BL model than SA model, indicating higher separation near the trailing edge.

In general, the agreement between the C_p data of the experiment and all two of the turbulence models is quite good. The biggest discrepancies occur for the lower angle of attack, particularly on the slat and the flap. The greater the region of flow separation on the flap, the lower the lift on the flap and slat. The BL model shows higher flow separation on the flap: a flattening of the C_p distribution near the trailing edge. It has been observed that the SA model results in C_p distributions that are closer to experimental observations.

4.3.3.2 Velocity profiles

Velocity profiles have been presented at six stations for $\alpha = 19^\circ$ and four stations for rest of the angle of attacks. The chord wise locations for velocity profiles, shown in Figure 4.26, are listed in the Table 4.6.

Station No	x/c
1	0.1075
2	0.45
3	0.85
4	0.89817
5	1.0321
6	1.1125

Table 4.6: Multi-element airfoil: Location of stations from leading edge for showing velocity profiles.

$\alpha = 8^\circ$

Figure 4.27 & 4.28 show the contours of the velocity magnitude, pressure fields, eddy viscosity for mesh1 and mesh2, respectively. Velocity profiles at different stations have been shown in Figure 4.29. According to the experimental data, the main element boundary layer edge is just below $n/c = 0.01$ (Fig. 4.29, station 1). The slat wake passes just above the boundary layer and shows very little velocity deficit. The result obtained

using BL model for mesh1 is in good agreement with the experimental result, whereas the BL result for mesh2 shows higher momentum deficit in the slat wake and thicker boundary layer than the experiment. The SA result for mesh1 is very close to the experimental result but shows slightly wider slat wake. The SA result for mesh2 does not show good match with experimental results.

Velocity profile on the flap near the leading edge has been presented in Figure 4.29(station 4). The profile in this region usually consists of four levels. Going from the surface outward these four levels are: (1) flap boundary layer, (2) slot flow through the flap gap, (3) main element wake, and (4) slat wake. Slat boundary layer is extremely thin at this location. Experimentally, the slot flow extends from $0.001 \leq n/c \leq 0.01$ and is ramp shaped indicating strong viscous effects on the slot flow coming through the flap gap. These viscous effects are quite possibly generated by the separated and recirculating flow in the flap cove. The main element wake extends from $n/c = 0.01$ to $n/c = 0.025$. Both the models for mesh1 show good agreement with the experimental result while BL model for mesh2 under predicts the edge velocity in flap boundary layer and also predicts too deeper slat and main element wake and no where close to the experimental result. Also, the SA model for mesh2 under predicts the velocity magnitude above the main element wake and not in good agreement with the experiment. Experimental result does not show any slat wake deficit whereas computed results show wide slat wake.

The velocity magnitude obtained using SA model for both meshes and BL model for mesh1 is almost close to the experimental result while BL model for mesh2 predicts too deeper main element and slat wake(Fig. 4.29, station 5). The velocity magnitude of flap boundary layer near trailing edge(Fig. 4.29, station 6) is completely dispersed.

$$\alpha = 15^\circ$$

The velocity magnitude, pressure fields, eddy viscosity contours have been shown in Figure 4.30. Velocity profiles on main element for all three stations have been shown in Figure 4.31 and on flap in Figure 4.32 for two different turbulence models. There are no experimental results available for this angle of attack.

$$\alpha = 16^\circ$$

Figure 4.33 shows the velocity magnitude, pressure fields, eddy viscosity contours for 16° angle of attack. Velocity profiles at various stations have been shown in Fig-

गुरुबोत्तम काशीनाथ केलकर पुस्तकालय
भारतीय प्रौद्योगिकी संस्थान कानपुर
अवधि क्र. A...148871.....

ure 4.34. At the leading edge of the flap(station 4), the velocity profile shows good agreement with experiment in predicting main element wake. However, on main element it shows higher velocity deficit in the slat wake, but it predicts overall good result with experiment. While considerable scattering has been observed in the prediction of flap velocity profiles, especially at the station 5(mid-chord position) and station 6(trailing edge) of the flap.

$$\alpha = 19^\circ, Re = 7 \times 10^6$$

Velocity magnitude, pressure fields, eddy viscosity contours have been shown in Figure 4.35. Velocity profiles on main element for all three stations have been shown in Figure 4.36 and on flap in Figure 4.37 for two different turbulence models. There are no experimental results available for this angle of attack.

$$\alpha = 19^\circ, Re = 9 \times 10^6$$

Figure 4.38 shows the velocity magnitude, pressure fields, eddy viscosity contours for $\alpha = 19^\circ$, $Re = 9 \times 10^6$. Velocity profiles on main element for all three stations have been shown in Figure 4.39. In this case slat wake has been predicted nicely well by both the turbulence models. The results obtained by SA model are in good agreement with the experimental results, while BL model over predicts the results. Velocity profiles on the flap have been presented in Figure 4.40. At the leading edge of the flap(station 4), the velocity profile shows good agreement with experiment in predicting main element wake. While SA model shows higher velocity deficit in the slat wake, but it predicts overall good result with experiment. There is considerably more scattering in the prediction of flap velocity profiles than those of main element, especially at the station 5(mid-chord position) and station 6(trailing edge) of the flap.

$$\alpha = 21^\circ$$

The velocity magnitude, pressure fields, eddy viscosity contours have been presented in Figure 4.41, 4.42 for mesh1 & mesh2, respectively. Velocity profiles at different stations have been presented in Figure 4.43. In this case slat wake has been predicted nicely by SA turbulence model. The SA model results show overall good agreement with the experimental results. On main element(station 1), the SA result for mesh1 quite close to the experimental result but shows slightly higher velocity deficit in the slat wake, while the SA result for mesh2 predicts much more higher velocity deficit in the

slat wake. At the leading edge of the flap(station 4), the velocity profile computed by SA model shows good agreement with experiment in predicting main element wake as well as exhibits overall good agreement. While significant scattering has been observed in the prediction of flap velocity profiles, especially at the station 5(mid-chord position) and station 6(trailing edge) of the flap.

$$\alpha = 27^\circ$$

Figure 4.44 presents the velocity magnitude, pressure fields, eddy viscosity contours for $\alpha = 27^\circ$. Velocity profiles on main element for all three stations have been shown in Figure 4.45 and on flap in Figure 4.46 for two different turbulence models. There are no experimental results available for this angle of attack.

In general, the agreement between the experimental and computational velocity profiles is fairly good. One of the biggest differences between the computations has been observed at $\alpha = 8^\circ$: the velocity defect of slat wake is very small(at the station 1) in the experimental data, whereas all the computations predict much larger defect. This is bit larger in mesh2 results, and less so on the mesh1 calculations. So, it is difficult to conclude which model is giving the best results overall, since none of the models agree completely with the experimental results, and differences between different computations are small.

It is well known that stall occurs near $\alpha = 21^\circ$. But it is clear from Figure 4.44 that the flow over main element and flap is still fully attached and as a result of that both the models are not capable of predicting stall even at $\alpha = 27^\circ$.

4.3.3.3 Force and Pitching moment

Computed lift force(at $Re = 9 \times 10^6$) has been compared with experimental results and presented in Figure 4.47. The experimental lift curve shows relatively linear behaviour up to $\alpha = 12^\circ$, followed by a gradual rounding, whereas C_{lmax} occurs near $\alpha = 21^\circ$ and mildly stalls thereafter. Computed results also show similar trends but predict higher C_{lmax} than the experimental result. The lift curve obtained by SA model shows linear behaviour upto $\alpha = 15^\circ$, and thereafter loses its linearity. The flap lift compares very well with the experiment. While the slat lift is slightly higher than experiment and the

main element lift compares sufficiently good before $\alpha = 19^\circ$ but the experimental curve shows a drop in lift at $\alpha = 21^\circ$. There seems to be a constant increment in lift in the computed results. The lift values are all quite close up to 16° , as anticipated by the C_p results. None of the models agree with experimental value of maximum lift. This is most likely because the experiment does start to undergo some 3D effects become significant at high values of lift.

The drag force has been shown in Figure 4.48. It has been observed that C_d is not well predicted by any models but SA model's prediction is better than BL model. In the present work the drag has been computed by integrating the pressure and skin friction forces on the surface. This method has been shown [36] to be less accurate than other methods (such as wake integration), and may be the cause of large errors in the computed C_d . Pitching moment has been shown in Figure 4.49. The pitching moment coefficient predictions are good for SA model at the lower angle of attack, although they differ from BL model. The trend of increasing slope in C_m between $\alpha = 12^\circ$ and 16° is not predicted by any model. Comparison shows that SA model over predicts the result while BL model under predicts.

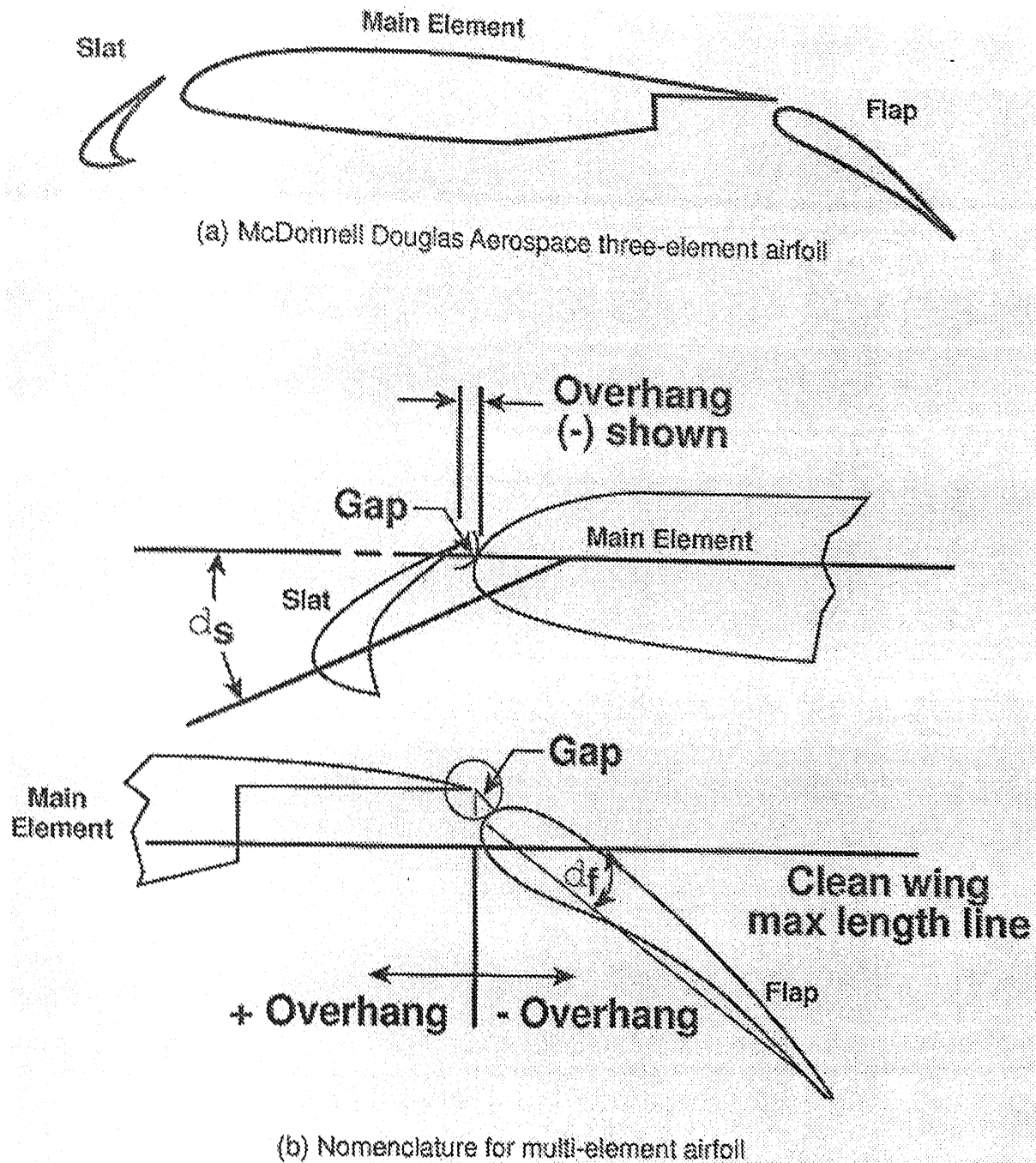


Figure 4.16: McDonnell Douglas Multi-Element Airfoil: Model geometry & Nomenclature (as given in the paper [17]).

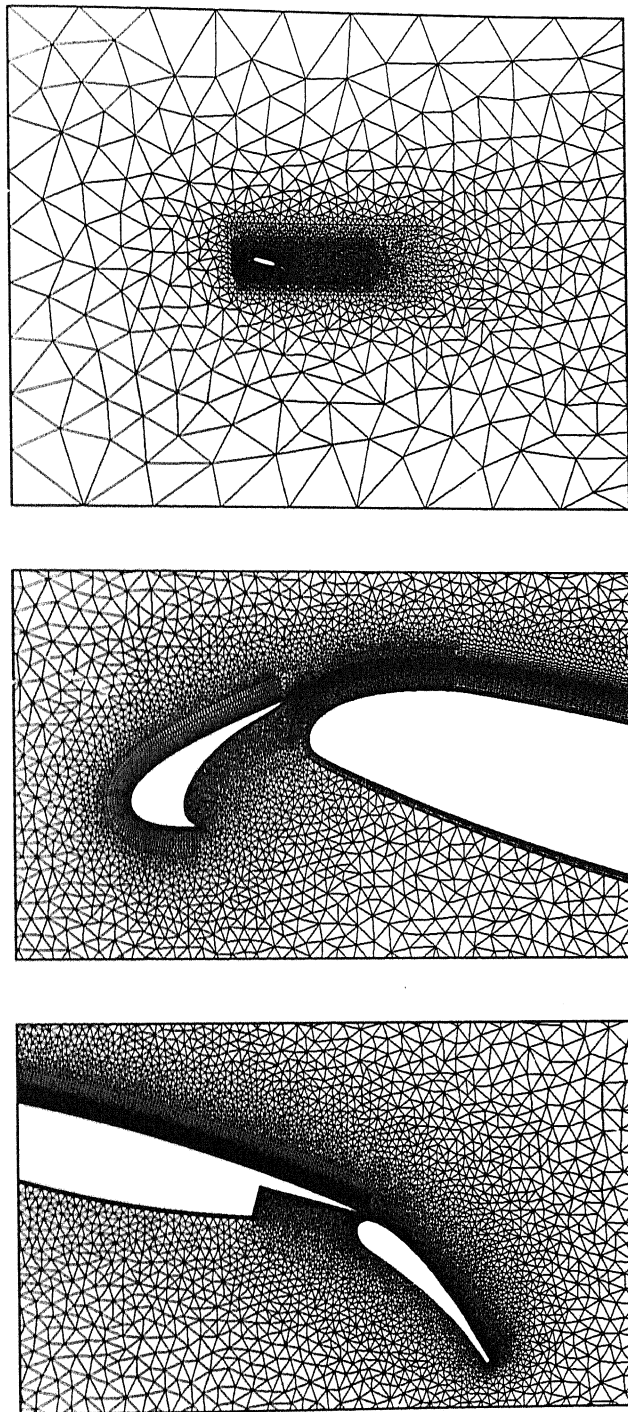


Figure 4.17: Typical Finite Element Mesh shown for $\alpha = 15^\circ$, consists of 48760 nodes and 96615 elements.

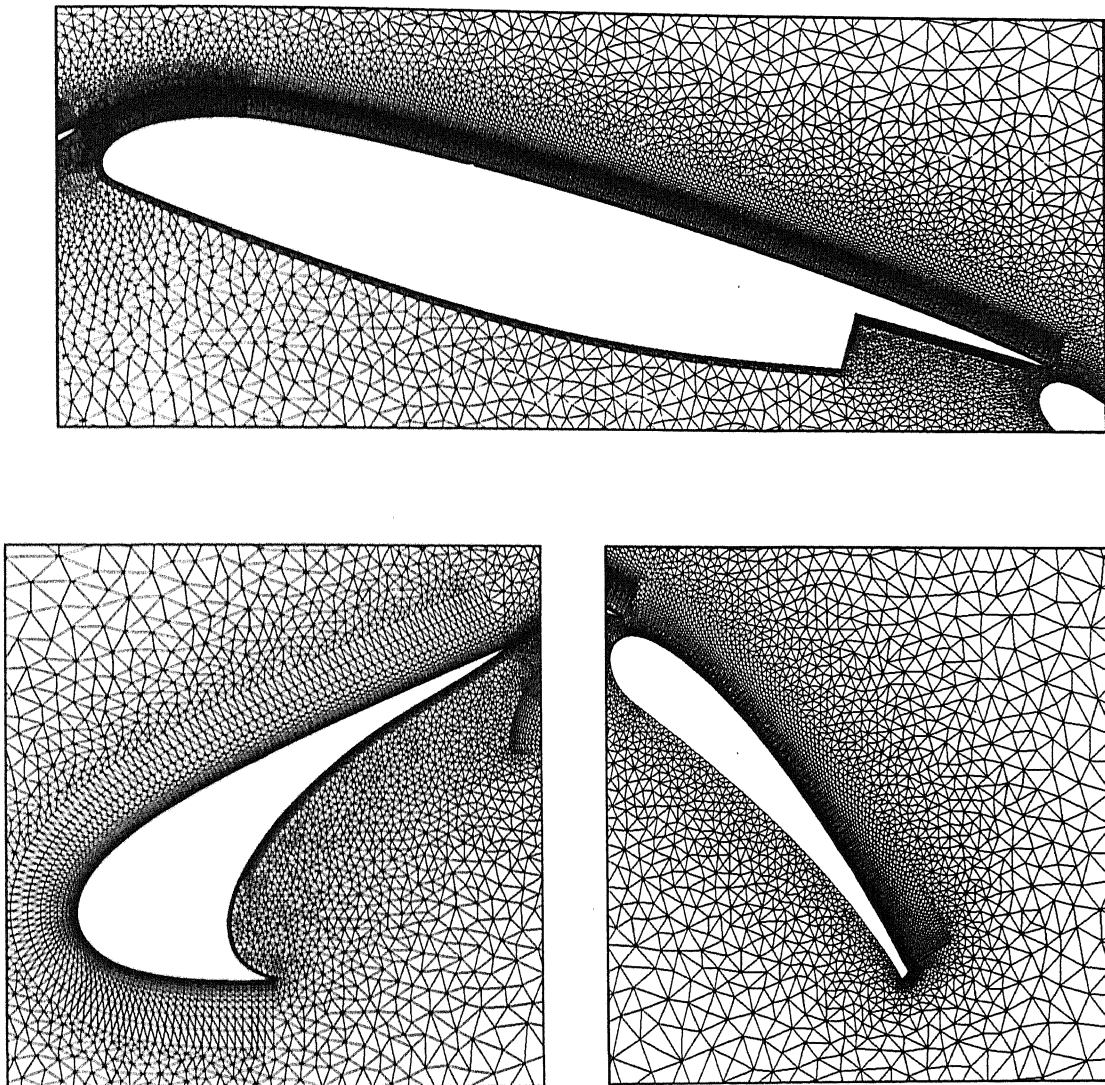


Figure 4.18: Finite Element Mesh for $\alpha = 15^\circ$ showing close-up of main-element, slat and flap.

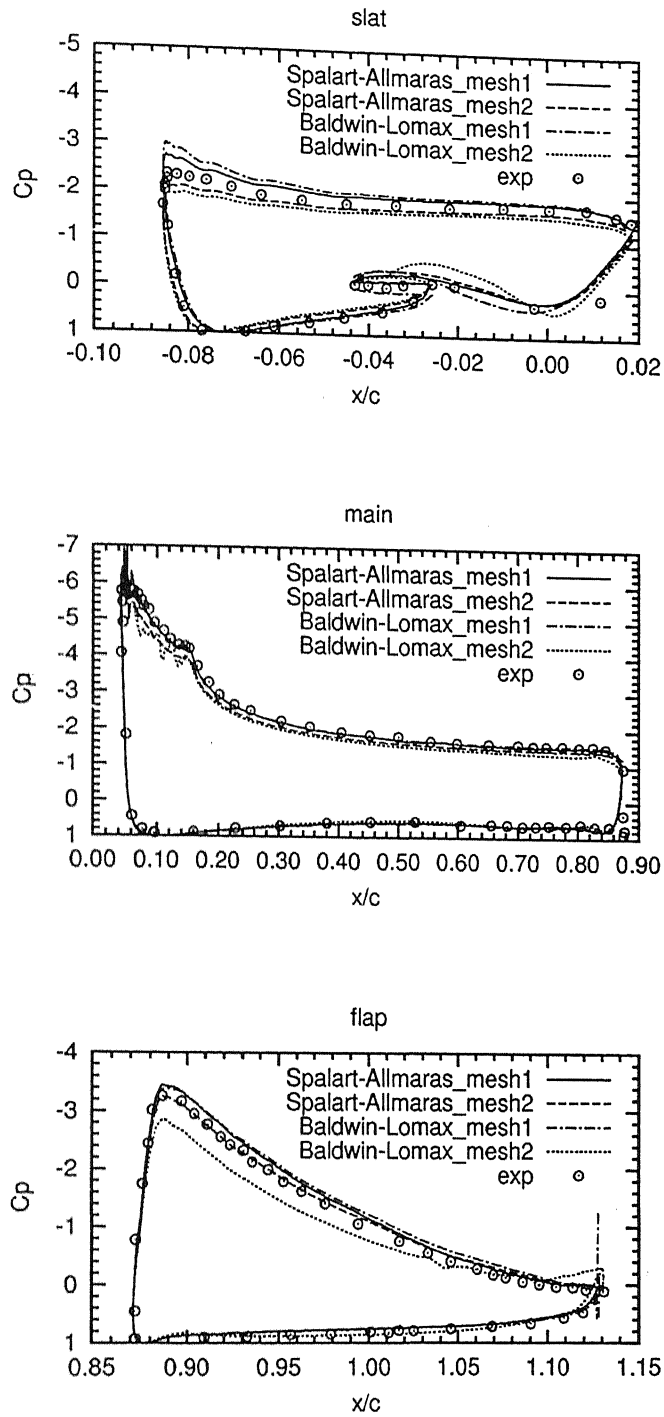


Figure 4.19: Pressure distribution over multi-element surfaces for $\alpha = 8^\circ$.

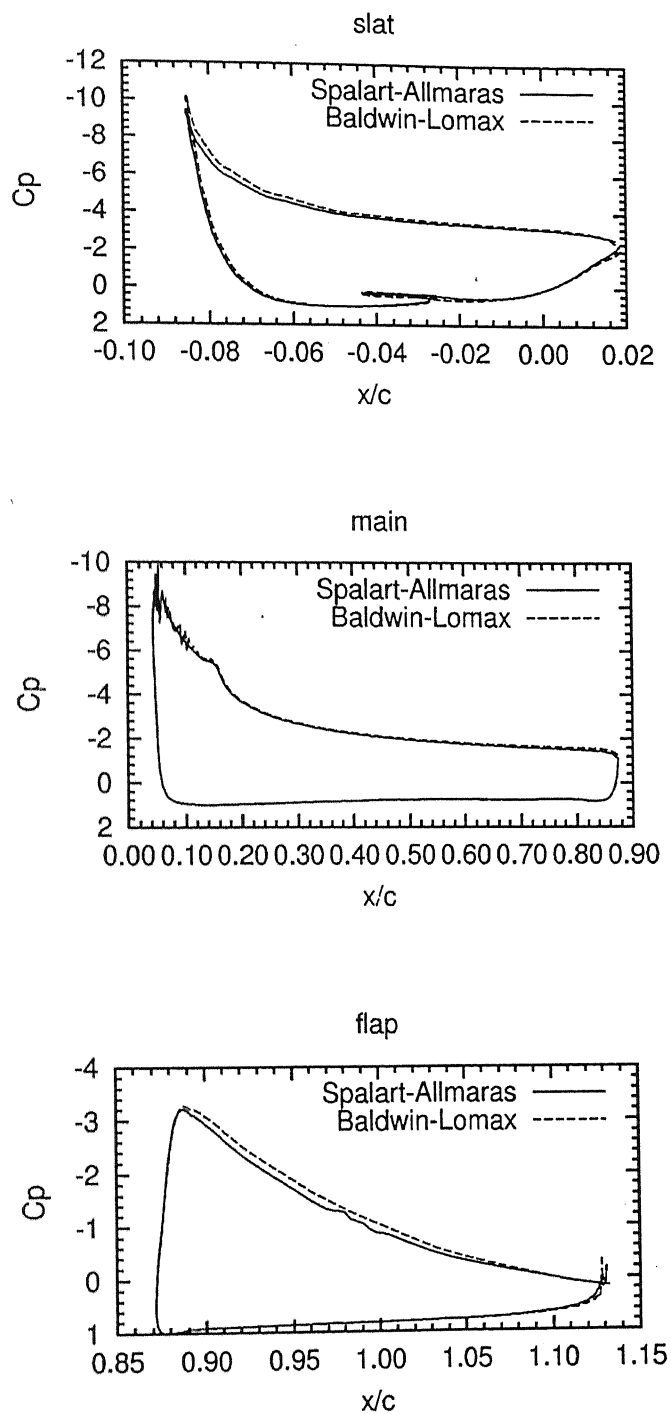


Figure 4.20: Pressure distribution over multi-element surfaces for $\alpha = 15^\circ$.

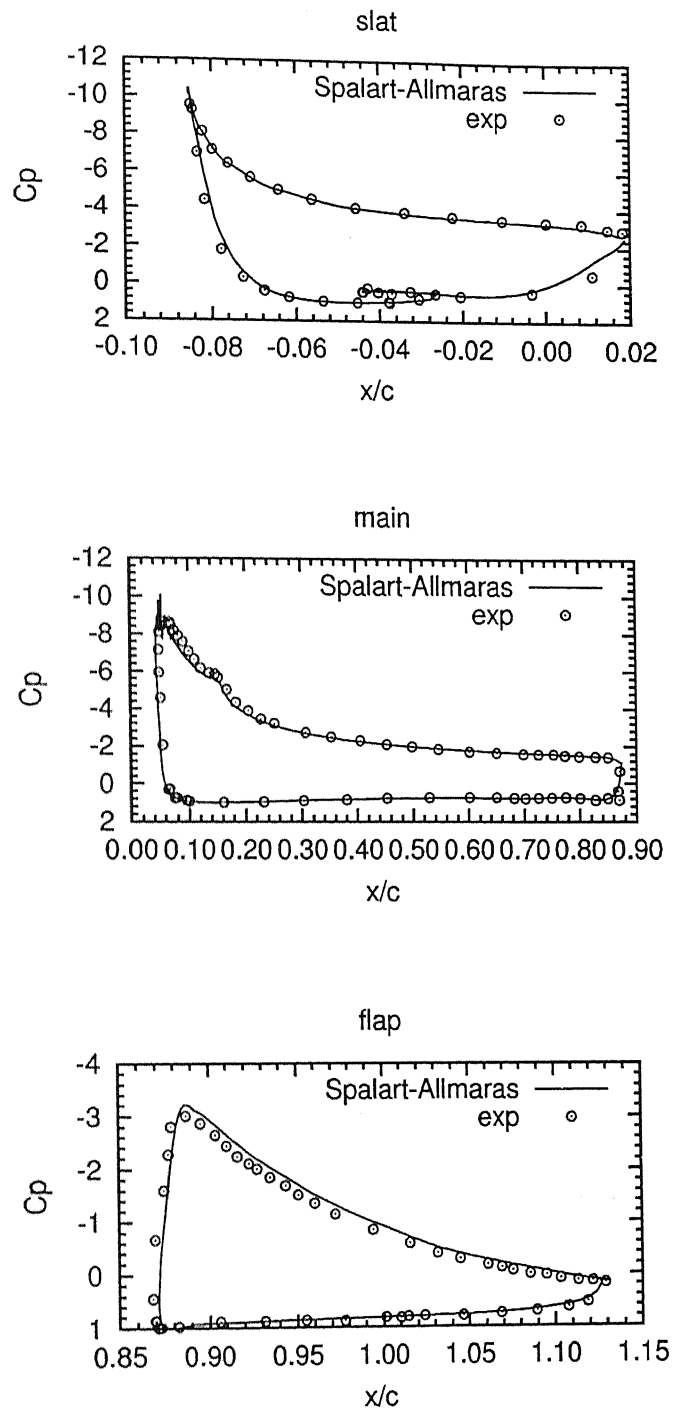


Figure 4.21: Pressure distribution over multi-element surfaces for $\alpha = 16^\circ$.

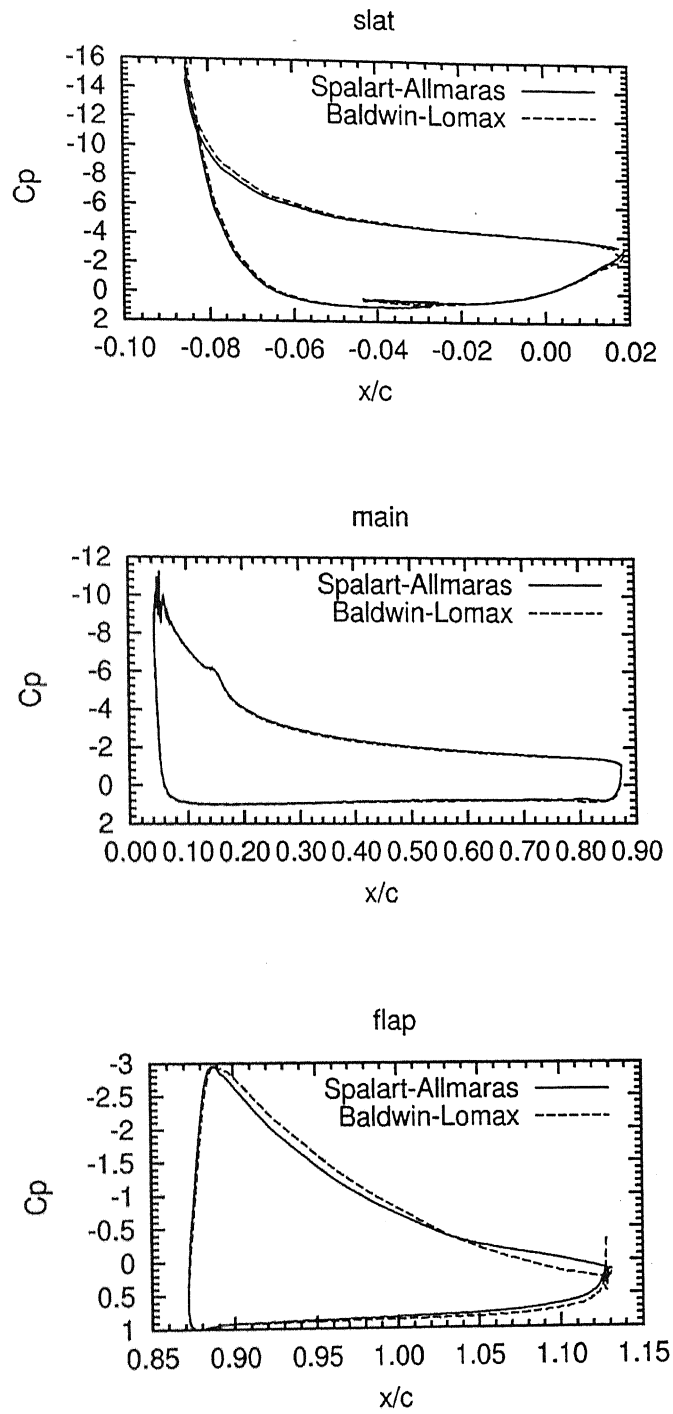


Figure 4.22: Pressure distribution over multi-element surfaces for $\alpha = 19^\circ$, $Re = 7 \times 10^6$.

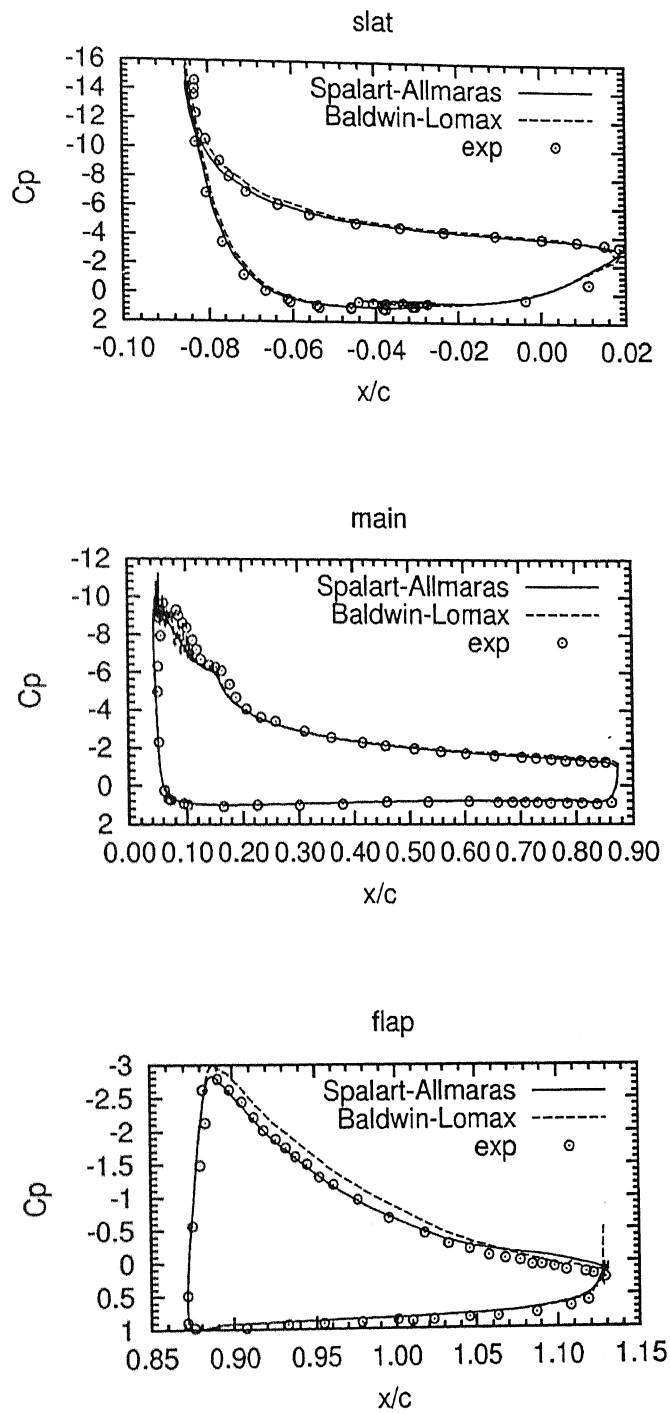


Figure 4.23: Pressure distribution over multi-element surfaces for $\alpha = 19^\circ$, $Re = 9 \times 10^6$.

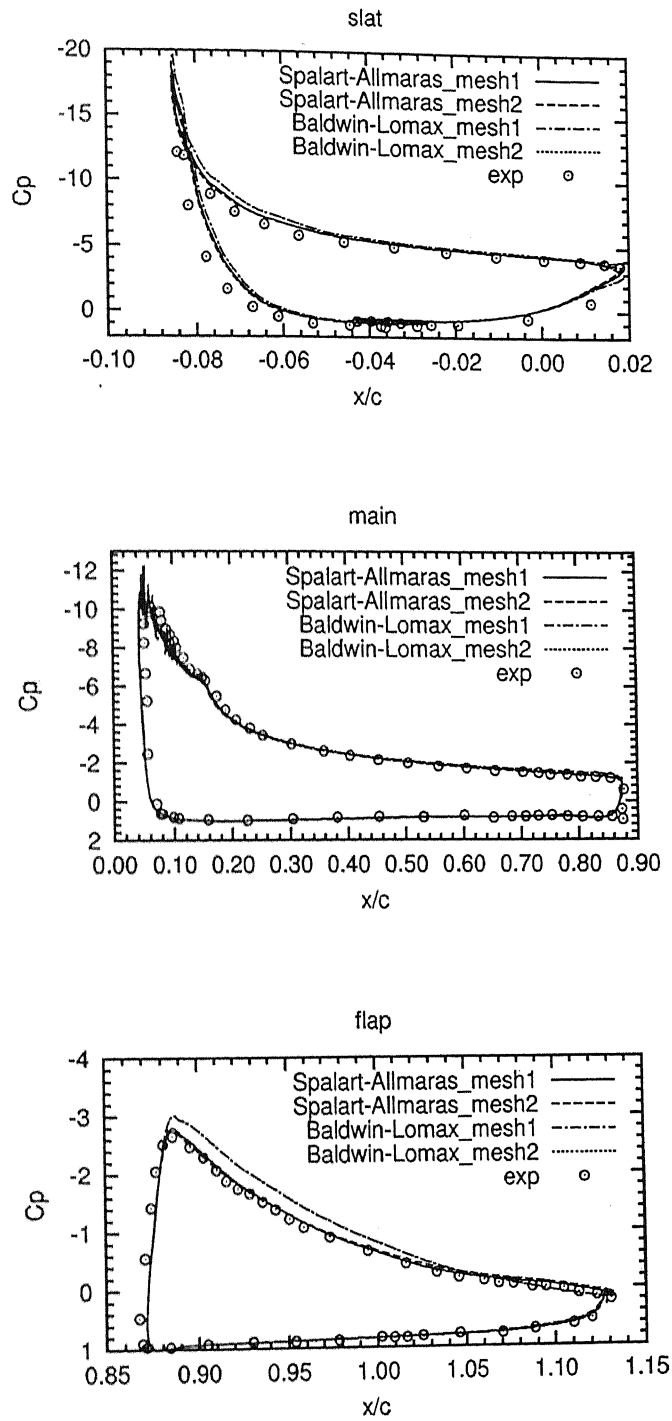


Figure 4.24: Pressure distribution over multi-element surfaces for $\alpha = 21^\circ$.

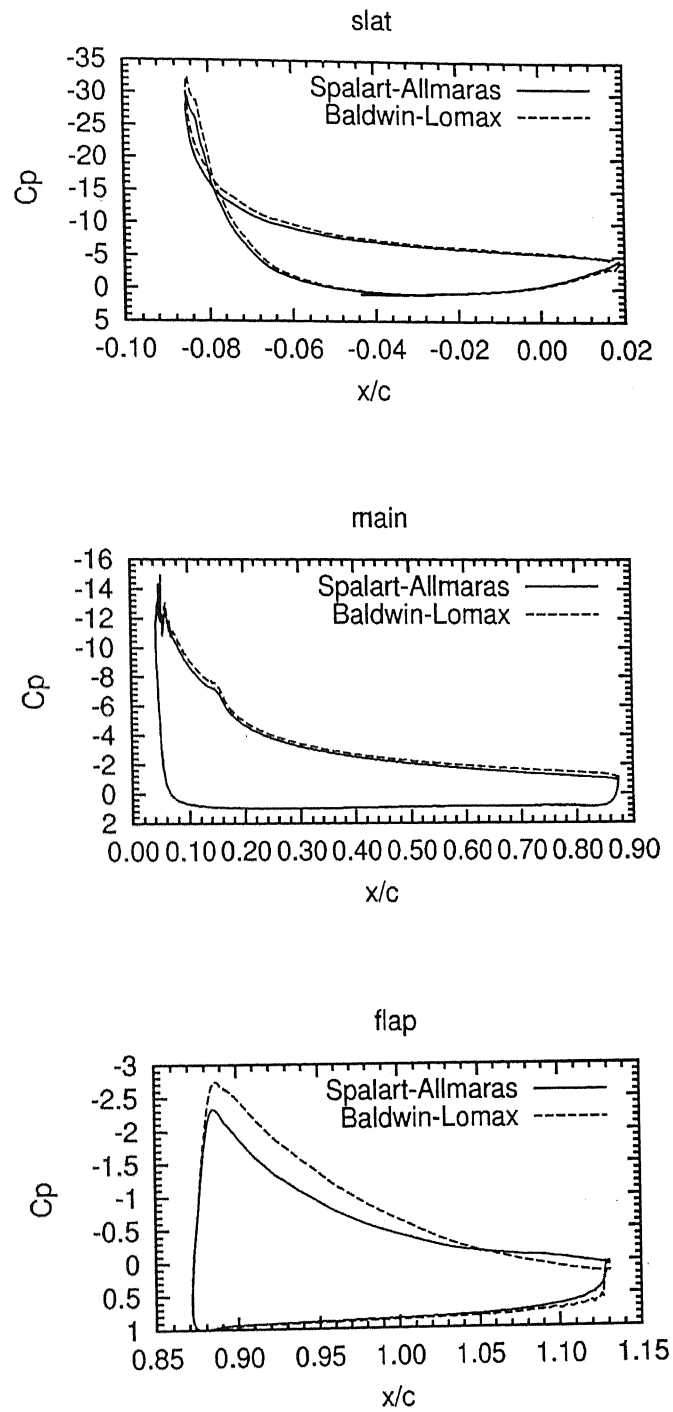


Figure 4.25: Pressure distribution over multi-element surfaces for $\alpha = 27^\circ$.

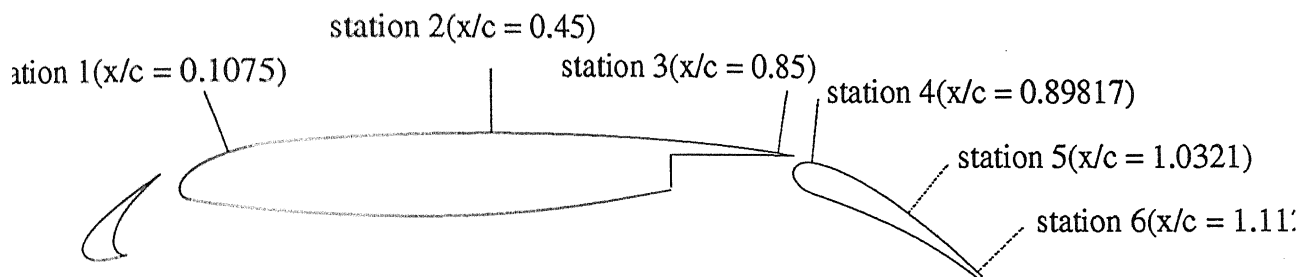


Figure 4.26: Multi-Element Airfoil: Location of stations from leading edge, for showing velocity profiles.

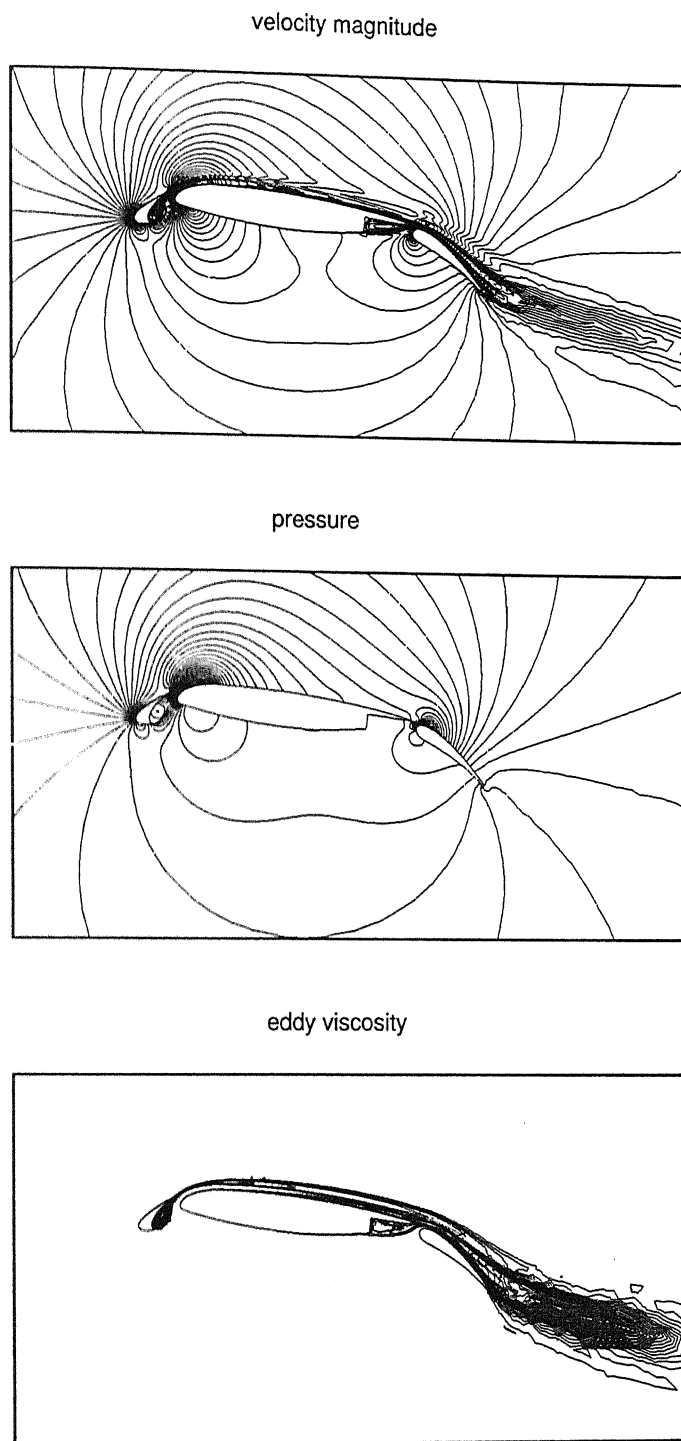


Figure 4.27: Multi-element airfoil: Contours of velocity magnitude, pressure fields, eddy viscosity for mesh1 at $\alpha = 8^\circ$, $Re = 9 \times 10^6$.

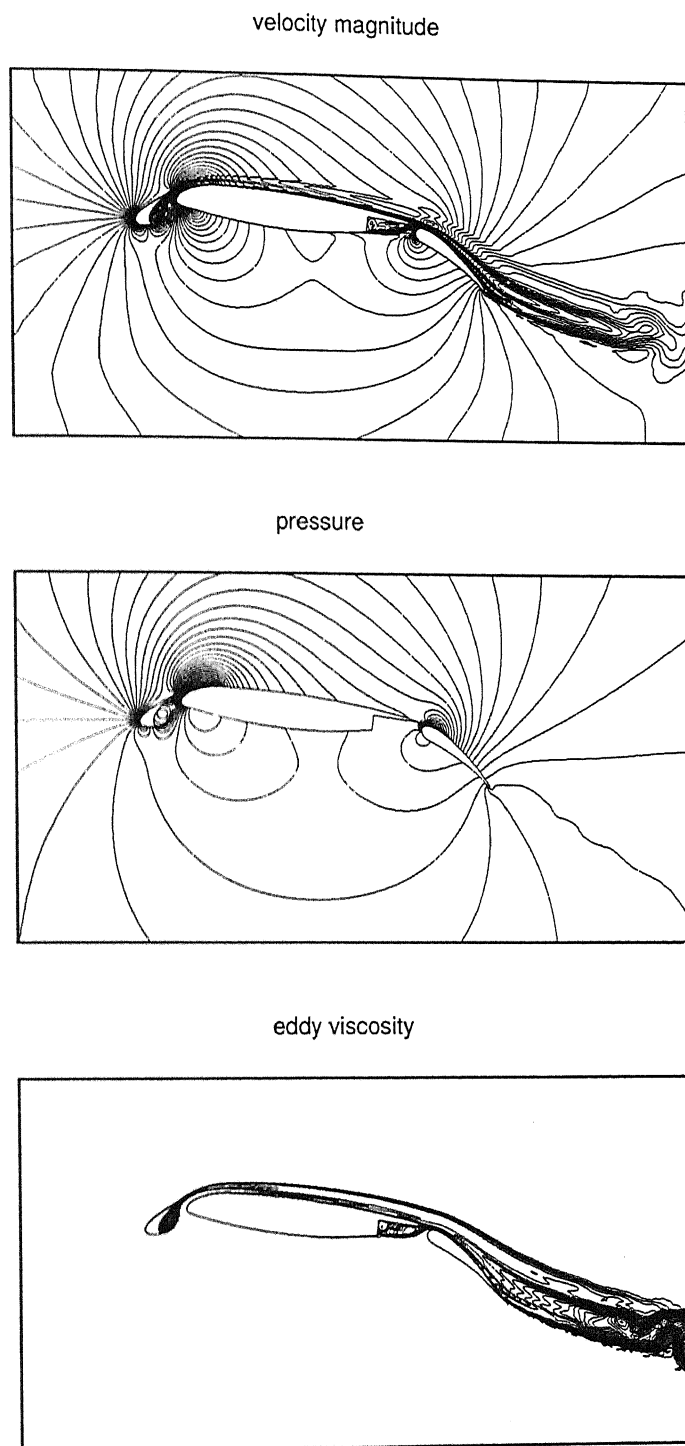


Figure 4.28: Multi-element airfoil: Contours of velocity magnitude, pressure fields, eddy viscosity for mesh2 at $\alpha = 8^\circ$, $Re = 9 \times 10^6$.

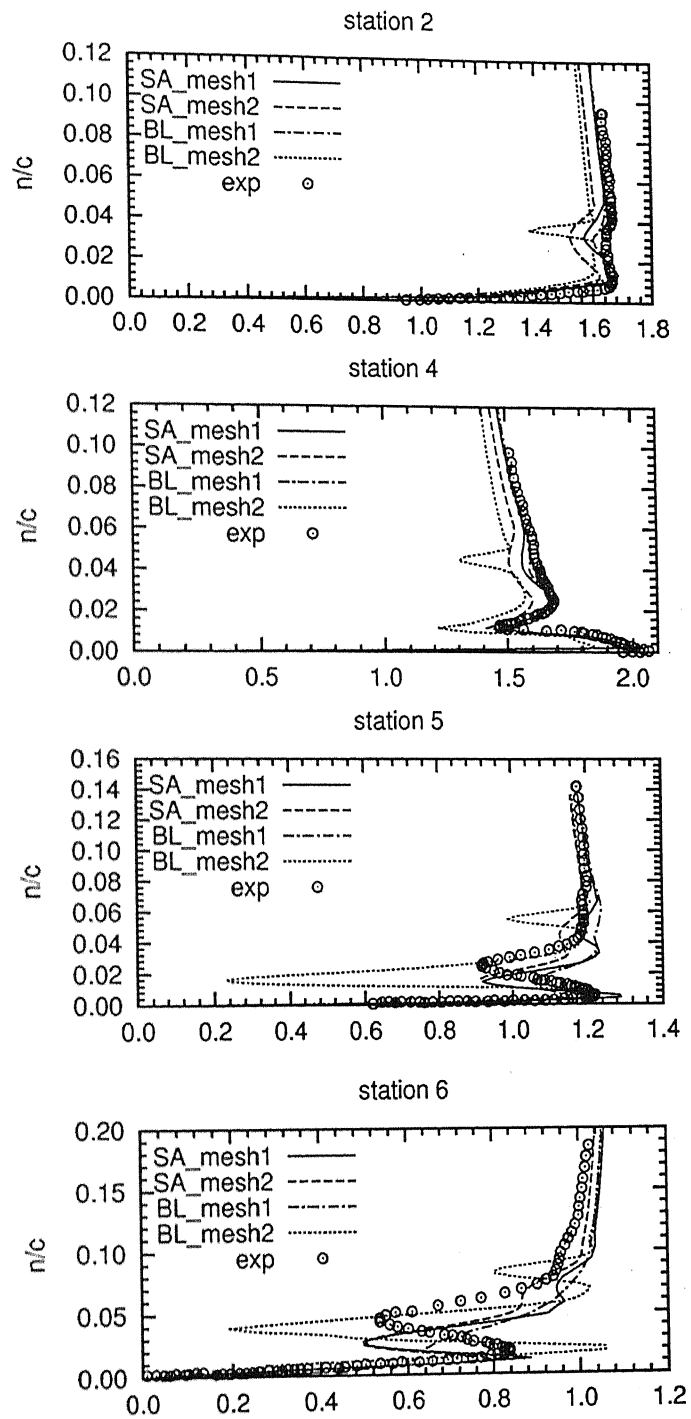


Figure 4.29: Multi-element airfoil: velocity distribution at $\alpha = 8^\circ$, $Re = 9 \times 10^6$.

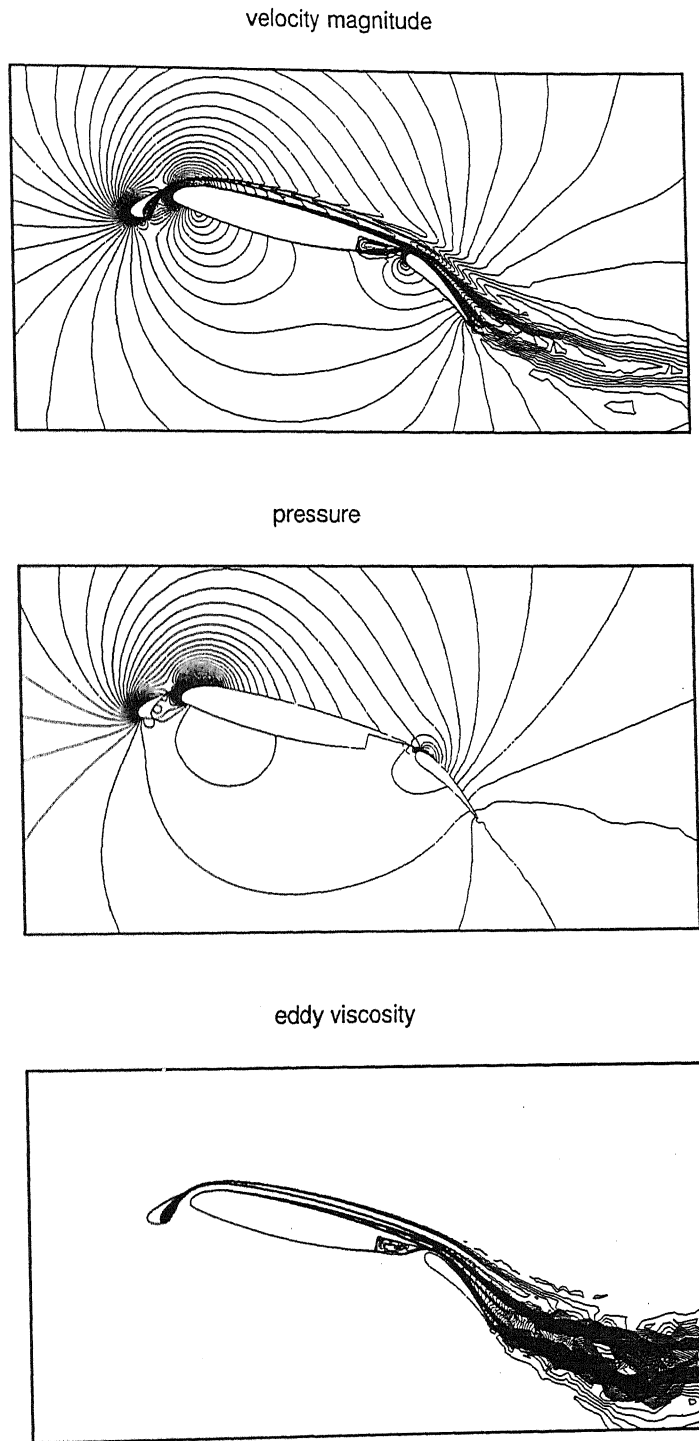


Figure 4.30: Multi-element airfoil: Contours of velocity magnitude, pressure fields, eddy viscosity at $\alpha = 15^\circ$, $Re = 9 \times 10^6$.

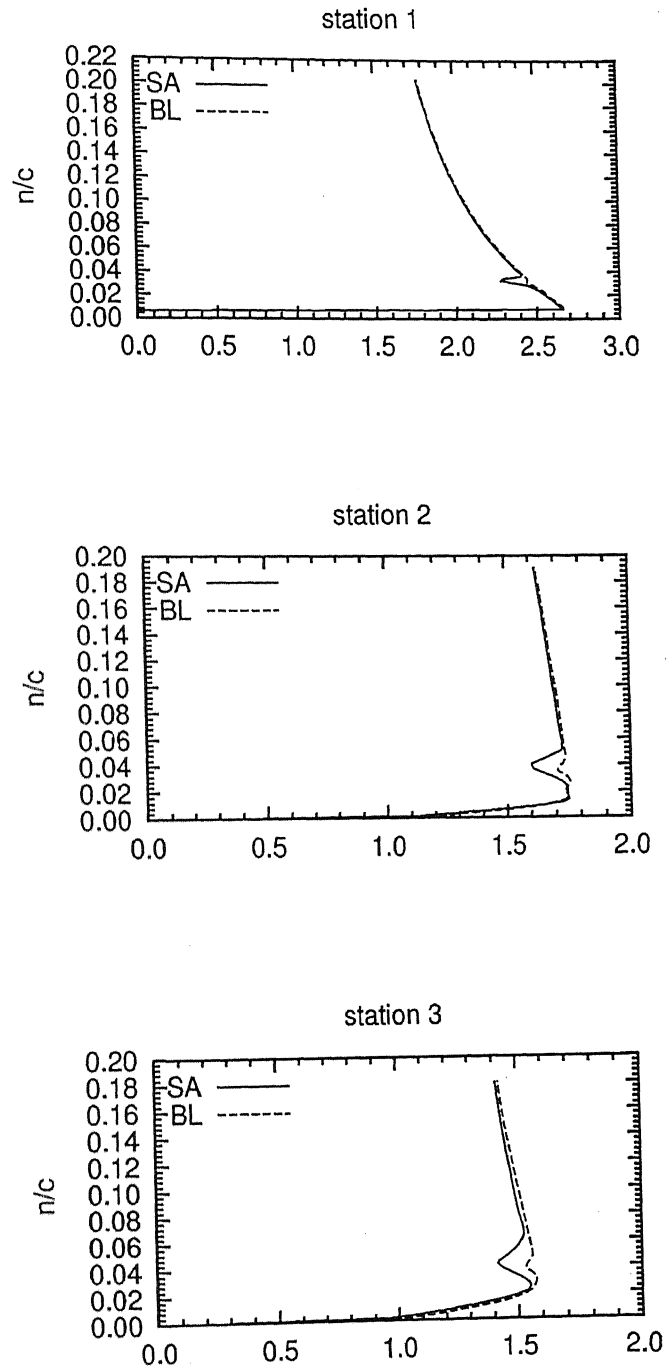


Figure 4.31: Multi-element airfoil: velocity distribution on main element at $\alpha = 15^\circ$, $Re = 9 \times 10^6$.

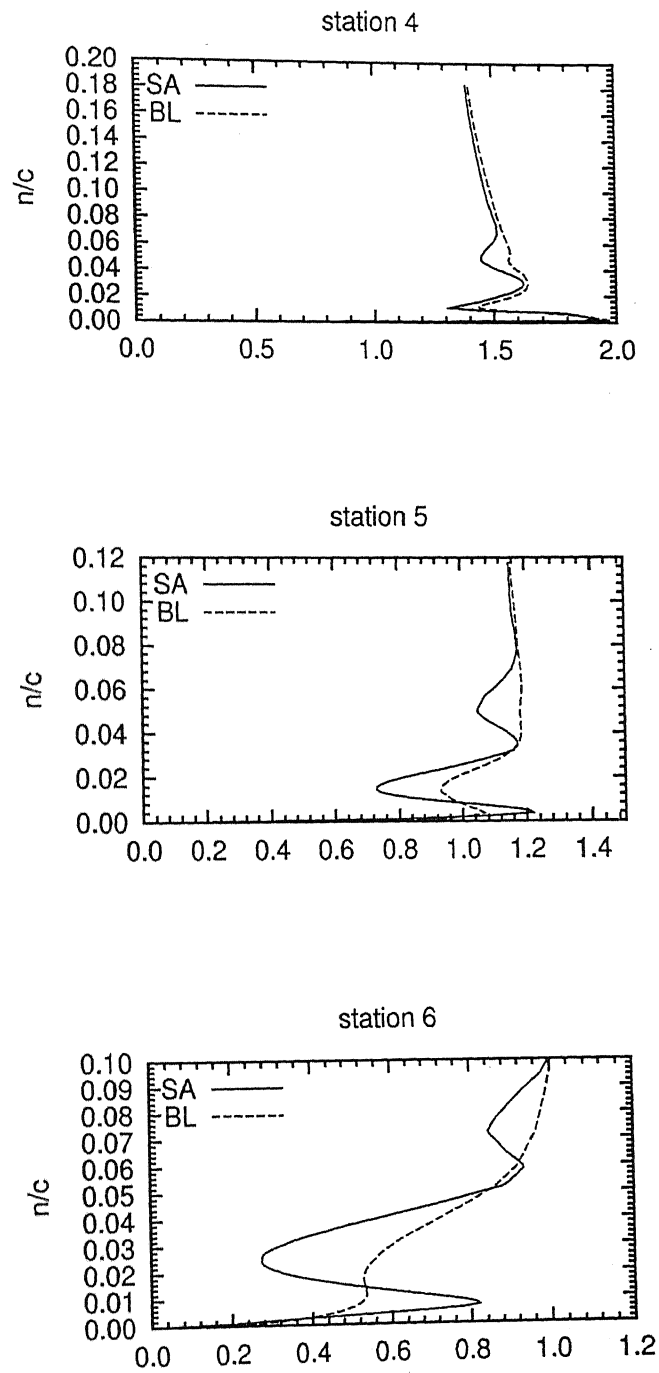


Figure 4.32: Multi-element airfoil: velocity distribution on flap at $\alpha = 15^\circ$, $Re = 9 \times 10^6$.

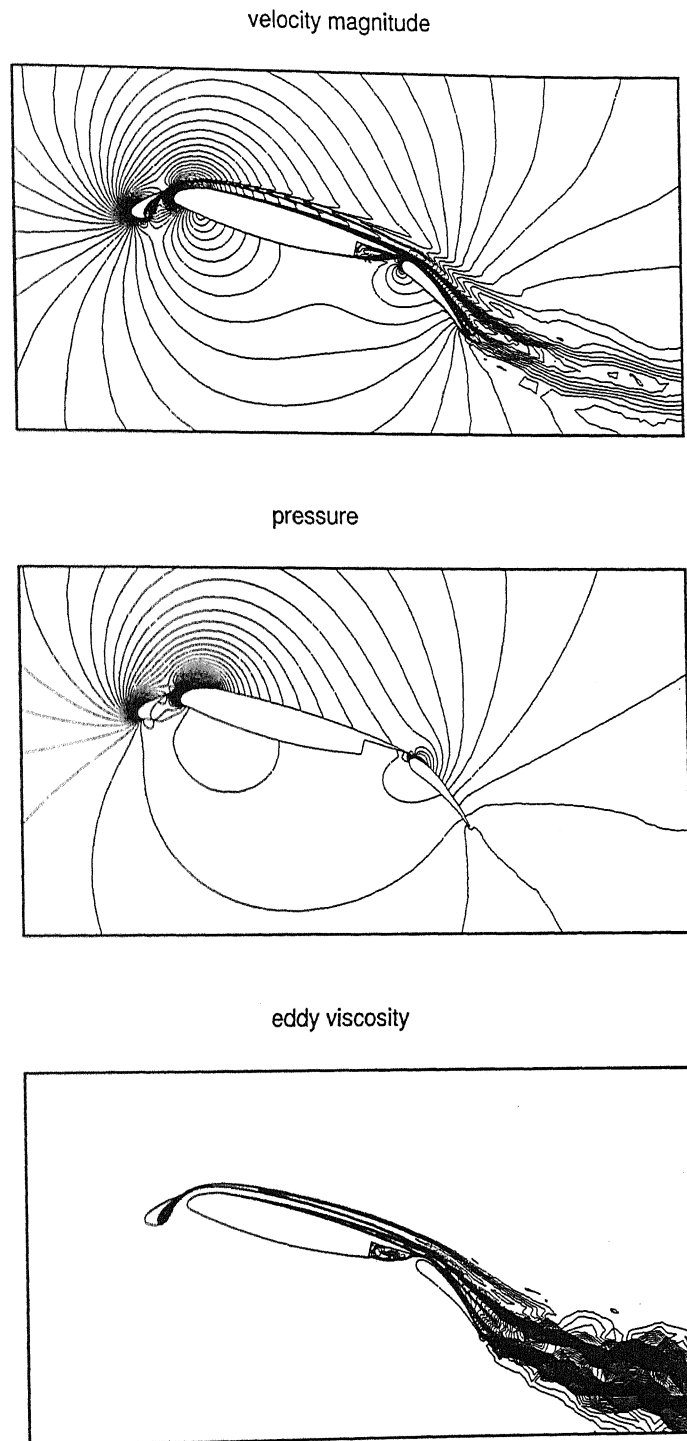


Figure 4.33: Multi-element airfoil: Contours of velocity magnitude, pressure fields, eddy viscosity at $\alpha = 16^\circ$, $Re = 9 \times 10^6$.

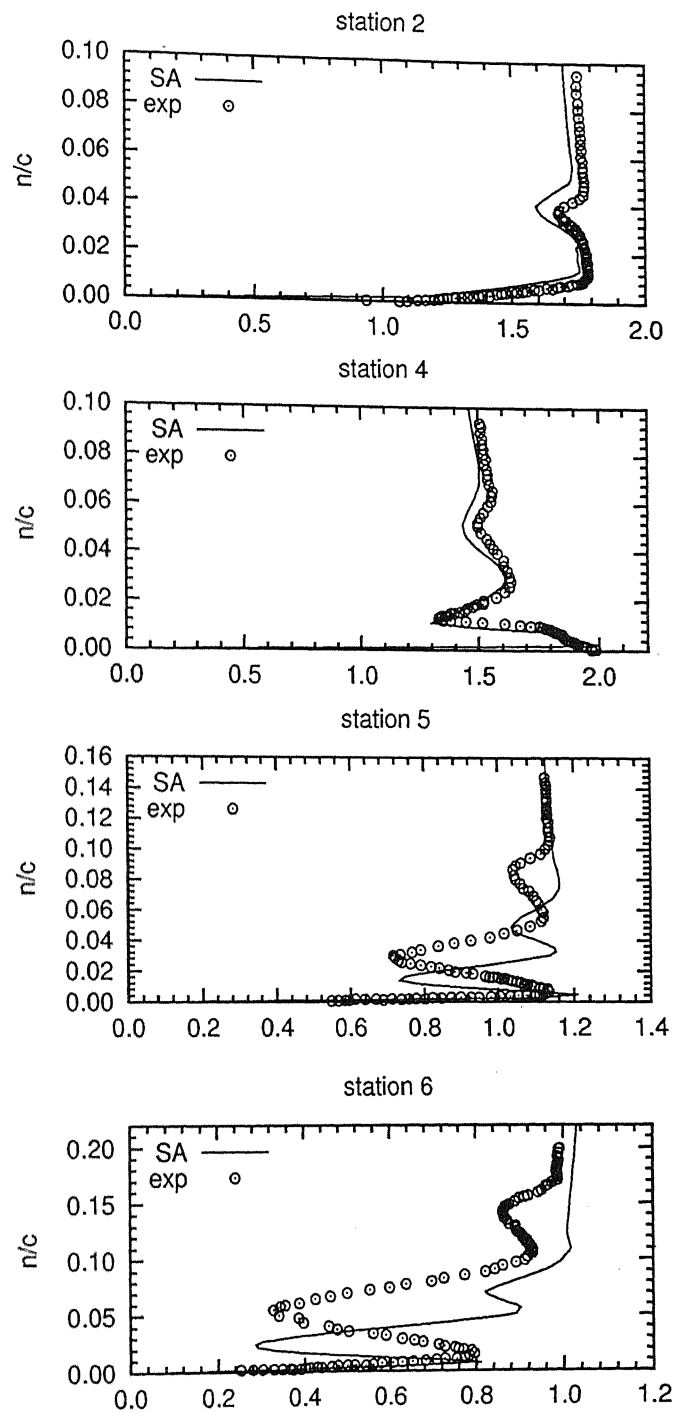


Figure 4.34: Multi-element airfoil: velocity distribution at $\alpha = 16^\circ$, $Re = 9 \times 10^6$.

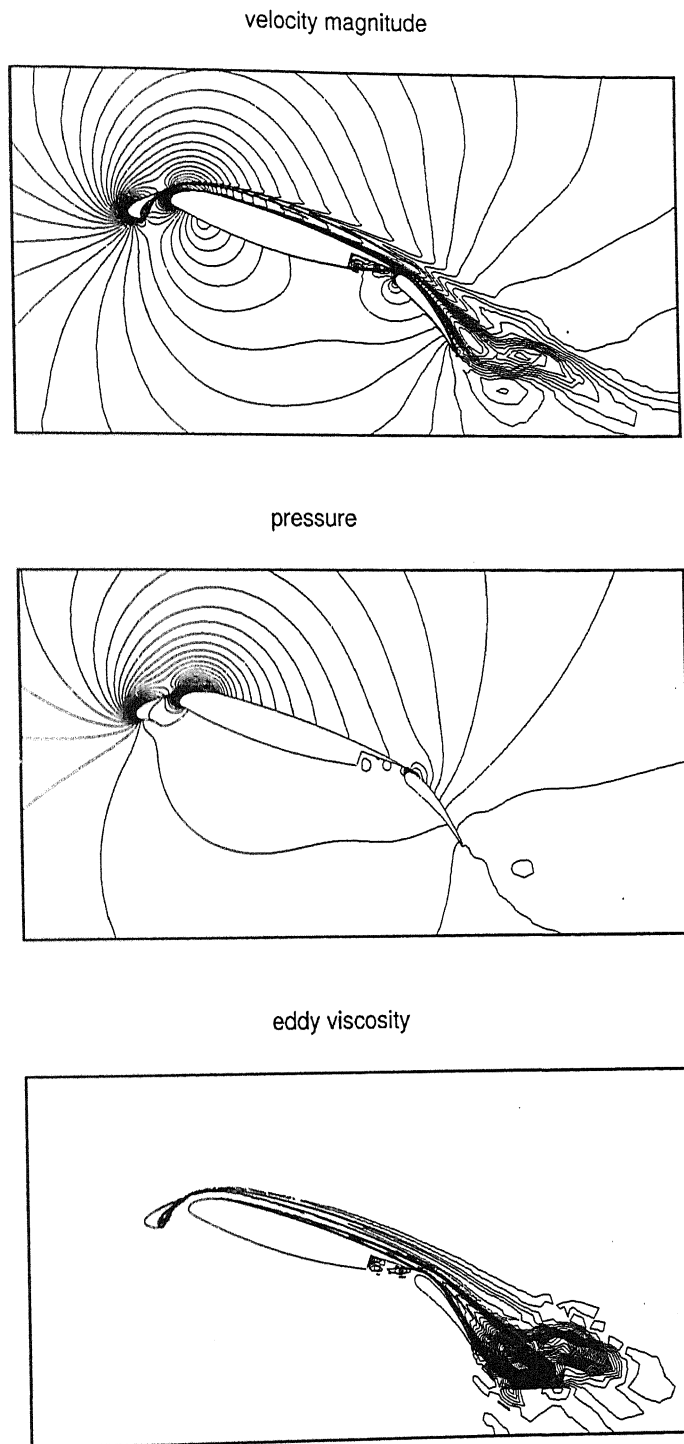


Figure 4.35: Multi-element airfoil: Contours of velocity magnitude, pressure fields, eddy viscosity at $\alpha = 19^\circ$, $Re = 7 \times 10^6$.

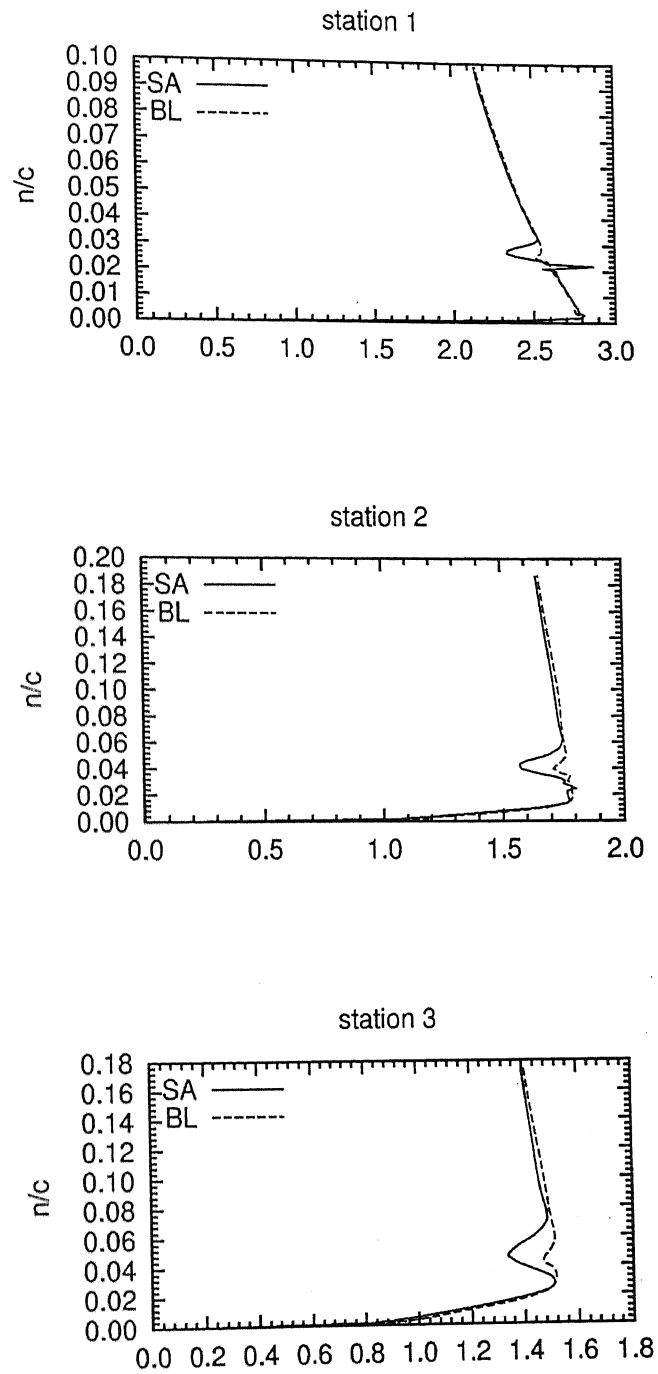


Figure 4.36: Multi-element airfoil: velocity distribution on main element at $\alpha = 19^\circ$, $Re = 7 \times 10^6$.

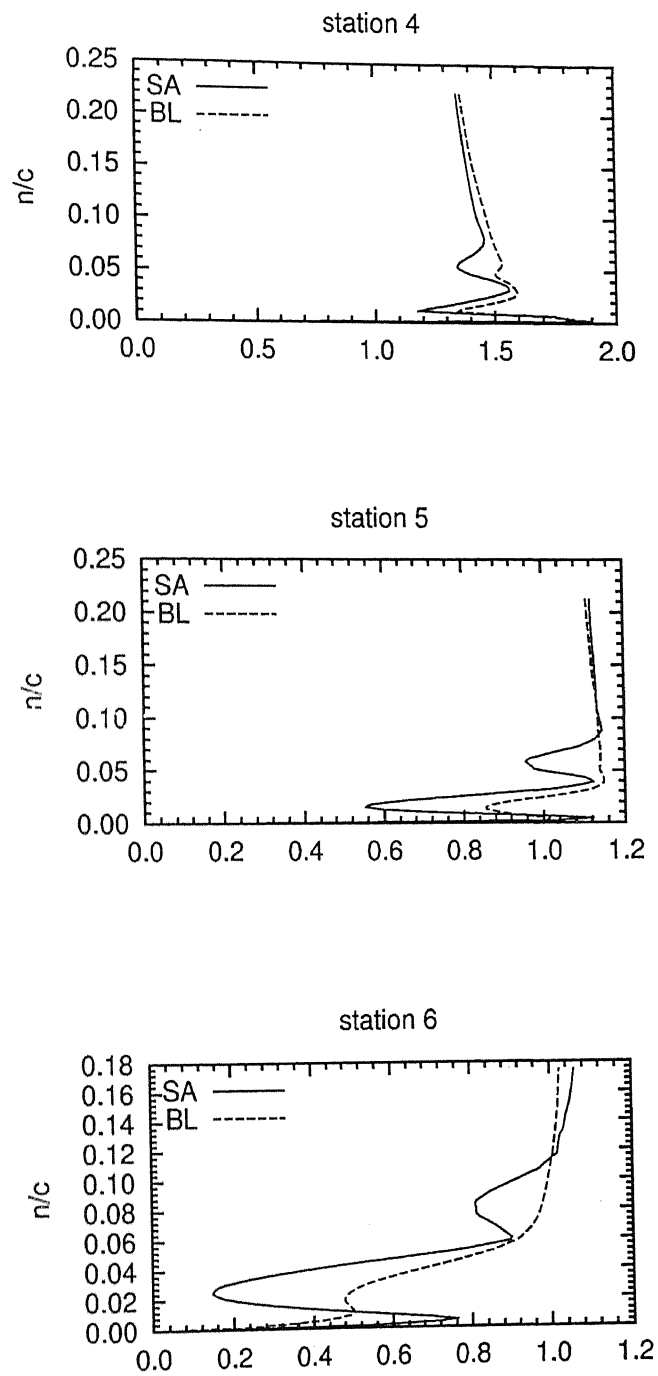


Figure 4.37: Multi-element airfoil: velocity distribution on flap at $\alpha = 19^\circ$, $Re = 7 \times 10^6$.

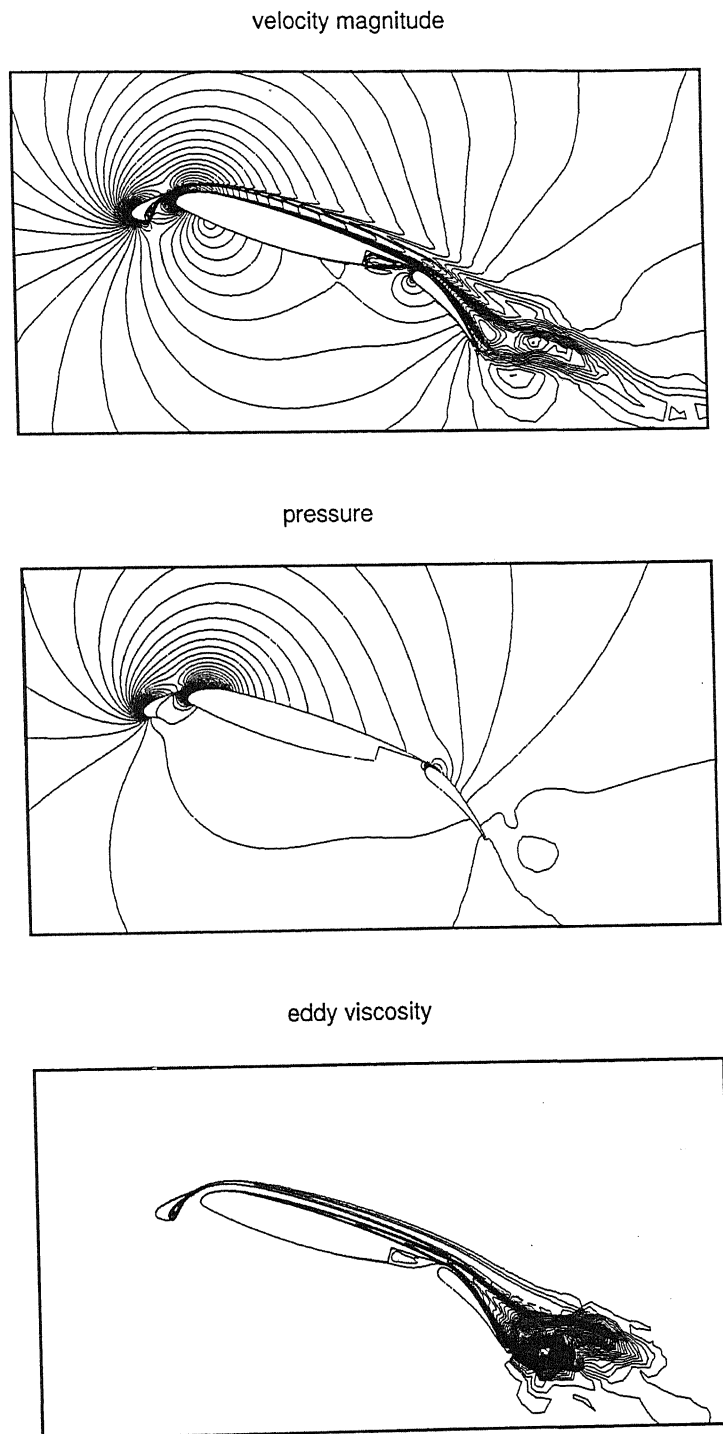


Figure 4.38: Multi-element airfoil: Contours of velocity magnitude, pressure fields, eddy viscosity at $\alpha = 19^\circ$, $Re = 9 \times 10^6$.

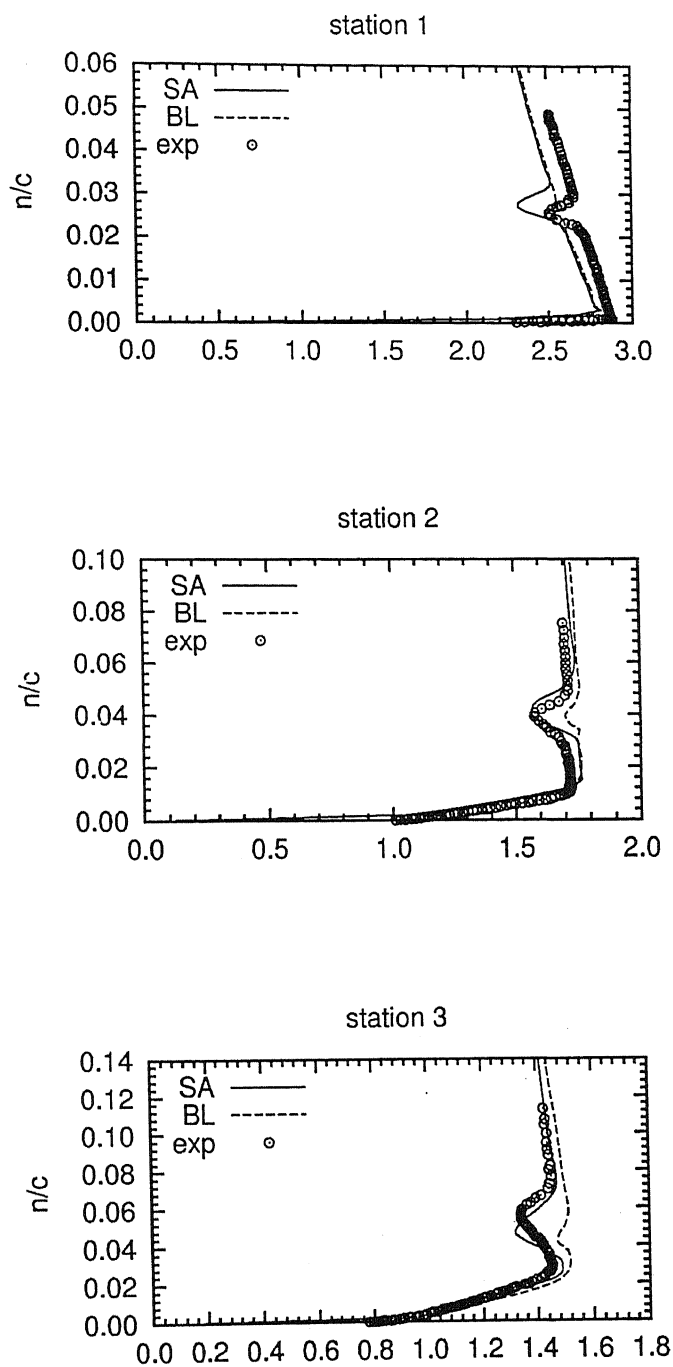


Figure 4.39: Multi-element airfoil: velocity distribution on main element at $\alpha = 19^\circ$, $Re = 9 \times 10^6$.

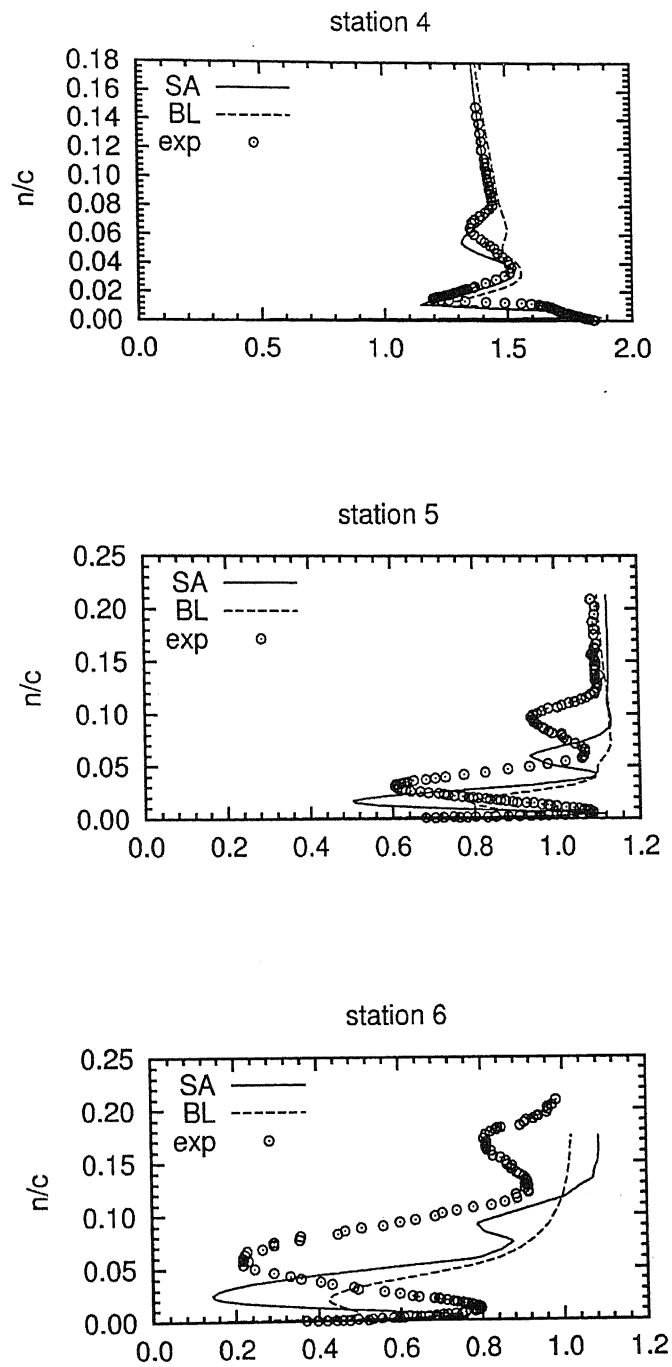


Figure 4.40: Multi-element airfoil: velocity distribution on flap at $\alpha = 19^\circ$, $Re = 9 \times 10^6$.

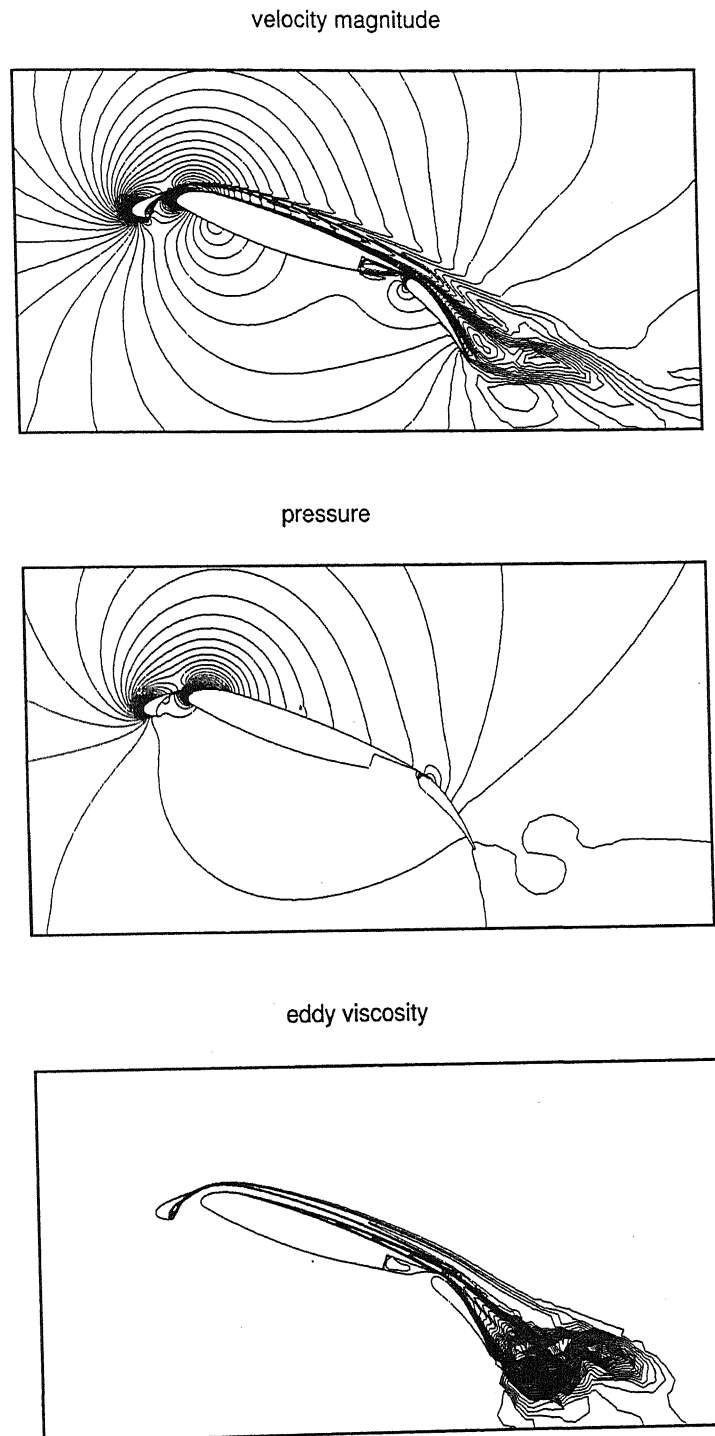


Figure 4.41: Multi-element airfoil: Contours of velocity magnitude, pressure fields, eddy viscosity for mesh1 at $\alpha = 21^\circ$, $Re = 9 \times 10^6$.

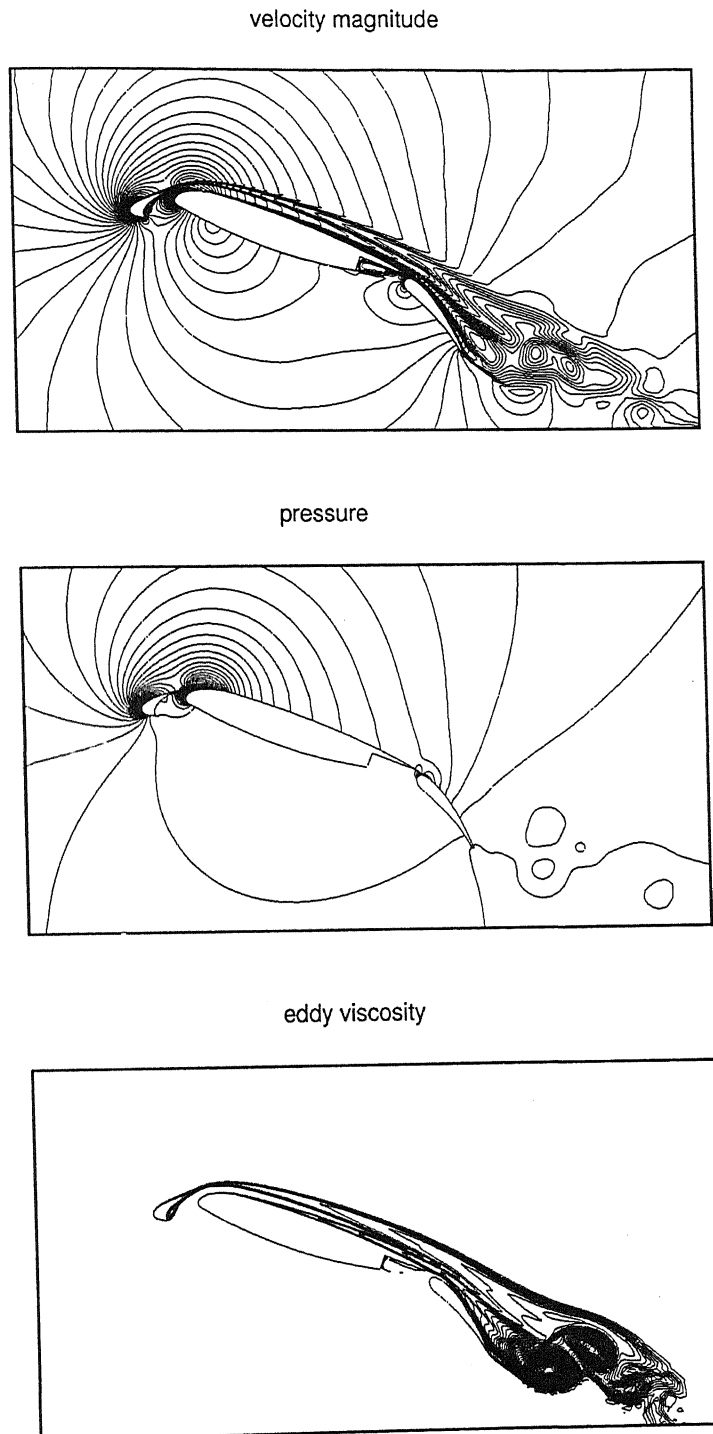


Figure 4.42: Multi-element airfoil: Contours of velocity magnitude, pressure fields, eddy viscosity for mesh2 at $\alpha = 21^\circ$, $Re = 9 \times 10^6$.

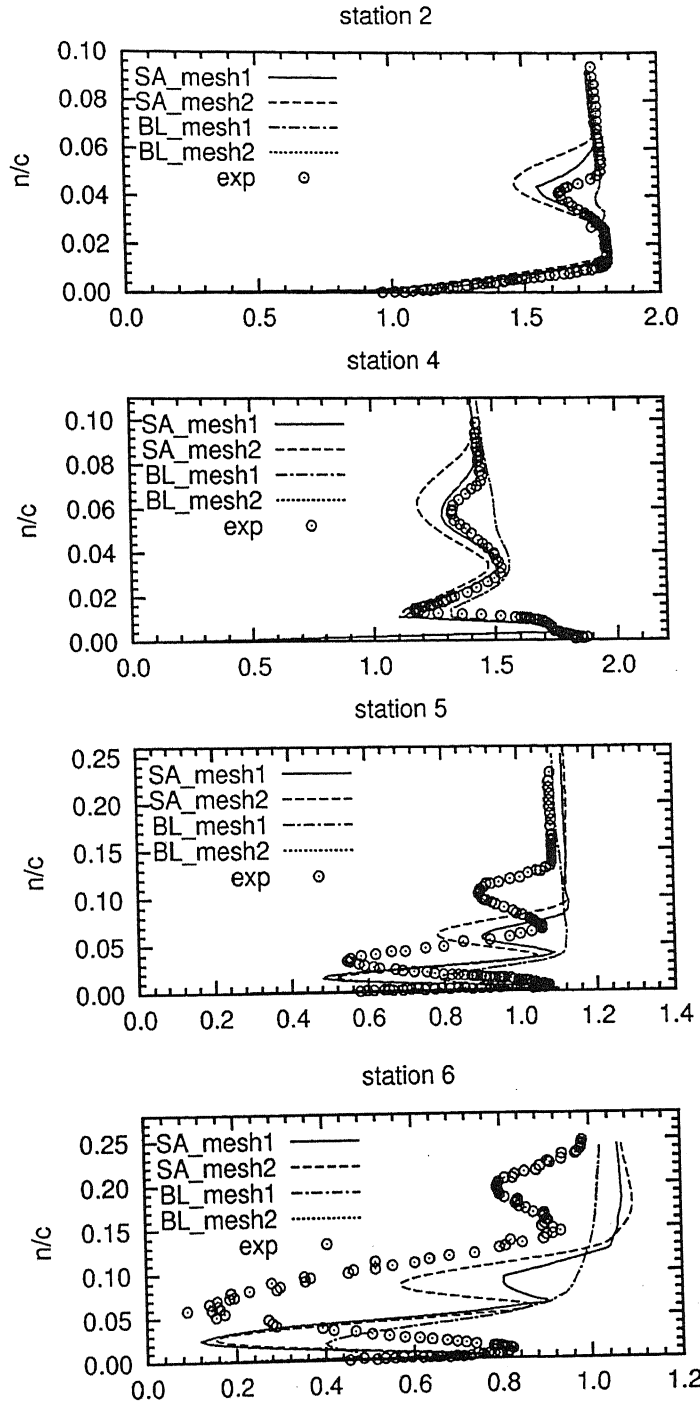


Figure 4.43: Multi-element airfoil: velocity distribution at $\alpha = 21^\circ$, $Re = 9 \times 10^6$.

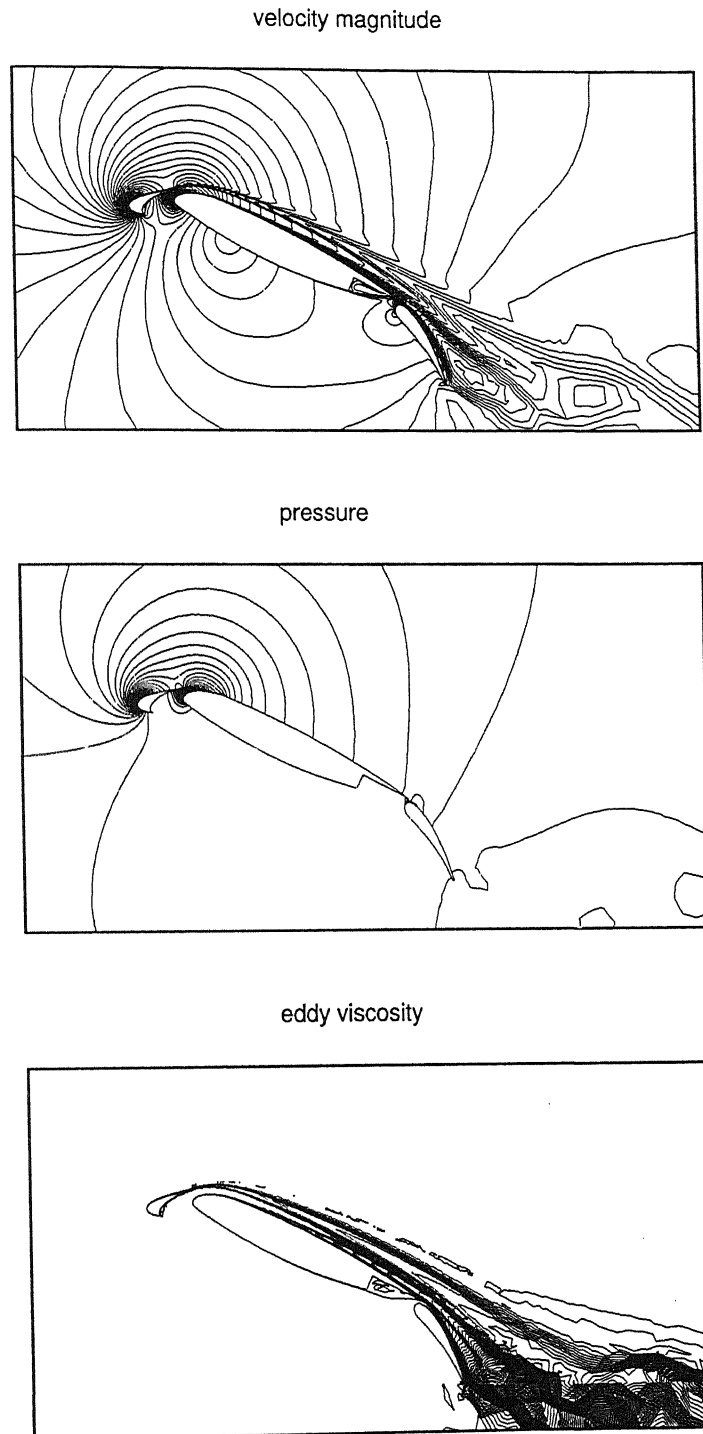


Figure 4.44: Multi-element airfoil: Contours of velocity magnitude, pressure fields, eddy viscosity at $\alpha = 27^\circ$, $Re = 9 \times 10^6$.

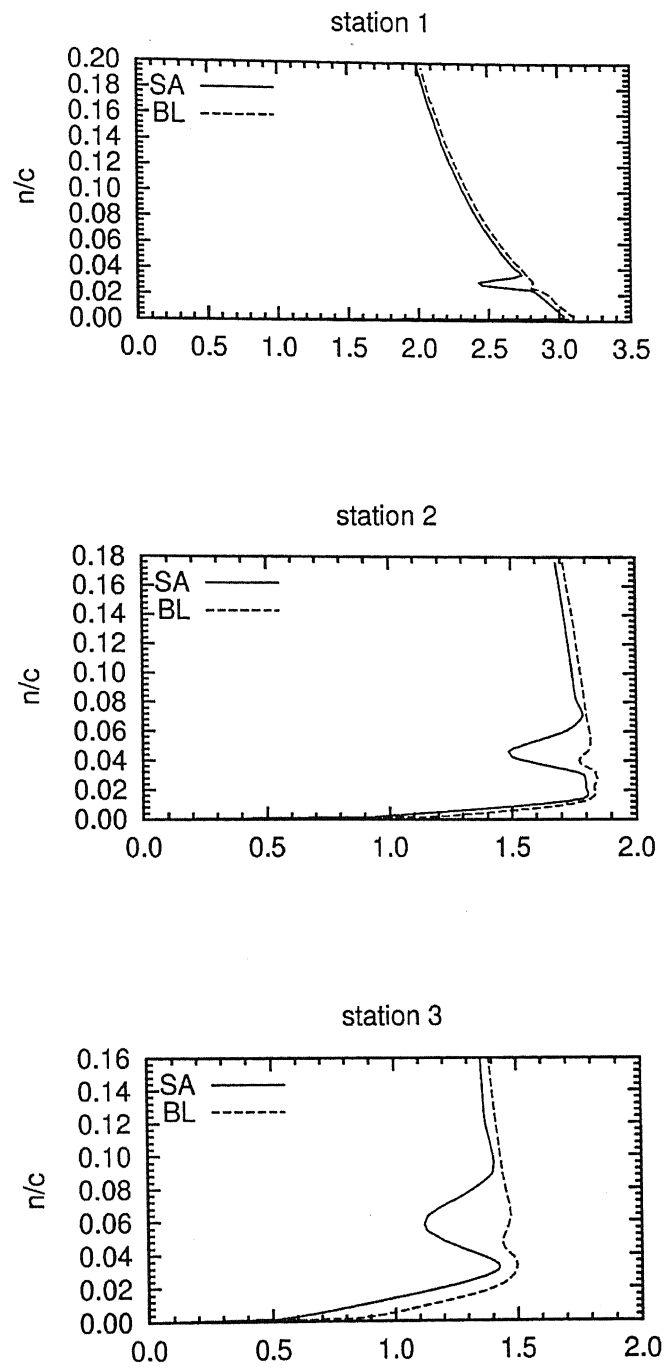


Figure 4.45: Multi-element airfoil: velocity distribution on main element at $\alpha = 27^\circ$.

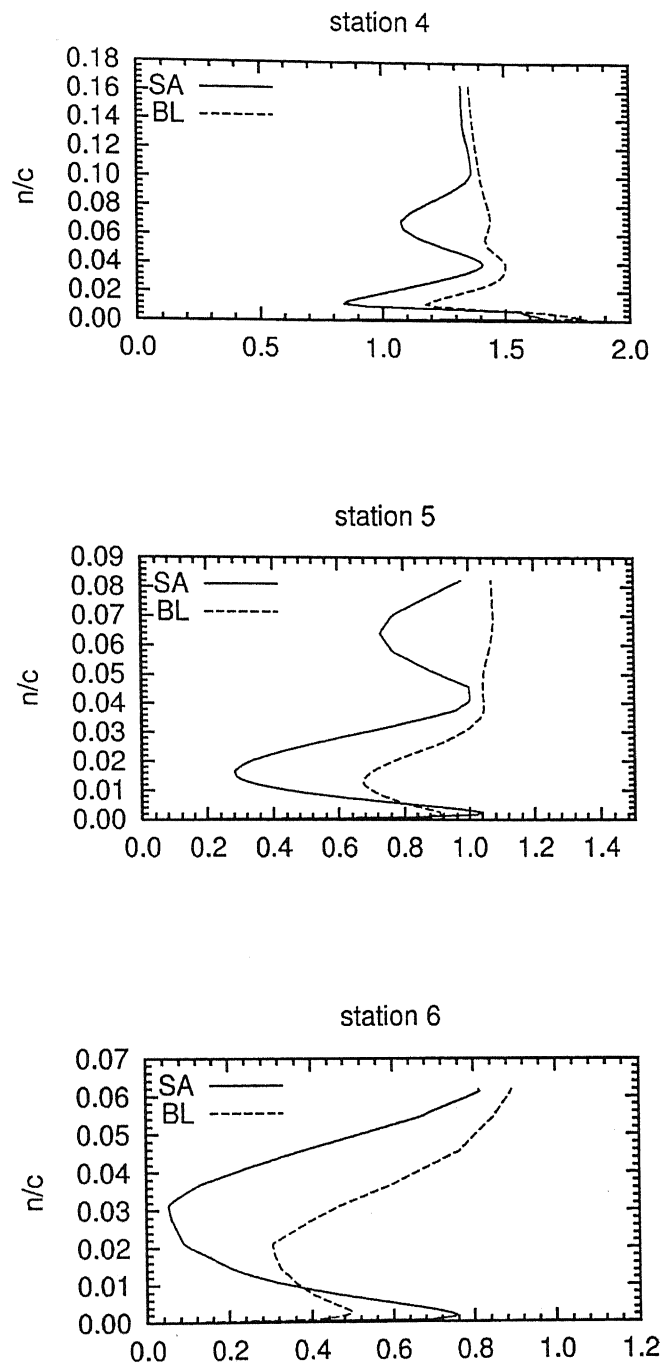


Figure 4.46: Multi-element airfoil: velocity distribution on flap at $\alpha = 27^\circ$.

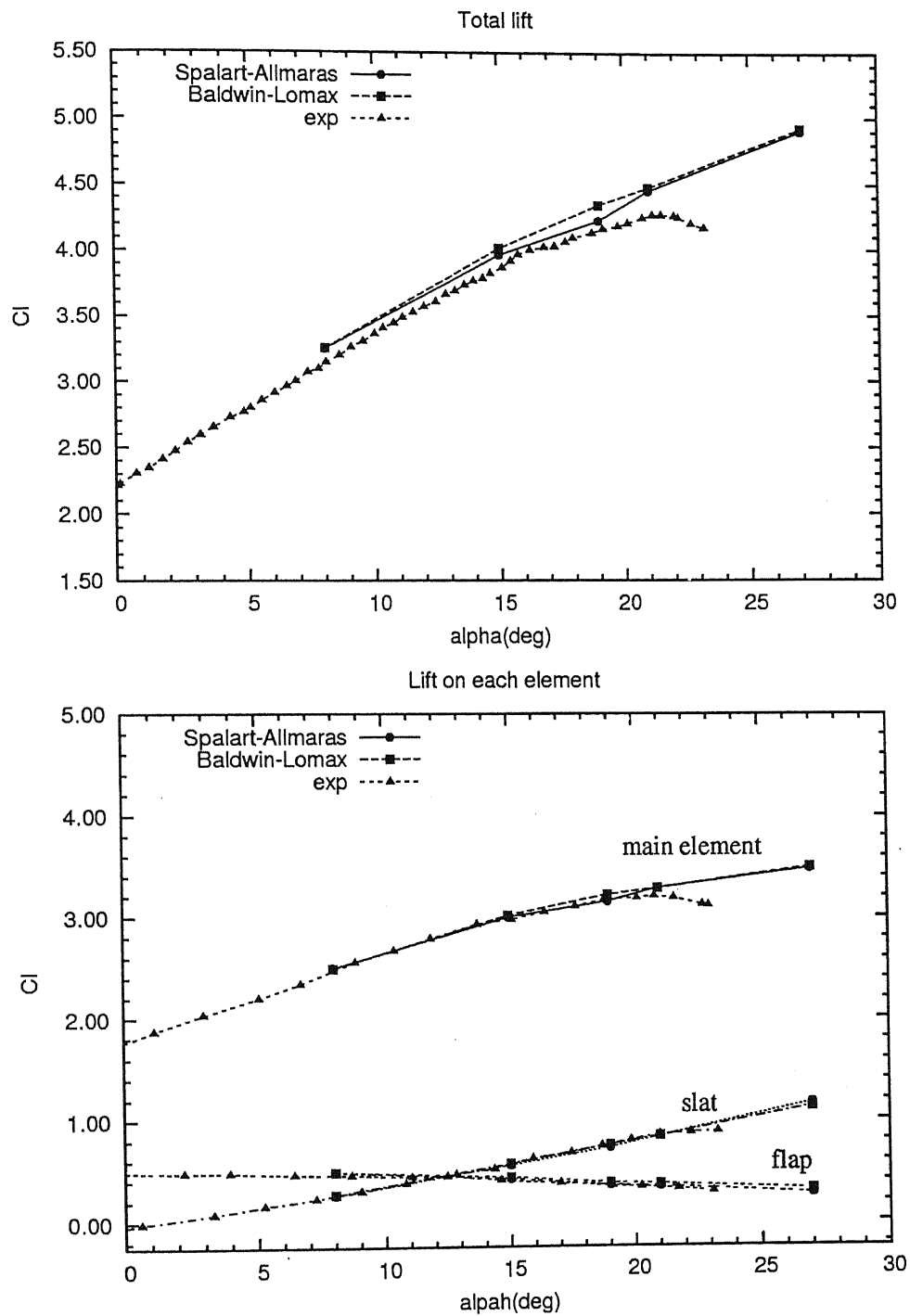


Figure 4.47: Multi-element airfoil: C_l Vs angle of attack at $Re = 9 \times 10^6$.

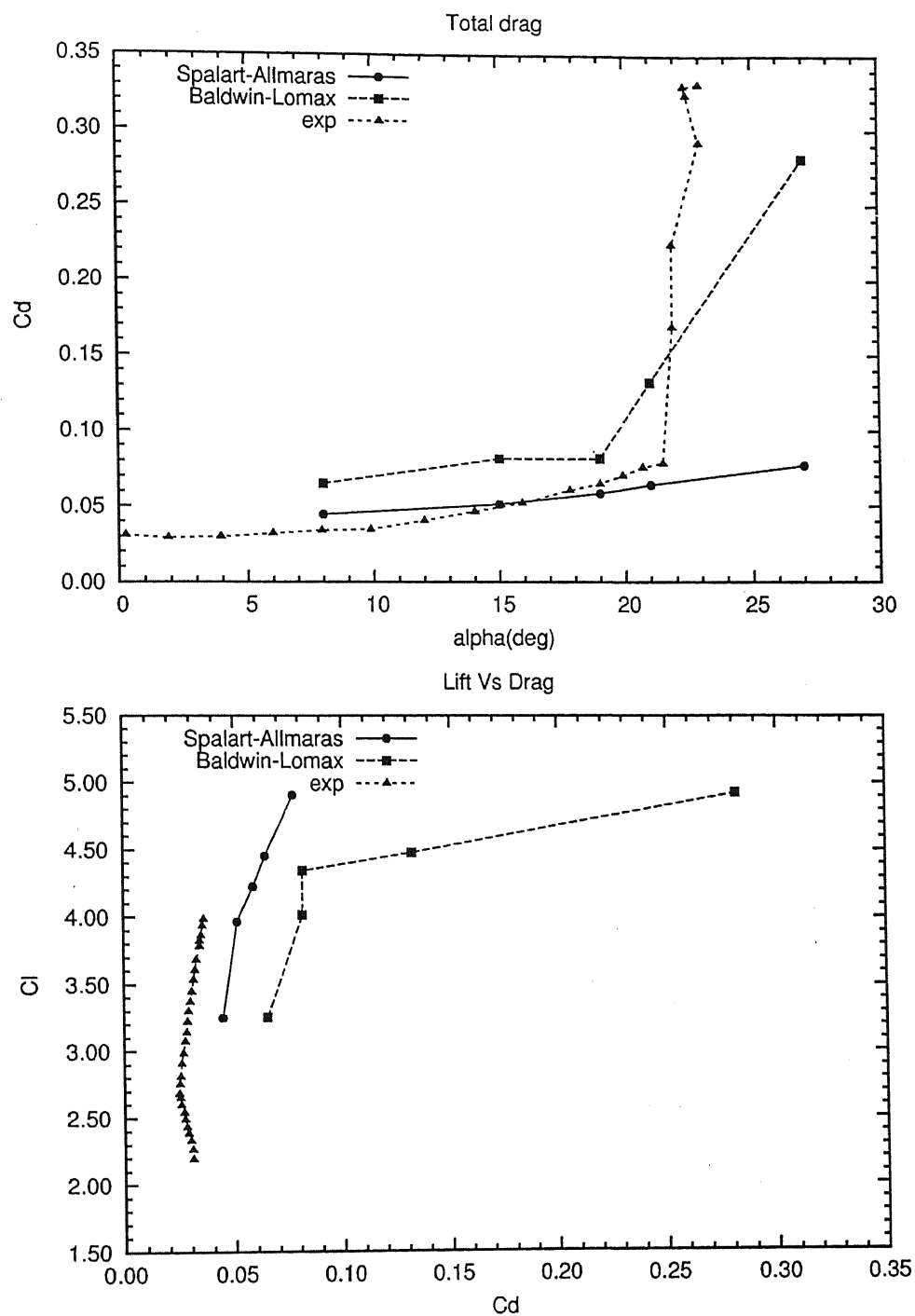


Figure 4.48: Multi-element airfoil: C_d Vs angle of attack at $Re = 9 \times 10^6$.

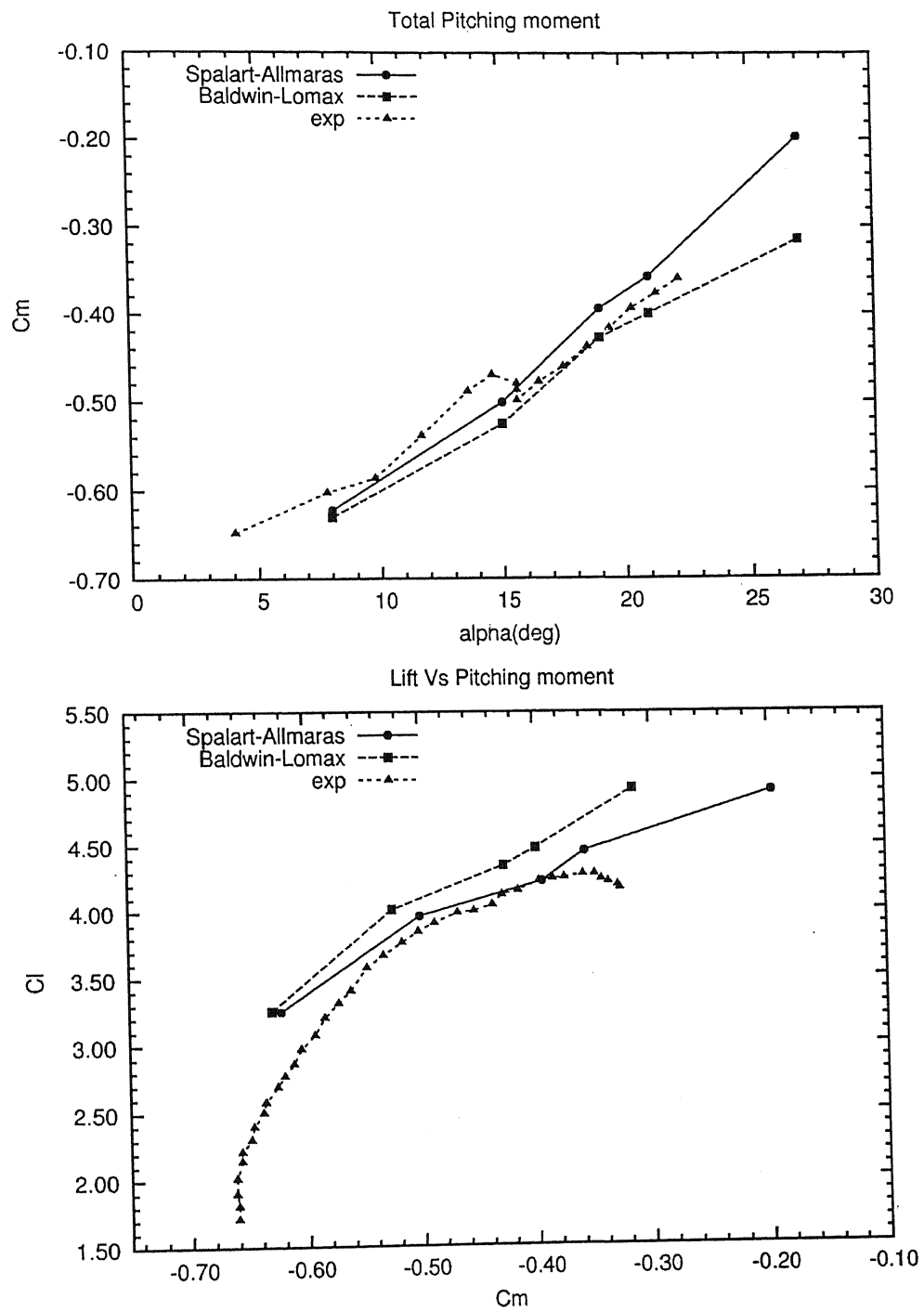


Figure 4.49: Multi-element airfoil: C_m Vs angle of attack at $Re = 9 \times 10^6$.

4.4 Convergence of GMRES solver

In the present study, GMRES technique in conjunction with diagonal preconditioners has been used to solve the equation system resulting from finite element formulations. It was observed that for high aspect ratio elements, even with a fully implicit method, the program has a problem in convergence with larger time steps. This was also investigated.

Laminar Flow

The solver was working properly in the context of laminar flow. The convergence rate was also found impressive.

Turbulent Flow

In case of turbulent flow, problem arose in the solver with poor convergence rate. So, it is evident that the problem was caused due to the turbulence model. Therefore, the term wise investigation was carried out to improve the convergence rate. Equation 2.6.19 refers the differential equation for full turbulence model. As, the whole computation has been done for fully turbulent cases, the trip terms(f_{t1} & f_{t2}) in equation 2.6.19 were assigned to 0. So, the resultant equation which was effectively solved, is equation 2.6.17. The following terminologies were used during convergence study.

$\frac{D\bar{v}}{Dt}$	Term1
$c_{b1}\bar{S}\bar{v}$	Term2
$\frac{1}{\sigma^*} \left[\nabla \cdot ((\nu + \bar{\nu}) \nabla \bar{v}) + c_{b2} (\nabla \bar{v})^2 \right]$	Term3
$c_{w1} f_w \left[\frac{\bar{v}}{d} \right]^2$	Term4
Change of f_w w.r.t. \bar{v}	Term5

Combinations of these terms were included/excluded to form the LHS of the matrix resulting from the finite element discretization. During convergence study, always changes were made in both preconditioner and the iterative subroutine. The results have been tabulated below:

Term1	Term2	term3	Term4	Term5	Remarks
On	Off	Off	Off	Off	Good convergence
On	On	Off	Off	Off	Good convergence
On	On	On	Off	Off	Poor convergence
On	On	Off	On	Off	Good convergence
On	On	Off	On	On	Poor convergence

After the above said investigation was carried out, it was found that Term3 & Term5 were causing problem. Further analysis led to the approximation of the parameter $(\nu + \bar{\nu}) \nabla \bar{\nu}$ in the preconditioner and finally this parameter was approximated to $(\nu) \nabla \bar{\nu}$ to improve the convergence rate, whereas Term5 still remained as a problematic term. As a result of that Term5 was totally turned off from both preconditioner & the iterative subroutine in the rest of the computations for getting improved convergence rate.

In addition to these changes, several more things like different values for element length(h) & stabilization term(τ), addition of least square terms, larger Krylov spaces, were incorporated to improve the convergence rate. But the implementation of all these changes had a very little effect in convergence rate, so, these changes were no more used in the computations.

After stabilization, the modified solver was working fine for NACA 0012 airfoil but once again started causing problem while implementing for multi-element airfoil with larger time steps. To address this problem, computations for the multi-element airfoil were carried out in block-iteration manner. First the eddy viscosity equation is solved and then velocity & pressure equations. The process is repeated for various iteration within a time step.

Chapter 5

Conclusions

2-D simulations of turbulent flows using Spalart-Allmaras turbulence model on three geometries of increasing complexity, have been carried out by solving incompressible Navier-Stokes equation, in the context of finite element formulation, to understand the flow physics as well as the numerical aspects. Initially the computations were done on flat plate, then NACA 0012 airfoil and finally for McDonnell Douglas 30P-30N multi-element airfoil. Flat plate results showed very good agreement with the theoretical results with successful control over the trip locations. The computed results showed consistency in the context of increased spatial resolution also. In case of NACA 0012 airfoil, the obtained results have also been found quite impressive. With the discussed results, it can be concluded that this turbulence model is able to capture the flat plate flow phenomenon and flow over NACA 0012 airfoil successfully.

The flow around multi-element airfoil is quite complex involving confluent shear layers. The flow on each element should be resolved properly since the shear layer of an element affects the flow on subsequent elements. The results have been compared between two different turbulence models and experiments. The surface C_p distribution shows very little difference in the flow solutions of each of the models. The velocity profiles exhibit some differences in the computations, particularly in the spreading rates of wake regions of the flow. The SA model showed almost close match with the experiment in the wakes, while the BL model consistently showed the least amount of velocity defect in wakes. The most significant difference observed between the computational results and the experimental data, is in the slat wake at the lower angle of attack. The

grid resolution study showed that this difference did not decrease with increased grid resolution. From the presented results it is not well understood that the discrepancy in the slat wake is a problem with the turbulence models, or with the grid resolution, or due to some other factor. The lift coefficient has been over predicted in computations. The computed drag is not also very much close to the experimental values. Similarly the pitching moment has also been over predicted. Both the models are unable to predict stall behaviour even at higher angle of attack, whereas experimental results show stall near $\alpha = 21^\circ$. Given the complexity of the multi-element airfoil geometry and the surrounding flow field, it would be wisest to proceed with additional treatment of transition terms in the SA model which may be helpful in predicting the stall properly.

Chapter 6

Scope for Future Work

- The effect of transition location is explored in Spalart-Allmaras model. But in the present study, the code does not employ transition modeling. As a result of that the fully turbulent solutions have been accomplished. So, the transition modeling can be explored.
- Hysteresis effects can be studied over multi-element airfoil.
- The dynamics of deployment of slat and flap can be explored.
- The fully implicit program has a problem while computing on multi-element geometry. So, the GMRES solver can be further analyzed for calculating suitable preconditioner.

References

- [1] A. M. O. Smith. High-lift Aerodynamics. *Journal of Aircraft*, Vol. 12, No. 6:501–530, June, 1975.
- [2] E. G. Tulapurkara. Turbulence Models for the Computation of Flow Past Air-palnes. *Progress in Aerospace Science*, Vol. 33:71–165, 1997.
- [3] P. R. Spalart & S. R. Allmaras. A One-Equation Turbulence Model for Aerodynamic Flows. *30th Aerospace Sciences Meeting & Exhibit, AIAA-92-0439*, January 6-9, 1992.
- [4] P. R. Spalart & M. L. Shur. On the Sensitization of Turbulence Models to Rotation and Curvature. *Aerospace Science and Technology*, Vol. 1, No. 5:297–302, 1997.
- [5] M. L. Shur, M. K. Strelets, A. K. Travin, and P. R. Spalart. Turbulence Modeling in Rotating and Curved Channels: assessing the Spalart-Shur Correction. *AIAA Journal*, Vol. 38, No. 5:784–792, May, 2000.
- [6] W. K. Anderson, D. L. Bonhaus, R. J. McGhee, and B. S. Walker. Navier-Stokes Computations and Experimental Comparisons for Multielement Airfoil Configurations. *Journal of Aircraft*, Vol. 32, No. 6:1246–1253, Nov.-Dec., 1995.
- [7] P. Godin & D. W. Zingg. High-Lift Aerodynamics Computations with One and Two Equation Turbulence Models. *AIAA Journal*, Vol. 35, No. 2:237–243, February, 1997.
- [8] S. De Rango & D. W. Zingg. Higher-Order Aerodynamics Computations On Multi-Block Grids. *15th AIAA Computational Fluid Dynamics Conference, AIAA 2001-2631*, June 11-14, 2001.
- [9] C. L. Rumsey & T. B. Gatski. Recent Turbulence Model Advances Applied to Multielement Airfoil Configuratins. *Journal of Aircraft*, Vol. 38, No. 5:904–910, Sep.-Oct, 2001.
- [10] C. L. Rumsey, T. B. Gatski, S. X. Ying, and A. Bertelrud. Prediction of High-Lift Flows Using Turbulent Closure Models. *AIAA Journal*, Vol. 36, No. 5:765–774, May, 1998.

- [11] L. Kim & K. Nakahashi. Navier-Stokes Computations of Multi-Element Airfoils. *Tohoku University, Aoba 01, Sendai 980-8579, Japan*.
- [12] W. O. Valarezo & D. J. Mavriplis. Navier-Stokes Applications to High-Lift Airfoil Analysis. *Journal of Aircraft*, Vol. 32, No. 3:618–624, May-June, 1995.
- [13] J. H. Morrison. Numerical Study of Turbulence Model Predictions for the MD 30P/30N and NHLP-2D Three-Element Highlift Configurations. *NASA/CR-1998-208967*, Dec., 1998.
- [14] K. M. Jones, R. T. Biedrom, and M. Whitlock. Application of a Navier-Stokes Solver to the Analysis of Multielement Airfoils and Wings using Multizonal Grid Techniques. *AIAA Paper 95-1855*, 1995.
- [15] S. E. Rogers, F. Menter, P. A. Durbin, and N. N. Mansour. A Comparison of Turbulence Models In Computing Multi-Element Airfoil Flows. *AIAA Paper 94-0291*, 1994.
- [16] A. Nakayama, H. P. Kreplin, and H. L. Morgan. Experimental Investigation of Flow-field About a Multielement Airfoil. *AIAA Journal*, Vol. 28, No. 1:14–21, January, 1990.
- [17] S. M. Klausmeyer & J. C. Lin. Comparative Results From a CFD Challenge Over a 2D Three-Element High-Lift Airfoil. *NASA Technical Memorandum-122858*, May, 1997.
- [18] T. B. Gatski. Prediction of Airfoil Characteristics With Higher Order Turbulence Models. *NASA Technical Memorandum-110246*, 1996.
- [19] C. L. Rumsey, M. D. Sanetrik, R. T. Biedrom, N. D. Melson, and E. B. Parlette. Efficiency and Accuracy of Time-Accurate Turbulent Navier-Stokes Computations. *13th AIAA Applied Aerodynamics Conference, AIAA 95-1835*, June 19-22, 1995.
- [20] W. K. Anderson, R. D. Rausch, and D. L. Bonhaus. Implicit/Multigrid Algorithm for Incompressible Turbulent Flows on Unstructured Grids. *AIAA 95-1740*, 1995.
- [21] B. A. Singer. Modeling the Transition Region. *NASA/CR-4492*.
- [22] D. L. Bonhaus, W. K. Anderson, and D. J. Mavriplis. Numerical Study To Assess Sulfur Hexafluoride as a Medium for Testing Multielement Airfoils. *NASA Technical Paper 3496*, June, 1995.
- [23] K. Paschal, L. Jenkins, and C. Yao. Unsteady Slat-Wake Characteristics of a High-Lift Configuration. *30th Aerospace Sciences Meeting & Exhibit, AIAA-2000-0139*, January 10-13, 2000.

- [24] O. Reynolds. On the dynamical theory of incompressible viscous and the determination of the criterion. *Philos. Trans. of Roy. Soc. London, Ser A-186*, pages 123–164, 1895.
- [25] S. J. Kline, D. J. Cockrell, M. V. Morkovin, G. Sovram, and editors. Proceedings Computation of Turbulent Boundary Layers. *Stanford University Mechanical Engineering Dept.*, Vol. 1, 1968.
- [26] D. E. Coles, E. A. Hirst, and editors. Proceedings Computation of Turbulent Boundary Layers. *Stanford University Mechanical Engineering Dept.*, Vol. 2, 1968.
- [27] B. S. Baldwin & T. J. Barth. A One-equation turbulence transport model for high Reynolds number wall-bounded flows. *AIAA-91-0610*, 1991.
- [28] Vinod Kumar. Computation of Flows Past Multi-Element Airfoil. *M.Tech Thesis*, February, 2001.
- [29] S. Mittal. On the performance of high aspect ratio elements for incompressible flows. *Computer Methods in Applied Mechanics and Engineering*, Vol. 188:269–287, 2000.
- [30] M. Sosonkina, L. T. Watson, and R. K. Kapania. A New Adaptive GMRES Algorithm For Achieving High Accuracy. *SIAM Journal On Sci. Computing*.
- [31] Y. Saad. A flexible inner-outer preconditioned gmres algorithm. *SIAM Journal On Sci. Computing*, Vol. 14:461–469, 1993.
- [32] H. A. Vander Vorst. Krylov Subspace Iteration. *Computing in Science & Engineering*, pages 32–37, January/February, 2000.
- [33] J. Baglama, D. Calvetti, G. H. Golub, and L. Reichel. Adaptively Preconditioned GMRES Algorithms. *SIAM Journal On Sci. Computing*, Vol. 20, No. 1:243–269, 1998.
- [34] Youssry Y. Botros and John L. Volakis. Preconditioned Generalized Minimal Residual Iterative Scheme for Perfectly Matched Layer Terminated Applications. *IEEE Microwave and Guided wave letters*, Vol. 9, No. 2:45–47, February, 1999.
- [35] T. E. Tezduyar, M. Behr, S. K. Aliabadi, S. Mittal, and S. E. Ray. A new mixed preconditioning method for finite element computations. *Computer Methods in Applied Mechanics and Engineering*, Vol. 99:27–42, 1992.
- [36] C. P. van Dam and K. Nikeforat. Accurate Prediction of Drag Using Euler Methods. *Journal of Aircraft*, Vol. 29, No. 3:516–519, May-June, 1992.
- [37] Y. Saad and M. H. Schultz. GMRES: a generalized minimal residual method for solving nonsymmetric linear systems. *SIAM Journal on Sci. Stat. Computing*, Vol. 7:856–869, 1986.

-
- [38] F. M. White. *Viscous Fluid Flow*. McGraw-Hill, Inc., 2nd Edition, 1991.
 - [39] H. Schlichting. *Boundary Layer Theory*. McGraw-Hill Book Company, 7th Edition.
 - [40] H. Tennekes & J. L. Lumley. *A First Course in Turbulence*. The MIT Press.
 - [41] S. B. Pope. *Turbulent Flows*. Cambridge University Press.
 - [42] T. J. R. Hughes. *The Finite Element Methods, Linear Static & Dynamics Finite element Analysis*. Prentice-Hall, Inc.
 - [43] T. J. Chung. *Finite Element Analysis in Fluid Dynamics*. McGraw-Hill International book Company.
 - [44] E. Kreyszig. *Advanced Engineering Mathematics*. John Willey & Sons, Inc., 8th Edition.